NUMERICAL ANALYSIS AND EXPERIMENTAL STUDY OF FIBER BUNDLES AND MULTI-CORE PHOTONIC CRYSTAL FIBERS FOR USE IN ENDOSCOPES

A Dissertation
Presented to the Faculty of the Graduate School
of Cornell Univeristy
In Partial Fulfillment of the Requirements for the Degree of
Doctor of Philosophy

by
Kristen Paulene Lantz Reichenbach
January 2007

NUMERICAL ANALYSIS AND EXPERIMENTAL STUDY OF FIBER BUNDLES AND MULTI-CORE PHOTONIC CRYSTAL FIBERS FOR USE IN ENDOSCOPES

Kristen Paulene Lantz Reichenbach, Ph. D.
Cornell University 2007

Flexible endoscopes for confocal and multiphoton imaging have the potential to revolutionize the medical field by obviating the need for invasive biopsies; however, these high expectations can be achieved only by reducing endoscope size and by improving image resolution. In this dissertation, methods for enhancing the performance of current endoscopes are explored by studying the properties of multi-core fibers using numerical modeling and experimental analysis. Numerical simulation tools are based on the normal mode expansion of the fields, coupled mode theory, and the multipole method.

Image fibers (multi-core step-index fibers commonly used in fiber endoscopes) have small, closely spaced cores that are predicted through basic theoretical analysis to be strongly coupled. These image fibers are explained to successfully transmit images because of nonuniformities in their cross-section that reduce inter-core coupling. The wavelength, average core size, and degree of variation in core size determine the strength of coupling between adjacent cores, such that fibers with smaller cores at longer wavelengths require more nonuniformity in order for reliable image transmission. Guidelines are given for assessing the performance of image fibers in a particular system. In addition, due to the random nature of this effect, strong core

coupling can be observed experimentally, demonstrating that the quality of images from current endoscopes is still compromised by crosstalk.

Multi-core photonic crystal fibers (PCFs) are a potential alternative for use in flexible endoscopes. PCFs achieve tighter mode confinement than image fibers and are therefore predicted to allow higher core densities with less crosstalk and, ultimately, improved image contrast and resolution. The fabrication of these fibers, however, typically introduces nonuniformities into the photonic crystal cladding. Random nonuniformities in the air hole size and location are shown to reduce the coupling length and the coupling efficiency. When the air holes are large, variations in the lattice of less than 1% are sufficient to cause essentially independent core propagation. Nonuniformities are also shown to increase the core birefringence although the dispersion and loss of PCFs are rather robust to variations.

Understanding the characteristics of core coupling is a first step towards improving the design of current endoscopes.

BIOGRAPHICAL SKETCH

Kristen Paulene Lantz Reichenbach was born Kristen Paulene Lantz in rural Wisconsin on July 29th in 1979 to parents Paul and Alene Lantz. She has one older sibling, Karen. Her home town of Baraboo is most well-known for the circus that locates itself there and for its quaint downtown. Kristen's most fond memories growing-up are long summer camping trips with her family and running around bare-foot with the neighborhood kids. Kristen was a member of the school marching band, the city 4-H club, the math club, and various sports teams. In May of 1997, Kristen graduated high school as the valedictorian of her class. The following fall, she left home to explore life at a small liberal arts college in rural Iowa. Grinnell College turned out to be a wonderful melting pot of culturally diverse, intelligent, and uniquely motivated individuals, and also, quite a good time. During her freshman year, she changed her major from psychology to physics thanks to the gentle persuasions of her college advisor, Mark Schneider. She also majored in French, spending a semester abroad in the town of Rouen, France, expanding her horizons and traveling around Europe. The summer between her sophomore and junior year, she met Rob Reichenbach while studying with an NSF sponsored REU program at Hope College in Michigan—thank you NSF for bringing these two together. When they both graduated from college in May of 2001, they set off together to Ithaca, New York to study for Ph.D. degrees at Cornell University. The couple was wed in June of 2004. In August of 2006, Rob obtained his Ph.D. in Electrical Engineering and moved to Portland, Oregon to work for Intel Corporation. Kristen will begin work at the patent boutique firm, Klarquist Sparkman, LLP, in Portland in the beginning of January, 2007.

This dissertation is dedicated to my parents,
who gave me the confidence and freedom to pursue any goal,
and to my husband Rob,
my best friend through everything

ACKNOWLEDGEMENTS

I would like to take this opportunity to acknowledge those colleagues who have helped me to complete the research necessary for obtaining my Ph.D. First of all, I would like to thank my advisor, Chris Xu, for allowing me to be the first student that he graduates at Cornell University and for being a great source for ideas and motivation.

I owe my present sanity, and also a bit of thanks for enduring the not so sane moments, to my fellow graduate students in the Xu group. Thanks to Jim van Howe for letting me follow him around Cornell—from our office together in Rockefeller Hall to becoming the first students of Chris Xu—and for his self-effacing humor and non-judgmental attitude that always made me feel at home. Thanks to Mike Durst for being eternally willing to help me out—whether I needed a beam-splitter ordered, a Labview program to collect data, or a kitchen to cook brownies in—for his warm welcomes to the lab, and for always asking how my weekend went. Thanks to Jen Lee, for putting up with my GWP adventure and for listening to my Matlab problems even when she didn't have the answer. Thanks also to Demirhan Kobat for lively discussions about research and philosophy. I can't imagine how grueling my graduate career would have been without a group of people surrounding me who were always willing to listen to my questions, give me advice, laugh at my jokes, and help me to feel among friends.

I am grateful for our collaborations with OFS Optics, and specifically to John Fini for insightful discussions about the multipole method and programs based on this method. I would also like to acknowledge the Cornell Nanofabrication Facility staff (and my husband) for assisting with SEM images, and Jim McDonald at Myriad Fiber

Imaging Tech., Inc., for the Fujikura fiber bundle samples and information about the fibers. I must also acknowledge the University of Sydney through its ARC Centre of Excellence - Ultrahigh-bandwidth Devices for Optical Systems, School of Physics as the exclusive Licensor of the CUDOS MOF UTILITIES Software and I thank Boris Kuhlmey for answering questions about the program. I would like to acknowledge the financial support of the National Center for Research Resources, National Institutes of Health. I would also like to acknowledge Larry Chen for working with me these last couple months and for continuing some aspects of this research.

Finally, thanks to my husband, Rob. During my graduate career, he has been there to listen to all my practice talks, to voluntarily proof-read my papers, and to support me when nothing seemed like it would work. He has served as a continual source of encouragement; without him, I would not have made it.

TABLE OF CONTENTS

LIST OF FIGURES

LIST OF TABLES

Chapter 1

INTRODUCTION

Two revolutions in optical microscopy have occurred in the last century. The first was the invention of the confocal microscope in 1955, which uses an aperture to block out-of-focus light from hitting the detector [1]. This advance in microscopy was made possible by the advent of laser scanning—a system where the laser focus is scanned over a sample and the image is collected pixel by pixel. The signal to background ratio is drastically improved over standard wide-field imaging, increasing resolution and allowing for optical sectioning—when images are taken at different depths in the sample. Image quality and penetration depth were also improved with the discovery of multiphoton imaging using pulsed lasers in 1990 [2]. Background signal is reduced and excitation is more localized because of the nonlinear nature of this process. Both confocal and multiphoton microscopy have had an enormous impact on the medical research community by making it possible to image living cells and intact tissues.

Flexible endoscopes utilize optical fibers to extend the sample stage of a standard microscope to an alternative location. Confocal and multiphoton imaging through flexible endoscopes has the potential to transform the medical field by obviating the need for invasive biopsies and by assisting in early diagnosis. These types of endoscopes would allow for *in vivo* observation and measurement of internal tissue and organs through relatively noninvasive procedures. Current fiber endoscopes typically contain either coherent fiber bundles or single-core fibers and are used to access areas of the body such as the gastrointestinal tract, the respiratory tract, and the female reproductive system. The improvement of current endoscope systems may some day allow smaller more inaccessible regions such as veins or delicate brain tissue to be probed noninvasively.

In endoscope systems with image fibers or coherent fiber bundles, the laser focus is scanned over the proximal end of the image fiber. The output at the distal end, however, is no longer focused. In order to focus the light to a spot smaller than the individual image fiber core and to control the depth of focus for performing optical sectioning, optics must be fused to the distal end of the fiber. These components typically contain miniaturized lenses and focusing mechanisms that are bulky, rigid, and expensive. In addition, the images taken using fiber bundles have an inherent pixilation due to the individual cores that transmit the information. The resolution of the transmitted image is limited by the size and separation of these cores as well as by the degree of coupling between the cores.

Single-core fiber endoscopes typically utilize a smaller diameter fiber; however, the functionality of the endoscope is still limited by the size of additional optics. In order to perform laser scanning, the distal end of the fiber itself must be physically moved to image over a region of the sample. In addition, distal focusing optics are again necessary for improving resolution and controlling the depth of focus.

While current endoscopes have already lessened the need for certain invasive procedures, reducing the size, improving the image resolution, and increasing the functionality would amplify their impact. The research presented in this dissertation was motivated by these goals. A completely new type of fiber, a multi-core photonic crystal fiber, was investigated for its potential to improve the laser scanning technology necessary for endoscopic confocal or multiphoton imaging. Air-silica PCFs achieve tighter mode confinement than image fibers and are therefore predicted to allow higher core densities with less crosstalk and, as a result, improved image contrast and resolution. The propagation and coupling properties of multi-core PCFs were explored with the intention of designing a high core density fiber with minimal core coupling. A fiber of this type would facilite the removal of all optics from the distal end of the fiber while simultaneously maintaining image quality and laser scanning capabilities. The size of the end probe would be greatly reduced, resulting in endoscopes no larger than the fiber diameter. The fabrication of PCFs, however, typically introduces nonuniformities into the photonic crystal cladding. The viability of endoscope designs utlizing photonic crystal fibers depends on a thorough understanding of these fibers, their unique properties, the factors that control inter-core coupling, and the implication of fabrication induced nonunformities these characteristics.

In addition, the resolution of current fiber endoscopes containing image fibers can be improved through the production of fibers with smaller, closer pixels (ie. high core density). High core density, however, increases crosstalk between pixels, thus resulting in blurred images, decreased contrast, and a lower signal to background ratio. Balancing the need for improved image quality with the degrading effects of crosstalk requires a detailed understanding of how light propagates in these multi-core fibers, how changing the pixel density can alter these properties, and what the impact of the nonuniformity observed in actual image fibers has on the fiber performance.

This dissertation is a study of light propagation in fiber bundles and multi-core PCFs through use of numerical modeling tools and experimental observation. The coupling of light between cores in a multi-core fiber, or crosstalk, can be understood using well-developed models of light propagation in coupled waveguides. Coupled mode theory and normal mode expansion method are used to model light propagation in multi-core fibers. The fiber modes are calculated using the multipole method with both a Matlab program developed by the author in addition to a Fortran program available from the University of Australia at Sydney (www.physics.usyd.edu.au/cudos/software/) [3]. In general, nonuniformities in the cross-section of both fiber bundles and two-core photonic crystal fibers can facilitate the reduced coupling required for applications in endoscopic imaging.

Chapter 2 introduces the reader to the basic concepts of light propagation in cylindrical optical fibers. This chapter reviews total internal reflection and the concept of modes in a standard step-index fiber. An intuitive understanding is given through descriptions based on the ray picture of light and the importance of diffraction is also addressed. Solutions to the scalar wave equation are derived and several important properties of step-index fibers are described.

Chapter 3 covers the concept of coupling between a pair of waveguides. A basic explanation of light coupling between cores in a fiber is presented initially followed by an in depth discussion of two methods for quantifying the coupling behavior in a system of waveguides. First, by expressing the field solution in a waveguide as an expansion of its modes, the power exchange between two cores, and therefore the nature of the coupling, can be determined. In addition, coupled mode theory, an analytical model for predicting coupling, is summarized. The implications of non-identical cores on the coupling properties of a two-core system are discussed briefly.

Chapter 4 provides an introduction to the field of photonic crystal fibers. The different types of photonic crystal fibers are presented and the properties of high-index core fibers are discussed. The effective index model is used to provide insights into the unique characteristics of these fibers.

Chapter 5 explains the multipole method for use as a mode solver for photonic crystal fibers and mulit-core step-index fibers. The implementation of this method using Matlab is also discussed, including insights into the accurate application of this program and method. The use of this Matlab program in conjunction with the CUDOS MOF Utilities software is also addressed.

In Chapter 6, the theories of coupling presented in Chapter 3 are applied to photonic crystal fibers for predicting the coupling length. The scalar effective index model is used for applying coupled mode theory to these fibers and the results are compared to the vector normal mode expansion method. The relationship between photonic crystal fiber dimensions and the coupling lengths of different types of two-core fibers are presented and based on these results a proposal for a multi-core photonic crystal fiber endoscope is presented in Appendix A.

Chapter 7 presents the published work of the author on the impact of random nonuniformities in the photonic crystal cladding on the birefringence, loss, dispersion, and coupling length of a photonic crystal fiber. Fibers with large air holes are shown to exhibit the most sensitivity to variations in the air hole location and size.

Chapter 8 specifically addresses the implications of nonuniformities on coupling in two-core photonic crystal fibers, also published work. The coupling efficiency in large air hole fibers is shown to be greatly reduced when the photonic crystal cladding is nonuniform. Additional information on the effects of nonuniformities on coupling in these types of fibers is given in Appendix B.

Chapter 9 is work that has been submitted for publication concerning the coupling properties and performance of multi-core step-index fibers such as coherent fiber bundles, or image fibers. It is explained that current image fibers used in flexible endoscopes are able to transport images due to nonunformity in the fiber cross-section. Analytical expressions based on coupled mode theory are developed in order to predict the performance of available image fibers.

Chapter 10 presents results from the experimental observation of coupling in image fibers, also submitted for publication. The physical set-up is described and the wavelength and polarization dependence of coupling are experimentally demonstrated for fibers manufactured by Fujikura and Sumitomo. The results are supported by numerical simulations based on the theory presented in Chapter 9.

Finally, Chapter 11 provides a short summary of the research presented. In addition, possible future projects in this area and concepts for continued research are mentioned.

Chapter 2

PROPAGATION OF LIGHT IN FIBERS

Introduction to step-index fibers

Optical fibers are cylindrical waveguides that confine or guide electromagnetic radiation in the optical frequencies. The most basic optical fiber design is the step-index fiber which is illustrated in Figure 2-1. These fibers are referred to as "step-index" because the index distribution of the materials that compose the fiber resembles a step function. While a fiber can have many possible index distributions, this example remains the simplest and most common. The core and the cladding are

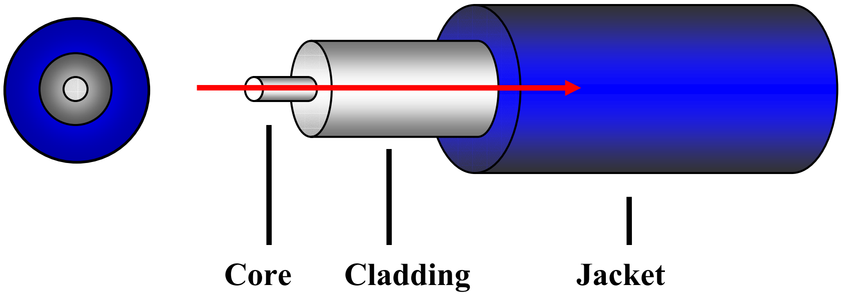

Figure 2-1. A standard step-index fiber; an end profile appears to the left and a side view to the right. Light propagates in the core region.

composed of dielectric or insulating materials such that the core has a higher index of refraction than the cladding. The materials are usually silica (SiO_2), which has an index of about 1.5, or else silica that has been doped to slightly increase or decrease the index. The fiber dimensions remain constant along the length which can be hundreds of kilometers. Depending on the application and the wavelength, the core diameter commonly falls within a range of ~2 μm to ~50 μm and the cladding diameter is on the order of a few hundred microns. The presence of a jacket strengthens the fiber and protects it from breaking.

Optical fibers have several advantages over traditional copper wires because they are lighter and smaller, have increased bandwidth, and eliminate electromagnetic interference. In addition, because of advances in the production of low loss glass, optical fibers are a viable solution for long distance communications. The major application for optical fibers is in telecommunications, though use in local networks and short distance deployments are also common.

Ray-picture for light propagation

When the size of the core is much larger than the wavelength, diffraction effects due to the wave nature of light are negligible and a ray picture can be used to describe how light propagates in a step-index optical fiber. A ray describes light of a well-known spatial direction (k-vector) or momentum and therefore exploits the particle nature of light. In Figure 2-2, a ray of light is shown entering a fiber core at an arbitrary angle θ_i. The law of refraction or Snell's law, derived by matching boundary conditions at a dielectric interface, can be used to describe the path of the

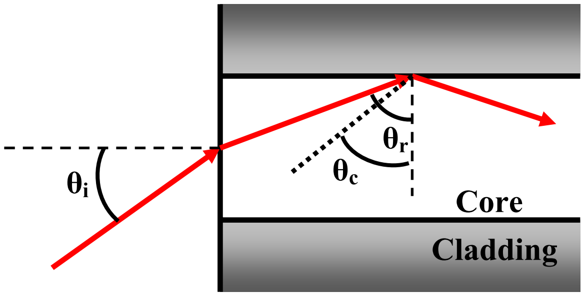

Figure 2-2. Light entering the core at an angle of θ_i is refracted due to the change in refractive index. When incident on the boundary between the core and the cladding, light is completely reflected if $\theta_r > \theta_c$.

ray as it enters the fiber core and encounters the core-cladding boundary. From this relationship, the maximum value for θ_i can be determined such that θ_r will always be greater than the critical angle for total internal reflection, θ_c. At the critical angle of incidence, light is refracted at a boundary with a lower index material such that no light is transmitted and all light remains in the higher index material. These two angles are defined in Eq. (2.1).

$$\sin\theta_c = \frac{n_{cl}}{n_{co}}, \text{ and } \quad \max\theta_i = \sin^{-1}\sqrt{n_{co}^2 - n_{cl}^2} \tag{2.1}$$

where n_{cl} indicates the refractive index of the cladding and n_{co} is that of the core. For angles θ_i less than the max θ_i defined in Eq. (2.1), total internal reflection will occur at the core-cladding boundary. The numerical aperture (NA) of the fiber can then be defined as sin(max θ_i) and the acceptance angle of the fiber is $2\theta_i$. Only rays entering the fiber within the cone of its acceptance angle will experience total internal reflection at the core-cladding interface and be guided.

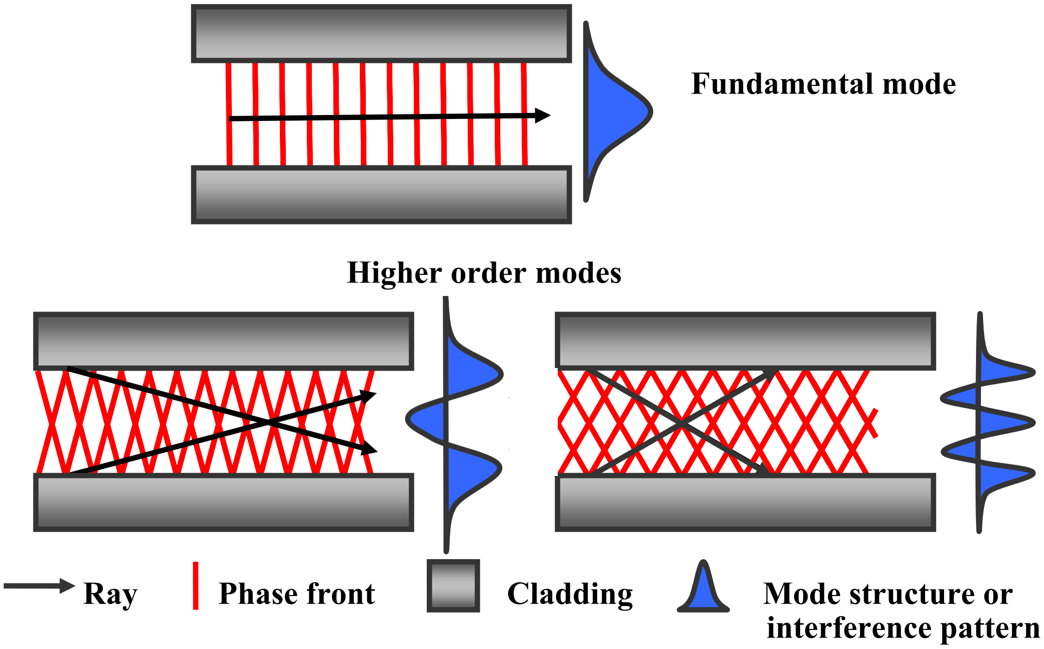

Figure 2-3. Three different modes are illustrated. Two plane waves enter the fiber core at the same angle, within the acceptance angle of the fiber. The direction of propagation is indicated by the ray, and phase fronts from the two rays interfere constructively only because travel from one surface and back again results in a multiple of 2π phase shift, or an integer number of wavelengths. (For simplicity, the diagrams above ignore the Goos-Hänchen shift)

The cone subtended by the acceptance angle contains a continuum of guided or bound rays; however, due to interference, not all of these rays will propagate without loss along the length of the fiber. A resonance condition occurs in the waveguide, limiting propagation to discrete mode solutions. In order to understand how this condition arises, the ray picture must be amended to include the phase of the propagating light wave. A ray describes light with a well-known k-vector; in other words, the ray depicts the direction of propagation of a plane wave of infinite extent. Therefore, lines perpendicular to the path of the ray represent points of constant phase or a wave front as shown in Figure 2-3.

For lines spaced equidistant along the ray, their separation corresponds to the wavelength of the light, which can also be thought of as a change in phase of 2π (see Figure 2-3). Each wave or phase front of a bound ray must accumulate a multiple of 2π total phase shift when propagating from one core-cladding interface and back again in order to constructively interfere with other rays traveling in the fiber at the same angle [4]. Equivalently, the distance the ray travels between reflections must be an integer multiple of the wavelength. This 2π condition selects rays from the incident cone of light with a discrete set of angles that will interfere to produce a stable field distribution called a mode. All rays entering the fiber at the same angle, if they satisfy the mode condition, will avoid energy decay resulting from deconstructive interference and will propagate without loss (assuming no absorption or scattering) along the length of the fiber. See Figure 2-3 for an illustration of the 2π condition satisfied by three different ray angles.

This description is most accurate for multi-moded waveguides, that is, fibers that have more than one mode solution. The fundamental mode exists in all step-index waveguides and the existence of higher order modes depends on the size of the fiber

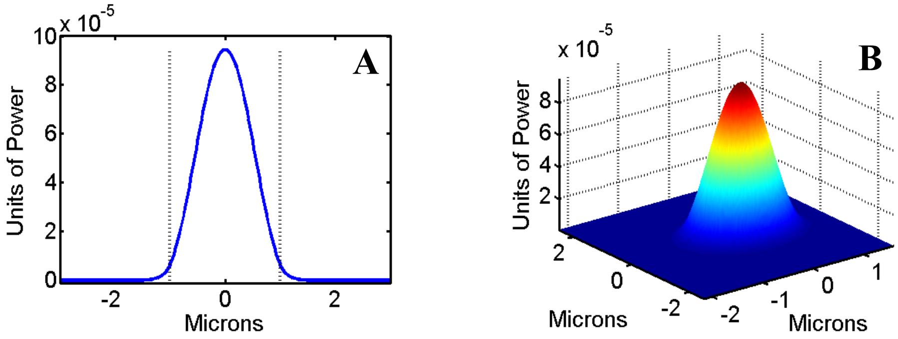

Figure 2-4. The a) transverse profile and b) 3D rendering of the energy distribution of the fundamental mode. The core diameter is indicated by dotted lines in a). The distribution is approximately Gaussian and has azimuthal symmetry.

core relative to the wavelength. The fundamental mode is shown in more detail in Figure 2-4 and is nearly Gaussian with a completely symmetric shape. This mode is typically the most desired for applications of light propagation. The concept of modes and discrete solutions reappears during the rigorous mathematical solution for a cylindrical fiber, and thus is an inherent condition of a steady state solution to a waveguide.

Including diffraction effects

When total internal reflection occurs, the plane wave incident on the core-cladding interface experiences an additional phase shift that can’t be predicted using a ray picture. Because light propagating in the core reflects off of a lower index material (the cladding) a phase shift is experienced at each reflection that is dependent on the wavelength of the light. This phenomenon is due to the effects of diffraction and is most pronounced when the radius of the fiber approaches the wavelength of light. A phase shift is analogous to travel over a distance; thus, in the ray picture, as illustrated in Figure 2-5, this phase shift due to reflection is represented as a lateral shift in distance, z_s (called the Goos-Hänchen shift), caused when the ray travels for a short time in the cladding [4]. This modified description of the ray's path is true to the flow of energy in the fiber. During the short time spent in the cladding, some of the wave's energy is transferred momentarily from the propagating wave to an evanescent or exponentially decaying wave in the cladding before returning completely to the reflected wave in the core. Any perturbation that the evanescent field experiences will result in energy being lost to another structure or coupled out of the core.

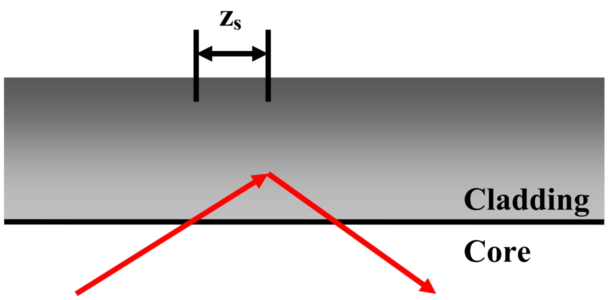

Figure 2-5. A ray picture depiction of the Goos-Hänchen shift, z_s, caused by the reflection of light off of the surface of a material with a lower index of refraction.

The ray picture provides an intuitive explanation for light propagation in fibers; however, the treatment of light as rays is appropriate only in certain regimes and is an approximate portrayal. Light propagation is more accurately described by a beam containing a distribution of plane waves or rays of slightly different propagation directions [5]. The rays used previous actually represent the average location of a beam of light. This description of light is a result of Heisenberg's uncertainty principle which states that the position and the wavelength of light can never be known exactly. In addition, the more precise one of these properties can be determined, the more imprecise the other must be.

Diffraction, or the apparent spreading of light, occurs because each plane wave component in the beam experiences a different phase shift as it propagates over the same distance. When light propagates in air, for example, the plane waves eventually interfere deconstructively and the beam disperses. Uncertainty in the position of the light manifests itself as the finite width of light, previously described as a beam. When the wavelength of light is much smaller than the dimensions of the fiber, the light can be approximated as a ray with an exact position. If the size of the beam is determined more closely—such as through confinement to smaller regions or a smaller core—the distribution of plane waves that compose the beam widens in order to uphold the uncertainty relation, and diffraction effects become stronger. Thus, when the fiber core is small relative to the wavelength, diffraction effects and behavior dependent on the wave-like nature of light instead of the position dominate and the ray picture must be dismissed.

When the dimensions of the fiber core approach the size of the wavelength, fewer modes have lossless propagation down the fiber. For core sizes less than a particular radius, only a single mode solution exists called the fundamental mode. Waveguides that allow only one mode to carry energy/information down the fiber are extremely useful for communications purposes. In order to determine this cutoff radius for a particular fiber, the effects of diffraction must be taken into account. Consider a Gaussian beam of circular cross-section propagating in the high index core of a fiber waveguide. The beam will experience an angular spread from the axis of propagation of $\theta_d \approx \lambda/(n_{co}\pi a)$, where a is the minimum spot size [5]. In order for the maximum amount of light to be guided in the fiber core, θ_d should be equal to or less than the complement of the critical angle, with θ_c as previously defined in Eq. (2.1). Using a trigonometric identity and rearranging this expression, the following relationship is derived [5]:

$$2 = \frac{2\pi}{\lambda} a \sqrt{n_{co}^2 - n_{cl}^2} \tag{2.2}$$

The right side of Eq. (2.2) is called the V-parameter, or the normalized frequency of the waveguide, when a equals the core radius. This simplified argument gives an estimate for the cutoff radius of a fiber for single mode propagation when the wavelength and index values are known. This example also demonstrates how propagation in a waveguide is a balance between spreading due to diffraction and confinement from reflection at the index boundary [5].

Mathematical description of light propagation

Exact expressions for the electric and magnetic field solutions in a fiber can be found using Maxwell's equations. By solving the wave equation in the core region and in the cladding region, and applying the appropriate boundary conditions, expressions for the fiber modes are determined. Because a fiber is a two-dimensional waveguide with an index profile that is a function of only r and ϕ, the z-component of the field will couple only to itself as it propagates along the fiber and is therefore a solution to the scalar wave equation shown in Eq. (2.3).

$$(\nabla^2 + k^2)\left\{\begin{matrix} E_z(r,\phi,z) \\ H_z(r,\phi,z) \end{matrix}\right\} = 0 \tag{2.3}$$

where $k^2 = k_0^2 n^2 = \omega^2 n^2 / c^2$ and ∇^2 is the Laplacian operator in cylindrical coordinates [4, 6]. The remaining components of the field can be derived using Maxwell's equations and the solutions for the z-component. Equation (2.3) can be solved using separation of variables or by assuming a solution of the following form:

$$\begin{aligned} E_z(r,\phi,z) &= E_z(r)\exp(\pm i\nu\phi)\exp(-i\beta z) \\ H_z(r,\phi,z) &= H_z(r)\exp(\pm i\nu\phi)\exp(-i\beta z) \end{aligned} \tag{2.4}$$

where ν is an integer and β is the propagation speed of the field solution. Substituting Eq. (2.4) into Eq. (2.3) results in Bessel's equation, which has well-known solutions. The z-component of the fields can then be written as:

$$\begin{aligned} \text{in core: } E_z(r,\varphi,z) &= AJ_\nu(\kappa r)\exp(i\nu\varphi)\exp(-i\beta z) \\ \text{in cladding: } E_z(r,\varphi,z) &= CK_\nu(\gamma r)\exp(i\nu\varphi)\exp(-i\beta z) \end{aligned} \tag{2.5}$$

where κ^2 is the square of the transverse wavevector $k_0^2 n_{co}^2 - \beta^2$, γ^2 is the square of the attenuation coefficient $\beta^2 - k_0^2 n_{cl}^2$. The z-component of the magnetic field can be written in a similar manner. β can also be understood as the longitudinal wavevector and Figure 2-6 shows the relationship between these wavevectors. Notice that the direction of k can be compared to a bound mode in the ray picture. There exists a

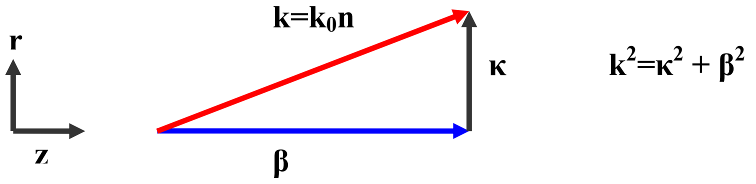

Figure 2-6. The geometric relationship between the different components of the wavevector.

discrete set of values for β in each waveguide and the length of β uniquely determines the mode and indicates the speed of propagation of each mode along the fiber axis. From this diagram, it is obvious that $\beta \leq k_o n$ [4]; therefore, when the magnitude of the longitudinal wavevector is larger than the wavevector in the cladding, but less than that of the core, it will be bound to the core, or $k_o n_{cl} < \beta < k_o n_{co}$, for bound solutions. When the magnitude of the longitudinal wavevector falls outside of these limits, the light will not be bound.

By applying the boundary conditions that the tangential components be continuous at the core-cladding interface, a system of four equations is generated. These equations can be solved simultaneously by first writing the equations in matrix form and then setting the determinant equal to zero. The result is a transcendental equation with solutions only for certain values of the propagation constants, β, which represent the set of mode solutions of the waveguide. The relationship between A and C in Eq. (2.5) can be calculated from the system of boundary condition equations for a particular β. A complete derivation is not presented here but can be found in one of the following sources [4-6].

Cylindrical fibers always guide a fundamental mode because there will be at least one solution to the transcendental equation. The appearance of a second mode can be predicted from the V-parameter, previously defined in Eq. (2.2). The V-parameter can also be understood as the maximum magnitude for the normalized transverse wavevector, or $\kappa_{\max} a$, and the exact expression for this parameter is given in Eq. (2.6)

$$V = \kappa_{\max} a = a k_0 \sqrt{n_{core}^2 - n_{clad}^2} = \frac{2\pi a}{\lambda} \sqrt{n_{core}^2 - n_{clad}^2} \tag{2.6}$$

where *a* is the core radius. The fundamental mode cutoff occurs when the value for V is greater than the 1st root of the zeroth order Bessel function, 2.405, approximately the value estimated in Eq. (2.2). This is referred to as the cutoff for single-mode operation and the value for V can be used to estimate the number of bound modes that a particular waveguide will support. As the size of the wavelength decreases relative to the core radius, V will increase and a fiber will become more multi-moded.

The shape of the modes solutions can be predicted from fields in Eq. (2.5). For each value of v, a different set of m modes exist such that each mode is labeled by two indices. The value for v indicates the number of angular nodes in the mode distribution and m dictates the number of radial nodes. The modes illustrated in Figure 2-3 demonstrate how the number of nodes increases for higher order modes; however, this depiction is only in two dimensions so that these modes would be sufficiently described by only one mode index, m. Note that the fundamental mode is characterized by no nodes and therefore has azimuthal symmetry. This mode will therefore have the highest concentration of power in the fiber core and its approximately Gaussian shape facilitates additional calculations making it the preferred mode for propagation in fibers.

Applications for optical fibers require certain knowledge about the fiber properties. In addition to the number of modes a fiber will support, the dispersion of a waveguide is also an important parameter. Dispersion occurs because different wavelength of light travel at different speeds in the fiber. There are three types of dispersion: material, modal, and waveguide [4]. Material dispersion is a result of the frequency dependence of the permittivity of any material. Rewritten as the wavelength dependence of the index of refraction of a material, this effect is described by the Sellmeier equation [4, 7] and the second derivative is proportional to the group velocity dispersion, or GVD.

$$GVD = -\frac{\lambda}{c}\frac{\partial^2 n}{\partial \lambda^2} \tag{2.7}$$

Modal dispersion can be ignored in single-mode fibers and is caused by the different propagation speeds of the mode solutions. Waveguide dispersion is a result of the structure of the fiber and the fact that changing the wavelength will change the mode solution β. The simultaneous effect of waveguide and material dispersion is often referred to as chromatic dispersion. Dispersion is extremely important for telecom applications and other applications where pulses of light are used to transmit information. Because a pulse is composed of several frequencies, dispersion will cause pulse spreading and signal distortion.

Chapter 3

CORE COUPLING

Introduction to two-core coupling

As alluded to in Chapter 2, energy can be lost from a fiber core when the evanescent part of the mode that is traveling in the cladding experiences a perturbation. For example, a perturbation could be a mechanical bending of the fiber, a notch in the cladding-core interface, or another region of high index material. This last case is a situation where multiple cores exist in a single cladding. Due to the coupling of energy between the cores, light initially incident on only one core will eventually propagate in the other cores. This behavior is essential for the development of devices such as splitters and couplers.

Consider a simplified situation with just two high index cores, C_L and C_R, in a background of a slightly lower index cladding material with a core separation of 3.2 μm and core diameter of 2 μm, as shown in Figure 3-1(a). These cores are equivalent to two adjacent step index fibers as described in Chapter 2. Figure 3-1(b) shows the energy distribution for the fundamental mode of the two-core fiber. Note that the majority of the energy is contained within the core, demarcated by the dotted lines, but a small portion exists in the cladding. In addition, because the light is well confined to

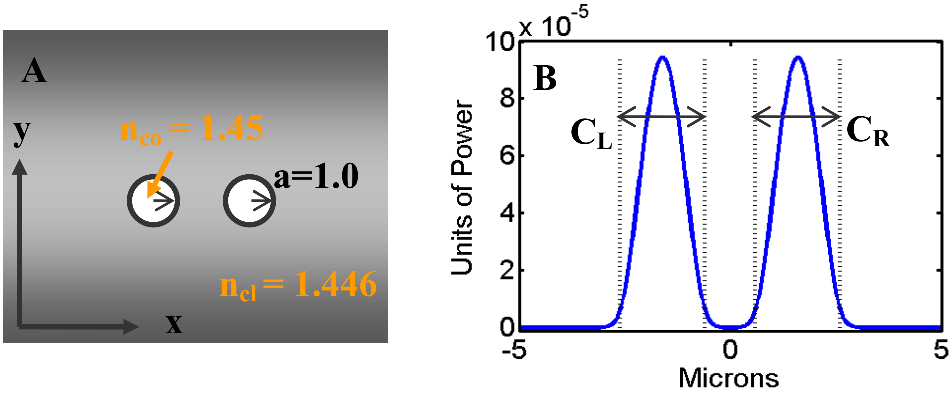

Figure 3-1. Image A is of a two-core step index fiber with core radii of a=1.0µm. Plot B shows the energy distribution for the fundamental mode of the two-core fiber. The core separation is 3.2µm.

the cores, the mode shown in Figure 3-1(b) looks very similar to the sum of the mode of the left core and the mode of the right core.

When light is incident on C_L, the fundamental mode of that core is excited; however, an evanescent or exponentially decaying portion of that field will be present in the cladding and inevitably enter into the high index region of C_R. This energy is trapped in C_R because of its waveguiding properties and becomes a source for a propagating mode in C_R. If the two cores are identical, all the energy from C_L will transfer into C_R. Then the reverse process will occur with energy passing back and forth between the cores along the length of the fiber. The oscillation of power between the cores as a function of the propagation distance, z, is illustrated in Figure 3-2. The percentage of power transferred between cores is referred to as the coupling efficiency, also referred to as crosstalk, and the rate of power transfer is described by the coupling length or beat length defined in Figure 3-2. The coupling length and the

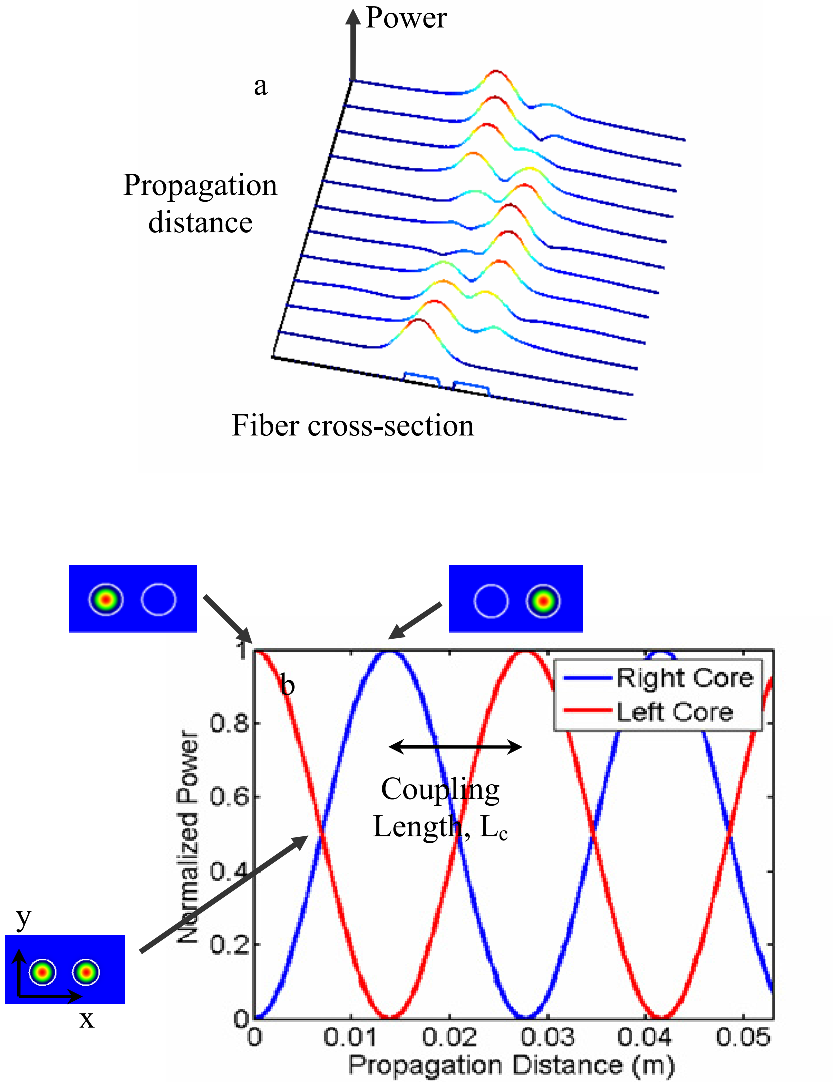

Figure 3-2. Light incident initially on the left core will couple into the right core and back again as it propagates along the fiber. In b), the power in each core is plotted versus the propagation distance and the energy distribution is shown at different points along the fiber length.

coupling efficiency are used to quantify the strength of coupling and represent the beating of the modes of the fiber.

The strength of coupling depends on the separation between the two cores and the size of the core diameters relative to the wavelength. For example, if the separation between two cores is increased, the exponential tail of the excited C_L mode will be weaker when it experiences the high index region of the second core. This will slow down the power transfer or, in other words, increase the coupling length. Figure 3-3 demonstrates for two different two-core fibers how the coupling length increases with core separation. This trend is consistent across changes in the wavelength and for fibers with different core sizes. In addition, if the core size is increased relative to the wavelength—equivalent to reducing the wavelength for a particular fiber—the mode becomes more tightly confined, which also decreases the value of the exponentially decaying field that enters C_R. This relationship is shown in Figure 3-4, where, for a constant core size and separation, the coupling length is shown to decrease with the wavelength for two types of fibers. Thus, to ensure weak coupling at a particular wavelength, two cores should be large and far apart in order to have a long coupling length.

The coupling behavior between two cores in a fiber, as observed in Figure 3-3 and Figure 3-4, can also be predicted through an analogy with a particle in a pair of quantum wells. Increasing the core separation has a similar effect to increasing the well separation which makes it more difficult for a particle to tunnel from one well into the other. Also, decreasing the core size has a comparable outcome to deepening each well, which effectively increases the height of the barrier making tunneling, again, more difficult. In order to increase the probability that a particle will be found

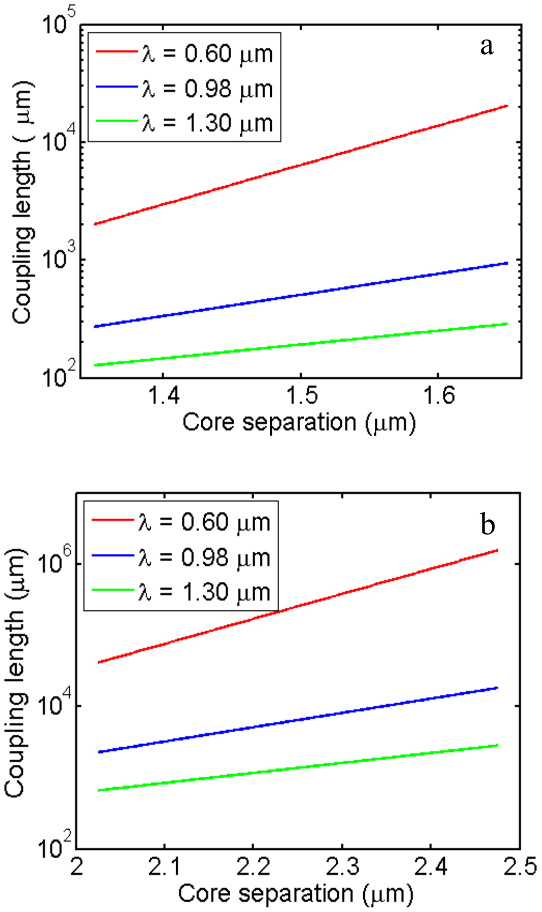

Figure 3-3. The coupling length is plotted versus the core separation for two different two-core fibers with different core diameters and for three wavelengths. In plot a), the diameter of the two cores is 2 μm, while in b) the diameters are 2.9 μm.

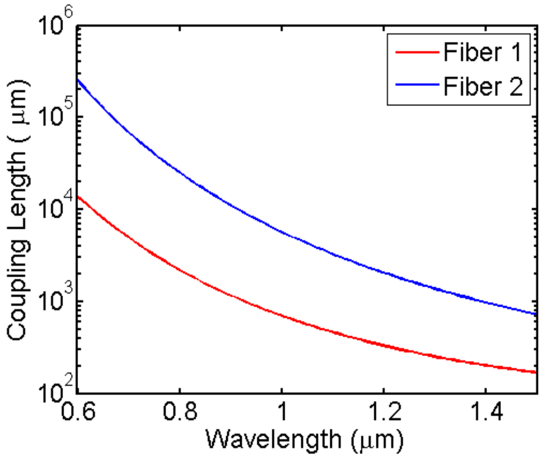

Figure 3-4. The coupling length is plotted over wavelength for two fibers. Fiber 1 has a core separation of 3.2 μm and core diameters of 2 μm while fiber 2 has a core separation of 4.5 μm and core diameters of 2.9 μm.

in its initial state in a single well, the well separation and the barrier height are increased.

Theories of coupling

The ability to calculate the power in each core at different points along the fiber length reveals the nature of the coupling in the fiber. There are two common approaches for determining this coupling behavior. The first method, using normal mode expansion, requires the mode solutions for the complete multi-core system. Because the mode solutions for systems involving multiple waveguides are sometimes difficult or time-consuming to obtain, a second method, called couple mode theory (CMT), is based on the solutions for the individual waveguides and provides an analytical approximation for the complete system. Additional methods exist for calculating the coupling behavior, such as beam propagation method [8], which is a split-step method where the field is expanded in a superposition of plane waves [4], although they will not be discussed in detail here.

Normal mode expansion

A field solution in a waveguide can always be written as an expansion of the set of normal modes of the waveguide [5, 9]. The field is written as:

$$\begin{aligned}\vec{E}(x,y,z) &= \sum_j a_j \vec{e}_j(x,y) e^{in_j kz} \\ \vec{H}(x,y,z) &= \sum_j a_j \vec{h}_j(x,y) e^{in_j kz}\end{aligned} \tag{3.1}$$

where $\vec{e}_j(x,y)$ and $\vec{h}_j(x,y)$ are the modal fields of the fiber (the radiation modes have been ignored for the sake of simplicity), n_j is the corresponding effective index for the j^{th} mode, and the z-direction is parallel to the axis of the fiber. The modal amplitudes, a_j, represent the amount of overlap between the input field and the j^{th} mode and are determined from Eq. (3.2) [5, 9].

$$a_j = \frac{1}{2N_j} \iint_{A\infty} \vec{E}(x,y,0) \times \vec{h}_j^*(x,y) \cdot \hat{z}\, dxdy \tag{3.2}$$

where $\vec{E}(x,y,0)$ is the input field, a Gaussian x-polarized field incident on a single core. N_j determines the normalization of the j^{th} mode as defined in Eq. (3.3):

$$\tfrac{1}{2}\iint_{\infty} \vec{e}_j(x,y)\times\vec{h}_j^*(x,y)\cdot\hat{z}dxdy = \tfrac{1}{2}\iint_{\infty} \vec{e}_j^*(x,y)\times\vec{h}_j(x,y)\cdot\hat{z}dxdy = N_j \tag{3.3}$$

The power in each core as a function of z is calculated from the z-component of the Poynting vector according to Eq. (3.4).

$$P_{core}(z) = \tfrac{1}{2}\mathrm{Re}\iint_{\substack{core\\area}} \vec{E}(x,y,z)\times\vec{H}^*(x,y,z)\cdot\hat{z}dxdy \tag{3.4}$$

where the fields are defined by the expansion in Eq. (3.1). The power in each core as a function of the propagation distance is plotted in Figure 3-2(b).

When solving for the modes of multi-core fibers, the mode group with the largest propagation constants contains 2N modes, where N is the number of cores in the system and the factor of two is consistent with two polarization states. The modes in this group will be referred to as the fundamental modes because the distribution of energy within the individual cores for each of the modes is approximately Gaussian with azimuthal symmetry, as characteristic of a fundamental mode. The normal mode expansion is typically truncated after these 2N lowest order modes since they represent the most significant contribution to the sum due to their large overlap with the Gaussian input field. Our modeling showed that ignoring the higher order modes results in negligible error because the modal amplitudes, a_j, become extremely small.

A two-core fiber has nondegenerate mode solutions of even and odd nature for each polarization, analogous behavior to a coupled oscillator system. The z-component of the Poynting vector as well as the three components of the electric field are shown in Figure 3-5 for the four modes of a two-core fiber. Notice the two-fold degeneracy of the single core solution is broken when the two cores are brought together in a two-core fiber. The symmetric modes are the two modes with the largest

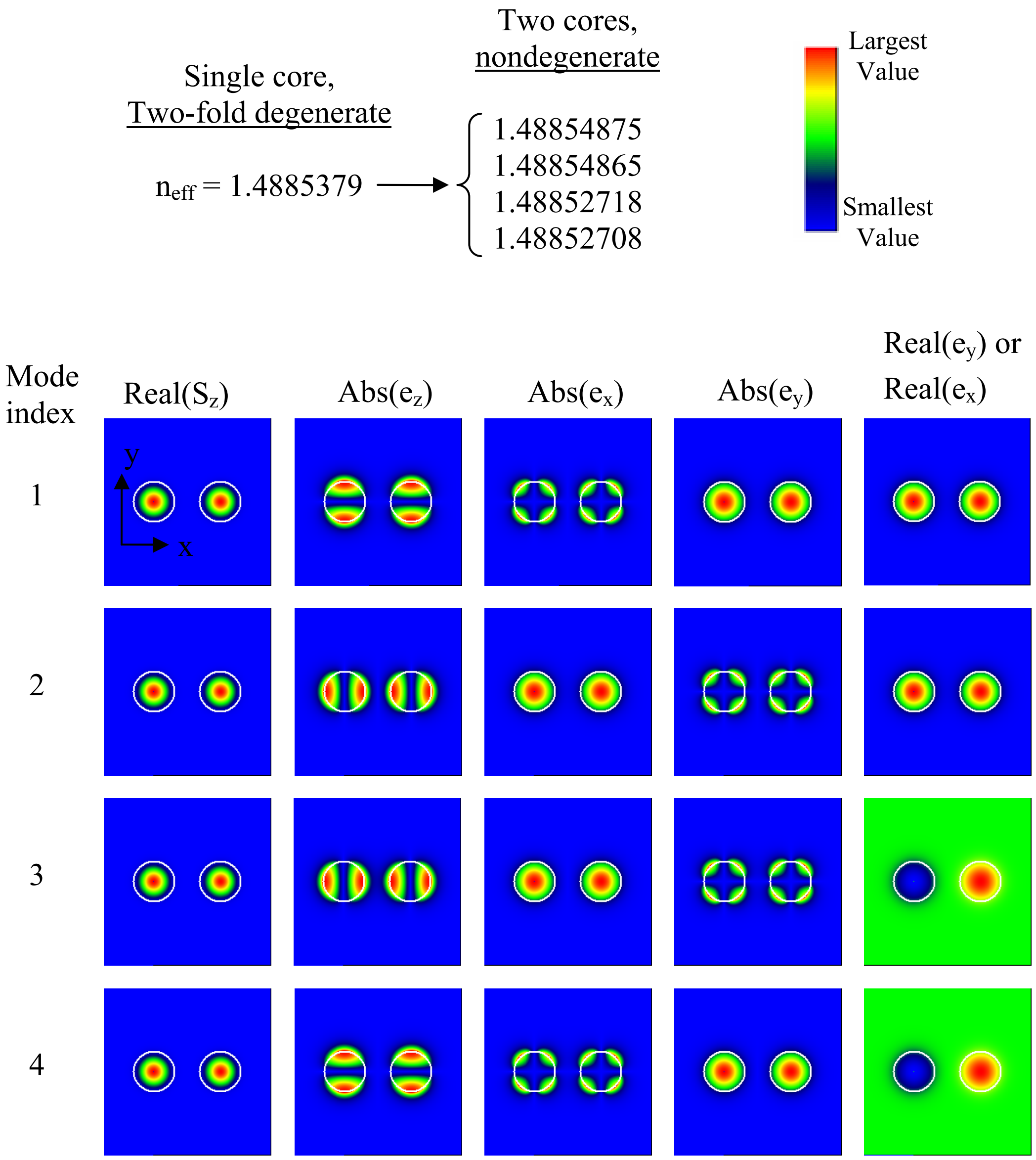

Figure 3-5. The four fundamental modes of a two-core fiber with core diameter of 2 μm and separation of 3.2 μm, λ = 600 nm. The mode index of 1 refers to the mode with the highest effective index. The colorbar is relevant for similar modal plots appearing in this dissertation.

effective indices, and two modes are predominantly x-polarized while two modes are predominantly y-polarized.

A more intuitive understanding of the normal mode expansion can be gained by considering a one-dimensional, single polarization or scalar example. In this case, the two fundamental modes of the two-core system are shown in Figure 3-6 (compare with modes 1 and 4 or modes 2 and 3 of Figure 3-5). The normal mode expansion of the scalar field solution in this 1D waveguide is shown in Eq. (3.5) for the electric and magnetic field.

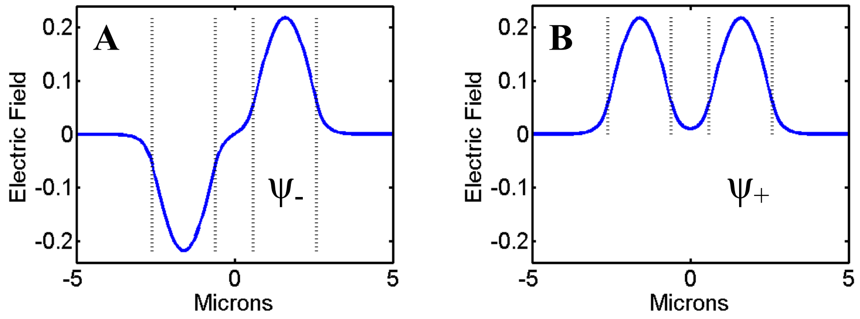

Figure 3-6. Odd a) and even b) modes, labeled ψ_- and ψ_+ respectively, of a two-core fiber for a single polarization. Dotted lines indicate the core boundaries.

$$\begin{aligned} E(x,z) &= a_+ e_+(x)_{sym} e^{in_+kz} + a_- e_-(x) e^{in_-kz} \\ H(x,z) &= a_+ h_+(x)_{sym} e^{in_+kz} + a_- h_-(x) e^{in_-kz} \end{aligned} \tag{3.5}$$

where the ‘+’ indicates a symmetric or even mode and the ‘–‘ corresponds to an antisymmetric or odd mode. Examining the field distributions in Figure 3-6, it is apparent that a single core input will have significant overlap with both the even and the odd mode, represented by the coefficients a_j. The energy coupled into each of these modes at the fiber endface will propagate at slightly different speeds along the fiber due to the splitting in the mode effective indices. The field solution at any point z is a linear combination of the even mode and the odd mode at that location in the fiber, as shown in Eq. (3.5). The resulting effect on the power in each core is the "beating" seen in Figure 3-2, where the input field is an x-polarized Gaussian, $E_y = 0$, that is centered on the left core with a spot diameter ($1/e^2$ intensity) equal to the radius of the core. For the case when the two cores are identical and the coupling efficiency is 100%, the period of the beat pattern is determined by the difference in the spatial frequencies of the modes, $k(n_+ - n_-)$ or $(\beta_+ - \beta_-)$, and can be written as a length:

$$L_c = \frac{\pi}{\beta_+ - \beta_-} = \frac{\lambda}{2(n_{eff}^+ - n_{eff}^-)} \tag{3.6}$$

where λ is the wavelength of light in vacuum. This distance is referred to as the beat length or coupling length and indicates the spatial separation between points where the modes of the fiber add in phase.

When the two cores of the fiber of Figure 3-5 are made to be non-identical, the coupling behavior can change drastically. For example, when the core diameters are different, the modal fields resemble the independent individual or decoupled cores, as shown in Figure 3-7. In Figure 3-7 the left core diameter has been increased by 1%. By examining the modal fields in Figure 3-7 it is obvious that an x-polarized input in the left core is most similar to a single mode, mode 2. The field expansion of Eq. (3.1) will contain essentially one mode and the energy distribution is no longer a strong function of z. In other words, light incident on a single core of the fiber in Figure 3-7 will couple almost completely into just one mode of the system and therefore not mix with other cores or modes along the length of the fiber.

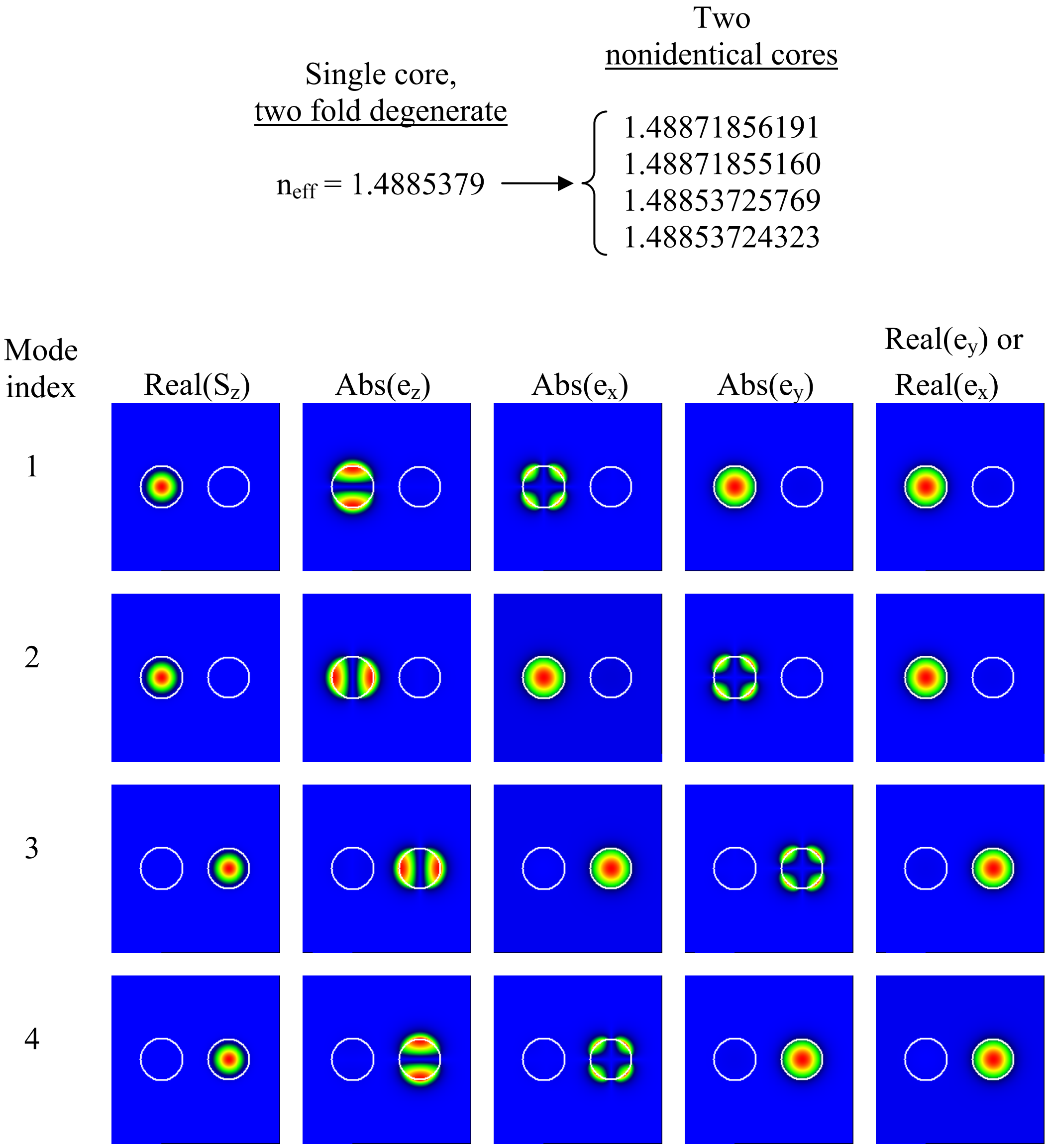

Figure 3-7. The four fundamental modes of a two-core fiber with right core diameter of 2 μm, left core diameter of 2.02 μm, and separation of 3.2 μm, λ = 600 nm.

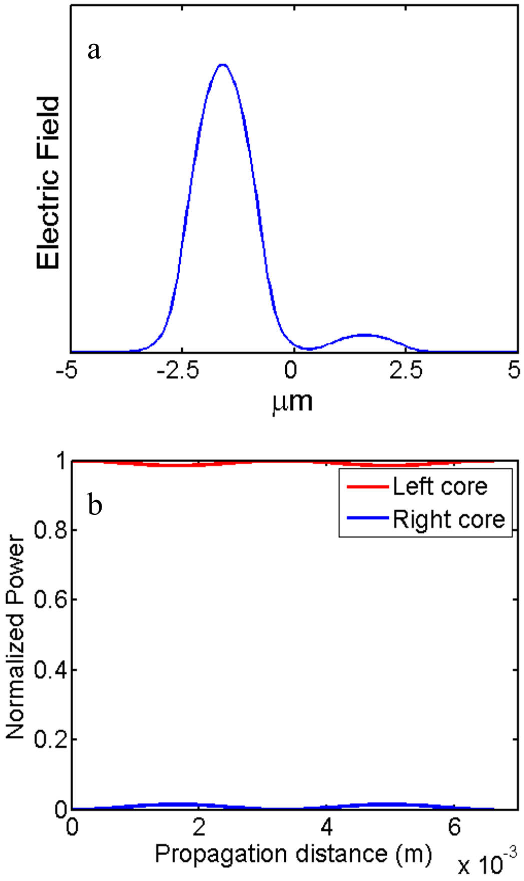

Figure 3-8. Plot a) shows the distribution of the field between the cores for mode 1 of the fiber in Figure 3-7. The power as a function of the propagation distance is plotted in b). The coupling length is 1.6545e+003 microns and the coupling efficiency is 1.47%.

As can be seen in Figure 3-8(a), the cores are not completely decoupled; therefore, a small amount of the power oscillates as a function of the propagation distance, as shown in Figure 3-8(b). The coupling length is also reduced and in this case, and the amount of power that is transferred between the cores is only 1.47%. The cores behave essentially independently because the difference between adjacent core diameters has created a mode mismatch that will inhibit coupling. Light incident initially on a single core will remain mostly in that core as it propagates down the fiber.

Coupled mode theory

The coupling behavior in two-core fibers can also be determined by using coupled mode theory (CMT). CMT is commonly used for obtaining approximate analytical solutions to systems of coupled waveguides, such as multi-core fibers. In CMT, each core is solved for independently and interactions with neighboring cores are treated as a perturbation [10-12]. In the case of weak coupling, CMT approximates the total field in the fiber as a linear superposition of the mode solutions of the individual cores, call them *a* and *b*, as shown in Eq. (3.7).

$$\begin{aligned} \vec{E}(x,y,z) &= a(z)\vec{E}^a(x,y) + b(z)\vec{E}^b(x,y) \\ \vec{H}(x,y,z) &= a(z)\vec{H}^a(x,y) + b(z)\vec{H}^b(x,y) \end{aligned} \tag{3.7}$$

This concept is represented pictorially at the top of Figure 3-9. The strength of the coupling between the cores is quantified by the coupling coefficient, K_{ab}, which depends on the area of overlap of the individual core modes in one of the cores. An exaggerated illustration of this overlap appears at the bottom of Figure 3-9. If light is

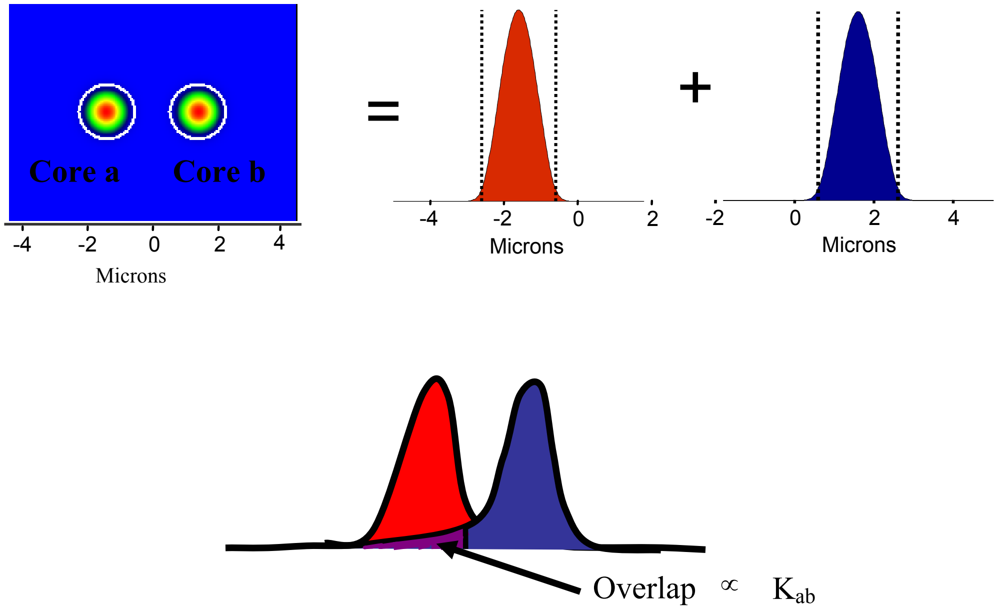

Figure 3-9. The coupled mode theory representation of a two-core fiber as a linear combination of the individual core modes. At bottom, an exaggerated view of the overlap between these modes in one core is shown. This overlap determines the strength of the coupling.

incident initially on core *a*, the coupling coefficient can be determined by Eq. (3.8) [11]:

$$K_{ab} = \frac{\omega\varepsilon_0}{4}\left(n_{co}^2 - n_{cl}^2\right)\cdot \iint\limits_{Area_a} \left[E_r^b(r,\theta)E_r^a(r,\theta) + E_\theta^b(r,\theta)E_\theta^a(r,\theta) - E_z^b(r,\theta)E_z^a(r,\theta)\right]\cdot r dr d\theta \tag{3.8}$$

where the fields represent the fundamental mode of each core, centered on the respective core, and have been normalized such that

$$1 = \frac{1}{2}\iint \vec{E}_t \times \vec{H}_t \cdot \hat{z}\ r dr d\theta \tag{3.9}$$

The power as a function of z is calculated from the fields in Eq. (3.7) as shown in Eq. (3.10).

$$\begin{gathered}
P(z)=\tfrac{1}{2}\operatorname{Re}\iint \vec{E}(x,y,z)\times\vec{H}^{*}(x,y,z)\cdot\hat{z}dxdy \\
P(z)=\left|a(z)\right|^{2}+\left|b(z)\right|^{2}+\operatorname{Re}\left[a(z)b^{*}(z)C_{ab}+b(z)a^{*}(z)C_{ba}\right] \\
C_{ab}=\tfrac{1}{2}\iint \vec{e}^{\,a}(x,y)\times\vec{h}^{b}(x,y)\cdot\hat{z}dxdy
\end{gathered}\tag{3.10}$$

In the weak coupling regime, or conventional CMT, the cross field power (the terms in Eq. (3.10) containing the cross field integrals, C_{ab} and C_{ba}) is ignored and the power is determined by *a*(*z*) and *b*(*z*). Although this is strictly only true when $K_{ab} = K_{ba}^{*}$ and the cores are identical, this approximation is valid when C_{ab} and C_{ba} are very small and $K_{ab} \approx K_{ba}^{*}$. The amplitude coefficients of the modes of the two cores obey the coupled amplitude equations of Eq. (3.11) as derived from the general reciprocity relation or through the variational method [11, 13].

$$\begin{gathered}
\frac{d}{dz}a(z)=i\beta_{a}a(z)+iK_{ab}b(z) \\
\frac{d}{dz}b(z)=iK_{ba}a(z)+i\beta_{b}b(z)
\end{gathered}\tag{3.11}$$

In conventional CMT, β_a and β_b are the propagation constants for the individual, independent waveguides and the coupling coefficients, K_{ba} and K_{ab}, are proportional to the overlap integral of the mode fields of the individual waveguides in each core [11, 14]. Improved CMT considers the situation where K_{ab} and K_{ba} are very different, therefore second order terms are added to the constants in Eq. (3.11) and the cross field power is included in order to conserve power [11, 14].

Solving the system of equations in Eq. (3.11) and applying the initial condition that light is incident on waveguide *a* at z = 0, or *a*(0) = 1 and *b*(0) = 0, produces the expressions for the power given in Eq. (3.12) when the cross power is neglected [14].

$$
\begin{aligned}
P_a(z) &= |a(z)|^2 = 1 - F^2 \sin^2 \beta_d z \\
P_b(z) &= |b(z)|^2 = \frac{K_{ab}}{K_{ba}} F^2 \sin^2 \beta_d z \\
F &= \frac{1}{\sqrt{1 + \dfrac{(\beta_a - \beta_b)^2}{4K_{ab}K_{ba}}}} \\
\beta_d &= \frac{\sqrt{K_{ab}K_{ba}}}{F}
\end{aligned}
\tag{3.12}
$$

The maximum power transferred out of waveguide *a*, or the coupling efficiency, is F^2 and β_d is related to the beat frequency or the rate of power transfer. The coupling length is the distance, L_c, at which the power in waveguide *b* has oscillated to its first maximum, ie. $\beta_d L_c = \pi / 2$. When the two cores are identical, F = 1 and the coupling length is found directly from K_{ab} according to Eq. (3.13).

$$L_C = \frac{\pi}{2K_{ab}} \tag{3.13}$$

This coupling length is equivalent to the beat length of Eq. (3.6). A small amount of mode overlap will lead to a relatively small value for K_{ab} and therefore a long coupling length, indicating weaker coupling. For non-identical cores, as the mismatch between the modes of the individual cores, β_a-β_b or $\Delta\beta$, increases, Eq. (3.12) also dictates that the coupling efficiency and the coupling length will decrease, as observed previously using the normal mode expansion.

There has been much discussion over the last two decades concerning the limitations of conventional CMT and the regimes for which ICMT is necessary [14-16]. In addition, polarization correction terms and a vector CMT have been proposed for strongly coupled waveguides [15, 17, 18]. Because the simplicity of conventional

CMT has its advantages, the cross field power is typically ignored and the consequences of this assumption are assessed.

Conclusion

The two methods presented in this chapter for determining the coupling behavior in a multi-core fiber or a multiple waveguide system each have their advantages. Because CMT relies on the solutions of the independent waveguides, it can provide a quick and simple estimate without substantial computational requirements. However, the validity of conventional CMT is often uncertain and is limited to specific regimes. The normal mode expansion method provides a more exact, though numerically intensive, description regardless of the strength of the coupling. The work presented in this dissertation examines the effects of core mismatch on the coupling properties of multi-core fibers. By approaching this situation using the normal mode expansion technique, and by later applying CMT to these results, the validity of CMT is assessed in different regimes of coupling strength. In this manner, the simple expressions of CMT are proven to provide a reliable tool for predicting the coupling behavior of the types of fibers studied.

Chapter 4

PHOTONIC CRYSTALS AND PHOTONIC CRYSTAL FIBERS

Introduction

In the late 1990s, a new class of fibers called photonic crystal fibers was developed out of research in the field of photonic crystals [19-21]. The conception of photonic crystals is founded on an analogy with crystalline solids which are composed

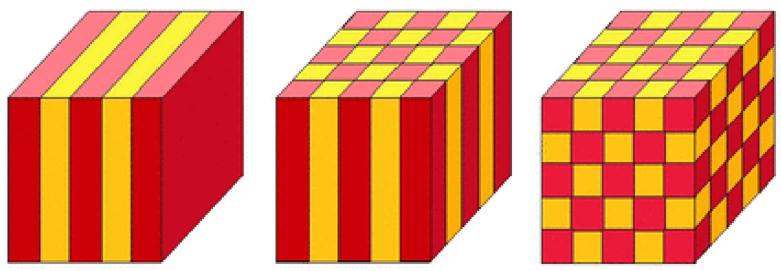

1D
Periodic in one direction

2D
Periodic in two directions

3D
Periodic in three directions

Figure 4-1. Illustrations of one, two, and three dimensional photonic crystals. Different colors represent materials with different dielectric constants.

of a periodic array of atoms or molecules that can be modeled as a periodic potential [22, 23]. Photonic crystals are formed by arranging dielectric materials in a periodic array or lattice with lattice spacing on the order of the wavelength of light. See Figure 4-1 for example illustrations of multidimensional photonic crystals [24].

Just as crystalline solids have electronic band gaps, photonic crystals have photonic band gaps, representing bands of wavelengths that are forbidden or unable to propagate in the crystal. 1D photonic crystals, such as Bragg stacks and optical gratings, have been used extensively for over a hundred years because of their interesting reflection properties that result from constructive and deconstructive interference of light as it reflects off different dielectric layers. 2D photonic crystals have found two main applications in planar and fiber waveguides. Planar photonic crystal waveguides are fabricated with a high index defect or channel in the same geometric plane as the photonic crystal as shown in Figure 4-2(a); that is, the dielectric periodicity occurs in the same plane as the fabricated waveguide. These waveguides have been studied for use in integrated photonics and for their ability to manipulate light around sharp bends in addition to other applications [25]. Photonic crystal fibers are produced in much the same manner as a standard fiber except the cladding is replaced by a photonic crystal. The guiding structure is a high or low index defect in the photonic crystal that is created perpendicular to the dimensions of dielectric periodicity. 3D photonic crystals have potential applications as resonant cavities, for localization of light, and for the suppression of spontaneous emission [22-24]

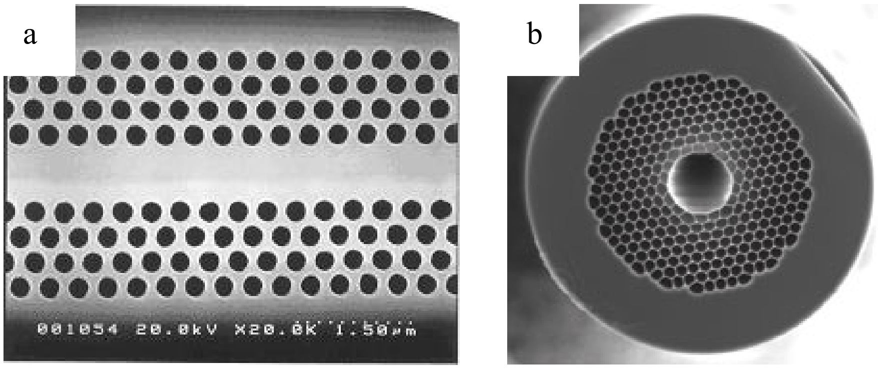

Figure 4-2. Picture of planar photonic crystal waveguide a) [www.imperial.ac.uk/research/exss/research/semiconductor/photonic/-index.htm] and a photonic bandgap fiber b) [www.photonics.com/content/-spectra/2004/April/research/77495.aspx].

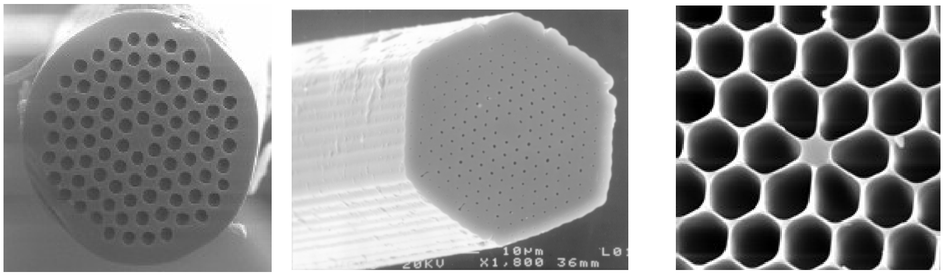

Figure 4-3. Three images of photonic crystal fibers where light propagates in a high index core region due to modified total internal reflection. [imfc.univ-fcomte.fr/lopmd/onl/frameonl2.htm, www.bath.ac.uk/physics/groups/opto-/pcf.html, www.crystal-fibre.com/products/nonlinear.shtm].

Two types of photonic crystal fibers, sometimes referred to as microstructured optical fibers (MOFs) or holey fibers, are distinguished by the method of light propagation [26-29]. In photonic band gap fibers, light propagates in a low index core region that is surrounded by a photonic crystal cladding (see Figure 4-2(b)). Light entering the fiber will be confined to propagate in the core if it is of a wavelength that falls within the band gap of the surrounding photonic crystal because it will be forbidden to leak out through the cladding [21, 30-32]. These fibers are being used primarily as sensors [33], for dispersion management [34], and for high peak power laser delivery [35].

The second class of fibers, commonly referred to as just photonic crystal fibers (PCFs), are the topic of this chapter. Images of this type of fiber appear in Figure 4-3. PCFs are typically composed of a single material such as silica and the most common arrangement of air holes is in a triangular lattice as shown in the fibers of Figure 4-2 and Figure 4-3. Propagation is along the axis of the fiber and is achieved through creation of a high index defect in the periodic lattice, typically silica. PCFs guide light by a process referred to as modified total internal reflection, which can be understood through an analogy with step index fibers [36]. PCFs are sometimes used in applications to replace step-index fibers but have additional applications due to the unique features of these fibers, such as adjustable dispersion [37], high nonlinearity [38], and endlessly single-mode propagation [29].

Photonic crystal fibers

Figure 4-4 compares propagation in a conventional fiber, as described in Chapter 2, with that in a PCF. Because the PCF core is of higher index than the

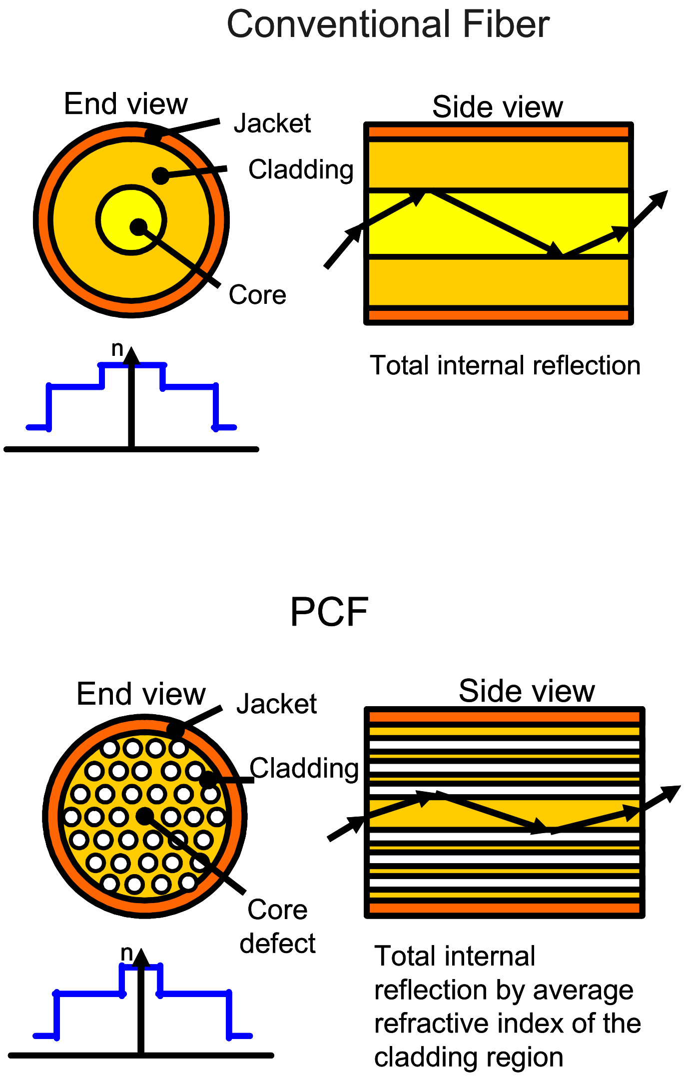

Figure 4-4. Propagation by means of total internal reflection in a conventional step index fiber is compared with propagation in a photonic crystal fiber. [www.bath.ac.uk/physics/groups/opto/pcf.html]

average index of the cladding, these types of PCFs can be compared to a step index fiber with a wavelength dependent cladding index [36, 39]. This average cladding index is defined as the effective index of the highest index mode of the infinite photonic crystal cladding, which changes depending on the wavelength of light. The wavelength dependence can be understood intuitively by considering two cases for an infinite photonic crystal with no defects. For a wavelength of light much shorter than the dimensions of the lattice (i.e. the air hole diameter and separation), the small spaces between the air holes will be able to be resolved by the light and it will propagate confined mostly to the silica, resulting in a mode index very near the index of the silica core. When the size of the wavelength is near to the scale of the lattice, the light will diffract across the boundary of the air holes and propagate in both index regions, thus reducing the effective index experienced by the propagating mode. The largest wavevector that will propagate in the infinite lattice, $k_o n_{fsm}$, thus depends on the size of the wavelength relative to that lattice and is defined as the fundamental space filling mode (FSM). This wavevector replaces the left side of the inequality previously mentioned in Chapter 2 for total internal reflection that shows the limiting values of β for bound modes, or $k_o n_{fsm} < \beta < k_o n_{co}$.

The modeling of a PCF as a step index fiber (SIF) is referred to as the scalar effective-index method. This model is useful for approximating the properties of a PCF without the complicated vector mode solvers required in order to take into account the complex array of dielectric boundaries in the cross-section of these fibers [36, 39]. Mode solutions can thus be determined by solving the scalar wave equation from in Chapter 2. This model is most accurate for shorter wavelengths on the order of the air hole separation or pitch, Λ, because the mode is well-confined. As shown in Figure 4-5, a PCF is modeled as a SIF with a core radius of ρ_c, and the cladding index

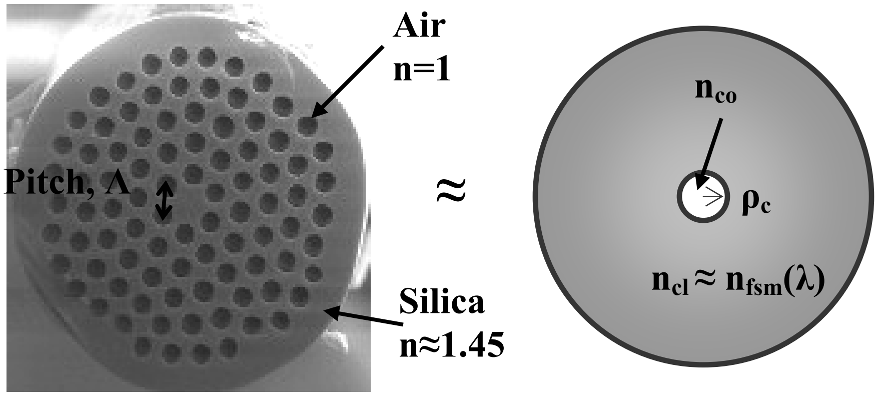

Figure 4-5. A scanning electron microscope image of a PCF with a high index central defect and the equivalent step index fiber, according to the effective index approach.

is n_{fsm}, which has been previously defined. The index of the FSM can be determined accurately only through fully vectoral numerical simulations of the photonic crystal lattice [40]; however, a scalar approximation is recommended by Birks et al. [39] for small air hole fibers and an empirical model has been developed by Saitoh and Koshiba [41]. The definition of ρ_c is not standardized and has been defined in several ways, as a fraction of the pitch 0.64Λ [42] or as $\Lambda/\sqrt{3}$ [41, 43], and as a function of the relative air hole size, d/Λ [44], where d is the air hole diameter.

The main advantage of the analogy between a PCF and a SIF is that established knowledge of the simple SIF can be utilized for predicting the behavior of this new type of fiber [36, 39, 41, 43, 45-47]. For instance, several properties such as the mode field radius, bend loss, the numerical aperture, splice loss, and beam divergence can be calculated from the V-parameter of a step-index fiber and these formulas can be applied to a PCF using the effective index model [41, 43, 45, 46, 48]. A V-parameter for a PCF, V_{PCF}, has been defined by Mortensen et al. [45, 49] as:

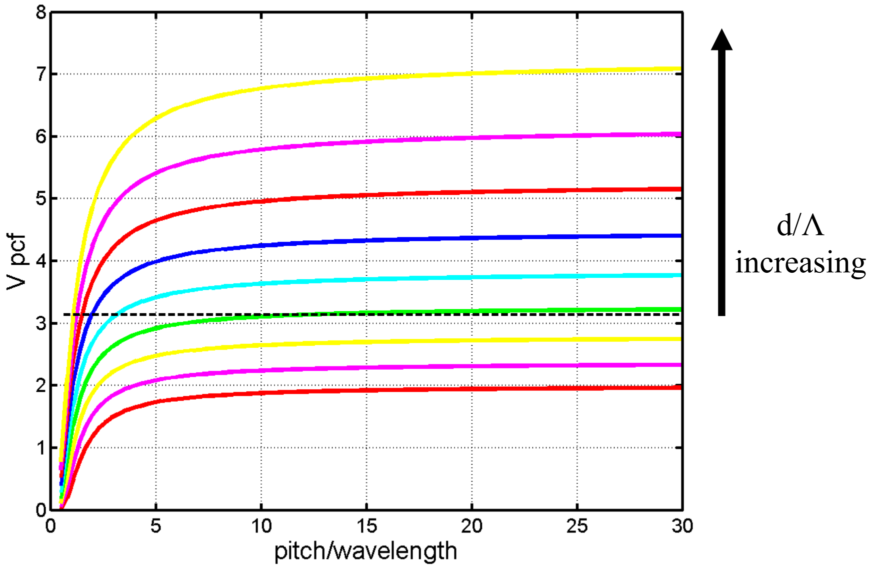

Figure 4-6. V_{PCF} is plotted versus the normalized pitch for d/Λ = [0.3 0.35 0.4 0.45 0.5 0.55 0.6 0.65 0.7]; V_{PCF} increases as d/Λ increases.

$$V_{PCF}(\lambda) = \frac{2\pi}{\lambda}\Lambda\sqrt{n_{co}^2(\lambda) - n_{cl}^2(\lambda)} \tag{4.1}$$

where n_{co} is the effective index of the fundamental mode and n_{cl} is n_{fsm}, both a function of the wavelength. Unlike a standard step-index fiber, the fundamental mode cutoff occurs when $V_{PCF} = \pi$ [45, 47, 49]. An alternative definition of V_{PCF}, which has a fundamental mode cutoff at the same value as a standard SIF, has been used by Saitoh and Koshiba for predicting several properties of PCFs such as the mode field radius, the nonlinear coefficient, and dispersion [41, 43]. In Figure 4-6, V_{PCF} as defined in Eq. (4.1) is plotted versus the normalized wavelength and as a function of the relative air hole size, d/Λ.

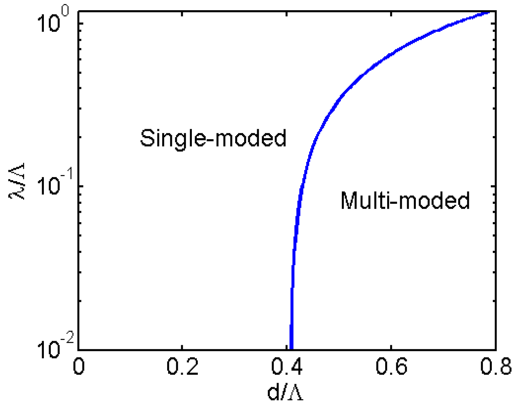

Figure 4-7. The phase boundary between the fundamental and second mode is plotted for the air hole size and the normalized wavelength.

Figure 4-6 illustrates the endlessly single mode behavior that occurs in certain PCFs. Below approximately d/Λ = 0.41, V_{PCF} will never cross the mode boundary at $V_{PCF} = \pi$. The phase boundary between the fundamental and second mode is shown in Figure 4-7 [45, 47, 49].

This endlessly single mode property of small air hole PCFs can be understood intuitively by returning again to the wavelength dependence of the cladding index of a PCF equivalent SIF. In a conventional SIF, decreasing the wavelength will reduce the mode field area and as the mode becomes better confined in the core the number of modes will increase. For a PCF, decreasing the wavelength will bring the index of the cladding closer to the index of the core—a smaller wavelength will sample more of the silica in the cladding resulting in a higher index for the FSM—and the light will experience a lower index contrast. In other words, as Λ/λ increases the Δn between the core and the cladding indices will decrease, resulting in weaker mode confinement. Thus, the mode field area will not decrease in the same manner as a SIF and two competing effects will essentially balance out for certain fibers. Endlessly singe mode behavior has also been verified through fully vectoral simulations.

An important distinction exists between the modes of a SIF and those of a PCF. Because confinement in a SIF is caused by perfect total internal reflection, a finite set of real propagation constants exists as bound solutions to the scalar wave equation. Due to the finite extent of the photonic crystal cladding that surrounds the core of a PCF, the modes are actually “leaky” modes as evidenced by their complex propagation constants. The modes of a PCF are only perfectly confined if the photonic crystal lattice cladding is infinite. Otherwise, light experiences loss as it propagates down a PCF. As the number of rings of air holes surrounding a core increases, the loss decreases. The loss is also reduced if the relative air hole size is larger because the mode becomes more confined and will extend less into the cladding [50-53].

Due to their unique properties, PCFs and other similar microstructured fibers have found applications in several areas of optics. There is specific interest in the endlessly single mode capabilities of these fibers since single mode propagation is preferred for telecom as well as many other applications. In addition, because a higher core-cladding index contrast can be achieved in fibers composed only of air and silica, tight mode confinement can result in a nonlinear index that is much higher than conventional fibers or the structure can be modified to confine light to much larger areas resulting in high numerical aperture fibers. Other applications take advantage of the large number of adjustable parameters in a PCF cross-section to create high birefringence fibers, dispersion compensating fibers, and dispersion shifted fibers [28, 29]. The development of PCFs with unique dispersion profiles and high nonlinearity have allowed for major advances in nonlinear fiber optics such as super continuum generation [54].

Several vector methods exist for predicting the properties of PCFs. Localized basis function method, biothornormal-basis method, Fourier-decomposition method, full-vectoral plane-wave expansion method, and the multipole method [28, 55] are just a few of the methods developed in response to the advancement of PCFs. The plane-wave expansion method is highly accurate and the most widely used of these methods [28]. It is best for infinite structures due to the use of periodic boundary conditions; however, the loss of the mode cannot be determined, nor can the guiding properties when the photonic crystal lattice cladding is not very extensive as compared to the wavelength. Finite-element method [42], finite-difference, and beam propagation method [56, 57], which are commonly used for general electromagnetic problems, have also been applied to PCFs [55]. The finite element method is especially useful for modeling PCFs with non-circular air holes or otherwise non-symmetric structure [58]; however, it is a computational intensive method. The multipole method is advantageous because it is able to farely quickly determine the solutions for a finite structure and the loss of a fiber can be predicted. The next chapter will explain the multipole method in more detail; this method was used for the research presented in this dissertation.

Chapter 5

THE MULTIPOLE METHOD

Introduction

In order to accurately model the photonic crystal fiber structure, a fully vectoral method for solving the wave equation is required due to the complicated arrangement of index boundaries that make up a PCF. Several numerical simulation methods have been developed and tested to meet this challenge [28, 55]. One advantage of the multipole method over other methods is the ability to take into account the finite nature of the fiber cladding. The multipole method is not limited by periodic boundary conditions, and can therefore predict the complex propagation constants that describe the modes in these types of fibers [29]. Unlike the finite-element method, the multipole method has been demonstrated to be extremely accurate without unreasonable computation times. Although the multipole method was developed to solve for the modes of photonic crystal fibers, any waveguide with more than one circular index boundaries lends itself well to this method, such as waveguides with high or low index cores. The multipole method has been used by the author to simulate high-index defect photonic crystal fibers (PCFs) and multi-core fiber bundles. The method and implementation will be described in this chapter.

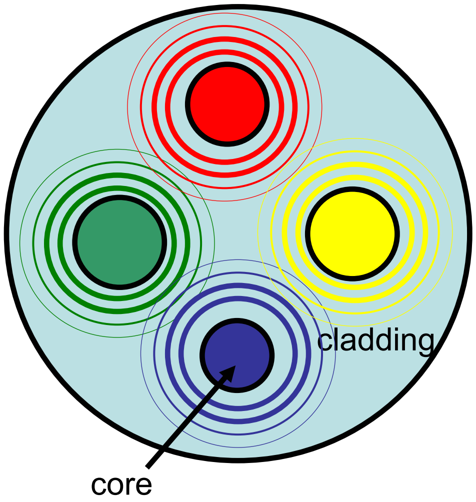

Figure 5-1. Illustration of each core in a fiber as a scattering or radiating source of electromagnetic field.

Multipole method

In the multipole method (MM), each core is considered as a scatterer of electromagnectic fields [59-61]. Because the boundaries for these cores scatter electromagnetic waves, they can also be viewed as sources. An illustration of several cores as scattering sources in a fiber is shown in Figure 5-1. The multipole method is founded on the description of the field at any point in the fiber as the superposition of the fields sourced or radiated from each of these cores and the reflection of this field off of the cladding boundary, as represented pictorially in Figure 5-2. Figure 5-3 defines the coordinate systems to be used in the more detailed derivation that follows. The multipole method as presented here is limited to circular index boundaries,

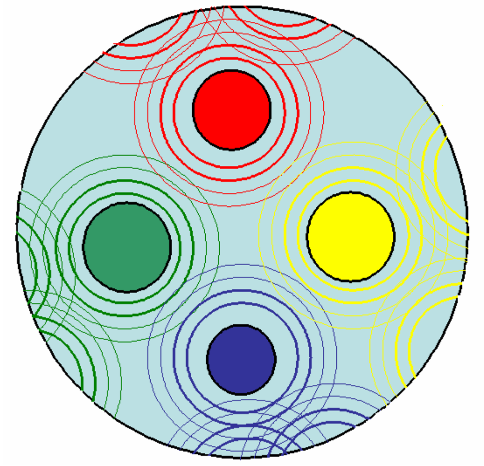

Figure 5-2. Pictoral representation of the Wijnaard or global expansion, used in the multipole method as an expression of the field solution.

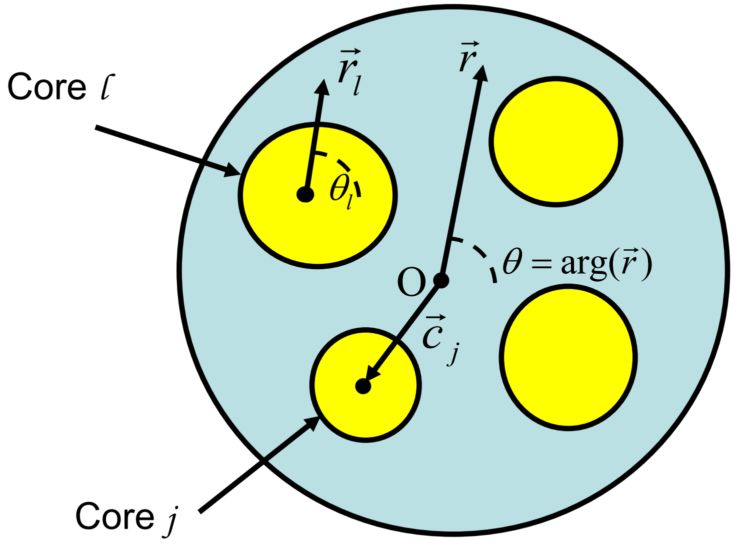

Figure 5-3. End view of a fiber with multiple cores. Local (with subscript l and the core center as the origin) and global (with point O as the origin) coordinate systems have been defined.

although this restriction is not inherent to the method [62]. The complication of allowing elliptically shaped cores has not been added to the programs used. Several sources have been consulted in order to present the multipole method theory in this chapter [29, 59, 63]

Solving the wave equation using the multipole method begins in a similar manner to the method described in Chapter 2 for a step-index fiber. Again, cylindrical coordinates are used and solutions to the scalar wave equation for the z-component of the field can be used to obtain the vector field; however, amendments to the method presented in Chapter 2 must be made in order to allow complex modal solutions and the interaction of multiple cores. First, β is defined as the speed of propagation of the mode in the z-direction, and the wave equation becomes the Helmholtz equation, written as

$$\left(\Delta + k_{\perp}^{2}\right) F = 0 \tag{5.1}$$

where $k_{\perp} = \sqrt{k^2 n^2 - \beta^2}$, n is the index of the core or cladding, and F is either the electric or the magnetic field. The field is then expanded as a Fourier-Bessel series:

$$F(r,\theta) = \sum (A_n J_n(k_{\perp} r) + B_n H_n^{(1)}(k_{\perp} r)) \exp(in\theta) \tag{5.2}$$

where $J_n(r,\theta)$ is Bessel's function of the first kind and $H_n^{(1)}(r,\theta)$ is Hankel's function of the first kind, a complex combination of Bessel's functions of the first and second kind.

A more intuitive understanding of the MM can be gained by interpreting the behavior of the fields represented by Bessel and Hankel functions. Bessel's functions of the first and second kind are plotted in Figure 5-4. Hankel functions are a complex combination of these two functions and have a singularity at x = 0. Consider, for example, the field in a circular donut-shaped region in the waveguide of Figure 5-3 surrounding the origin that does not include any cores. The Hankel functions represent outgoing waves or fields radiated from sources near the origin or inside the donut center; the sources are not contained in the region but are surrounded by the region. These fields can only be expanded in Hankel functions and are represented by a set of coefficients B_n in Eq. (5.2). Bessel's function of the first kind is plotted in Figure 5-4(a) and is regular everywhere; therefore, these functions describe radiated fields with coefficients A_n where the source is located beyond or outside the region. Whether or not a field is considered regular or outgoing is thus determined by the local coordinate system, or the system centered at each core. For example, a field that is considered outgoing from one perspective will be interpreted as regular in a region whose system is displaced from the original system. Graf's theorem is used to generate a matrix to transform between coordinate systems and, consequently, types of fields as $\mathcal{A}=\mathcal{H}\mathcal{B}$. See the following reference [29] for an explanation of Graf's addition theorem and additional resources.

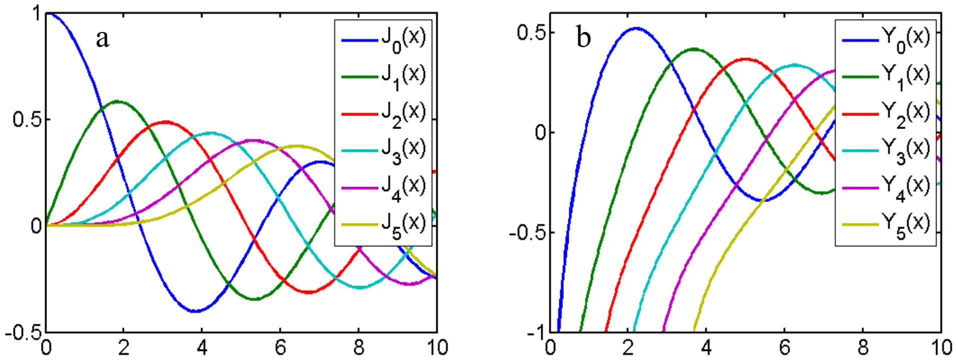

Figure 5-4. Plots of Bessel functions of the first (a) and second (b) kind.

Considering each circular index boundary, or core, in a fiber as a source or identically as a scatterer, the region outside a core will contain both types of fields. A regular field from an external source entering the region around a core will be scattered at the index boundary, thus radiating away as an outgoing field. A reflection matrix will generate the outgoing field from the incident regular field, $\mathcal{R}\mathcal{A}=\mathcal{B}$. When multiple cores are contained in a system, the regular field near a core will be the sum of fields from any external source and the reflected regular fields outgoing from other cores which act like sources. The outgoing field from that same core will be the reflected regular field. Using the MM, a multi-core waveguide becomes a complex system of interfering, scattered fields. In the absence of an external source, the solutions or steady states are the modes of the system. With this intuitive understanding of the MM, it can now be developed more rigorously into a useful numerical tool.

The mathematical foundation of the MM is based on the forced consistency of two expressions for the field—one from a local perspective and the other from a global perspective. First, near the j$^{\text{th}}$ core, the fields are described by a local expansion that is written in the local coordinates of the core:

$$E_z = \sum_m \left[A_m^{Ej} J_m(k_\perp r_j) + B_m^{Ej} H_m^{(1)}(k_\perp r_j) \right] \exp(im\theta_l) \tag{5.3}$$

The local coordinates are defined by polar axes centered on each core, or $\vec{r}_j = \vec{r} - \vec{c}_j$, where $\vec{c}_j$ is the location of core j in the global coordinate system of $\vec{r}$ (see Figure 5-3). The magnetic field can be written in the same manner as in Eq. (5.3) but with different coefficients. In order for expressions of the electric and magnetic field to have identical form, a scaled magnetic field $K = ZH$, $Z = \sqrt{\mu_0 / \varepsilon_0}$, replaces the actual magnetic field in all calculations and the coefficients for the magnetic field are

A_m^{Kj} and B_m^{Kj}. Equation (5.3) states that the field around a core is due to sources within the region (outgoing or scattered field that appears to be sourced at the local core) and outside the region (regular field that contains the radiated field from all other cores).

A global expansion of the fields that is valid everywhere is based on the work of Wijngaard [29, 59].

$$\begin{aligned} E_z = &\sum_{j=1}^{N}\sum_{m} B_m^{Ej} H_m^{(1)}(k_\perp \left|\vec{r}_j\right|) \exp(im\arg(\vec{r}-\vec{c}_j)) \\ &+\sum A_m^{E0} J_m(k_\perp r)\exp(im\theta) \end{aligned} \tag{5.4}$$

In Eq. (5.4) , the field is described as a superposition of the outgoing waves sourced at all N cores (and propagating away from each of the cores) and the field reflected from a jacket surrounding the cores, of index 0, which appears to be sourced outside the region and is therefore regular. This expansion was represented pictorially in Figure 5-2. For additional discussion of the Wijngaard expansion see reference [29].

Setting Eq. (5.3) equal to Eq. (5.4) yields the following expression, where the outgoing field from core ℓ has been cancelled from both sides:

$$\begin{aligned} \sum_{m} A_m^{El} J_m(k_\perp r_l)\exp(im\theta_l) = &\sum_{\substack{j=1 \\ j\neq l}}^{N}\sum_{m} B_m^{Ej} H_m^{(1)}(k_\perp r_j)\exp(im\theta_j) \\ &+\sum A_m^{E0} J_m(k_\perp r)\exp(im\theta) \end{aligned} \tag{5.5}$$

Because each term in these sums refers to a different origin or local coordinate system, the $\mathcal{H}$ matrix generated through Graf's addition theorem, as referred to previously, must be employed for these basis transformations. Therefore, the outgoing field from core j contributes to the local regular field near core ℓ through the following transformation:

$$\begin{aligned}
&\sum_n A_n^{Elj} J_n(k_\perp r_l)\exp(in\arg(\vec{r}_l)) = \sum_m B_m^{Ej} H_m^{(1)}(k_\perp r_j)\exp(im\arg(\vec{r}_j)) \\
&A_n^{Elj} = \sum_m \mathcal{H}_{nm}^{lj} B_m^{Ej} \\
&\mathcal{H}_{nm}^{lj} = H_{n-m}^{(1)}(k_\perp c_{lj})\exp(-i(n-m)\arg(\vec{c}_{lj}))
\end{aligned} \tag{5.6}$$

and $\vec{c}_{lj} = \vec{c}_j - \vec{c}_l$. For the derivation of the elements $\mathcal{H}_{nm}^{lj}$, see references [29, 59].

In order to simplify the notation and to facilitate the implementation of these equations into a numerical program, coefficients and operators will now be reformulated as vectors and matrices. A_n^{Ej} still represents a numerical value but now it is just the nth element in the vector $\boldsymbol{A}^{Elj}$ with length of M. Similarly, $\mathcal{H}_{nm}^{lj}$ is an element in the M x M matrix $\boldsymbol{\mathcal{H}}^{lj}$ which performs basis transformations between the local systems of cores ℓ and *j*. The integer M is the number of terms in the multipole expansion from –*m* to *m*, including zero; therefore, M = 2 x multipole order +1. The sum over *m* no longer needs to be written as it is implicit to the matrix multiplication. The transformation of Eq. (5.6) can then be rewritten as:

$$\boldsymbol{A}^{Elj} = \boldsymbol{\mathcal{H}}^{lj}\boldsymbol{B}^{Ej} \tag{5.7}$$

In a similar manner, the field due to the jacket, as referred to in Eq. (5.5), can also be written in the local coordinate system of core ℓ.

$$\sum_n A_n^{El0} J_n(k_\perp r_l)\exp(in\theta_l) = \sum_m A_m^{E0} J_m(k_\perp r)\exp(im\theta) \tag{5.8}$$

Using matrix notation for the basis transformation:

$$\begin{aligned}
\boldsymbol{A}^{El0} &= \boldsymbol{\mathcal{J}}^{l0}\boldsymbol{A}^{E0} \\
\mathcal{J}_{nm}^{l0} &= (-1)^{(n-m)} J_{n-m}(k_\perp c_l)\exp(i(n-m)\arg(\vec{c}_l))
\end{aligned} \tag{5.9}$$

When Eq. (5.6) and Eq. (5.8) are substituted into Eq. (5.5), all fields are now expressed in the local coordinates of core ℓ and $J_n(k_\perp r_l)\exp(in\arg(\vec{r}_l))$ is common to all sums in the expression. Eq. (5.5) can be simplified to the following matrix expression for the coefficients:

$$\boldsymbol{A}^{El} = \sum_{\substack{j=1 \\ j\neq l}}^{N} \boldsymbol{A}^{Elj} + \boldsymbol{A}^{El0} = \sum_{\substack{j=1 \\ j\neq l}}^{N} \mathcal{H}^{lj}\boldsymbol{B}^{Ej} + \mathcal{J}^{l0}\boldsymbol{A}^{E0} \tag{5.10}$$

Eq. (5.10) represents the regular incident field at core ℓ in terms of the outgoing waves from other cores and the reflected field off the jacket.

Eq. (5.10) is valid for both the E_z and the K_z fields. In anticipation of the complication that would be added to a modeling program if the electric and the magnetic fields needed to be computed separately, they are combined at this time into a single expression. The new vector $\boldsymbol{A}^l$ has a length of 2M and the first M elements describe the electric field while the next M elements correspond to the K_z field, or $\boldsymbol{A}^l = [\boldsymbol{A}^{El};\boldsymbol{A}^{Kl}]$ and likewise for the $\boldsymbol{B}^l$ coefficients. The matrix $\mathcal{H}^{lj}$ is rewritten as the block diagonal matrix $\tilde{\mathcal{H}}^{lj}$ with dimensions 2M x 2M, containing the two matrices $\mathcal{H}^{lj}$, for each type of field in a manner that does not mix the coefficients.

$$\tilde{\boldsymbol{A}}^{l} = \sum_{\substack{j=1 \\ j\neq l}}^{N} \tilde{\mathcal{H}}^{lj}\tilde{\boldsymbol{B}}^{j} + \tilde{\mathcal{J}}^{l0}\tilde{\boldsymbol{A}}^{0} \tag{5.11}$$

In addition, the sum over N can be eliminated as well. For a system with N cores, $\mathcal{A} = [\tilde{\boldsymbol{A}}^1;..\tilde{\boldsymbol{A}}^j;..\tilde{\boldsymbol{A}}^N]$, likewise for $\mathcal{B}$ and Eq. (5.10) is rewritten as:

$$\mathcal{A} = \tilde{\mathcal{H}}\mathcal{B} + \tilde{\mathcal{J}}^{B0}\tilde{\mathcal{A}}^{0} \tag{5.12}$$

This matrix representation allows all cores and both fields to be manipulated at the same time.

During the introduction to the MM as detailed at the beginning of this section, a scattering or reflection operator $\mathcal{R}$ was described in addition to the basis transformation matrix $\mathcal{H}$. Coupling between the coefficients $\mathcal{A}$ and $\mathcal{B}$ occurs at the boundaries of the cores, where a regular field becomes either an outgoing field when it is reflected or a regular field inside a core when it is transmitted. The matrix $\mathcal{R}$ as derived from the boundary conditions, contains the details of this interaction. In matrix notation, this relationship is written as:

$$\begin{gathered}\tilde{\boldsymbol{B}}^l = \tilde{\boldsymbol{R}}^l \tilde{\boldsymbol{A}}^l \\ \tilde{\boldsymbol{R}}^l = \begin{bmatrix} \boldsymbol{R}^{EEl} & \boldsymbol{R}^{EKl} \\ \boldsymbol{R}^{KEl} & \boldsymbol{R}^{KKl} \end{bmatrix}\end{gathered} \tag{5.13}$$

where each matrix in $\tilde{\boldsymbol{R}}^l$ is a diagonal M x M matrix of corresponding reflection coefficients R_n^{VVl}. The derivation of these coefficients for circular boundaries is not included here but can be found in the following sources [29, 59]. When all cores are included, the matrix is rewritten as $\boldsymbol{\mathcal{R}}$ which is a block diagonal matrix of matrices $\tilde{\boldsymbol{R}}^l$ for each core. The field reflected at the jacket, which is a regular field inside the cladding, can be expressed similarly as reflected outgoing field incident on the jacket.

$$\tilde{\boldsymbol{A}}^0 = \tilde{\boldsymbol{R}}^0 \tilde{\boldsymbol{B}}^0 \tag{5.14}$$

In an analogous manner to Eq. (5.9), the outgoing field at the jacket is a combination of all the fields from each core.

$$\begin{gathered}\tilde{\boldsymbol{B}}^0 = \sum_{j=1}^{N} \tilde{\mathcal{J}}^{0j} \tilde{\boldsymbol{B}}^0 = \tilde{\mathcal{J}}^{0B} \boldsymbol{\mathcal{B}} \\ \mathcal{J}_{nm}^{0\ell} = J_{n-m}(k_\perp c_l) \exp(-i(n-m)\arg(\vec{c}_l))\end{gathered} \tag{5.15}$$

The $\boldsymbol{\mathcal{J}}^{0B}$ and $\boldsymbol{\mathcal{J}}^{B0}$ matrices are 2MN x 2M column and 2M x 2MN row matrices, respectively, that describe the conversion of the individual field in the local core coordinate systems to the field near the jacket in the global coordinate system.

It is now possible to reexamine the expression in Eq. (5.12) by eliminating the $\mathcal{A}$ coefficients using Eq. (5.14), Eq. (5.15), and Eq. (5.13). A simple homogenous system of equations results:

$$[\boldsymbol{I} - \mathcal{R}(\tilde{\mathcal{H}} - \tilde{\mathcal{J}}^{B0}\mathcal{R}^{0}\tilde{\mathcal{J}}^{0B})]\mathcal{B} \equiv \mathcal{M}\mathcal{B} = 0 \qquad (5.16)$$

This is also called the field identity or Rayleigh identity, shown here without external sources (ie. the right hand side is zero). Non-trivial solutions to Eq. (5.16) represent mode solutions to this multi-core system.

Implementation in Matlab

The implementation of this method as a Matlab program is rather straightforward since the Matlab language utilizes matrices and vectors and is well-suited for numerical rather than symbolic calculations. The Matlab MM program was organized into different Matlab function files for each matrix, $\mathcal{R}, \mathcal{H}, \mathcal{J}^{B0}, \mathcal{J}^{0B}$ and $\mathcal{R}^{0}$, in Eq. (5.16). These files require the index distribution, the expansion order, the size of the computation window, and the wavelength as inputs. An additional Matlab m-file was created to access the matrix function files and to perform calculations on the $\mathcal{M}$-matrix, which is necessary in order to determine the modes or to plot the modal fields.

The effective indices of the mode solutions are located at the minimum points of the complex determinant of the $\mathcal{M}$-matrix. These minimums can be found when log base 10 of the modulus of the determinant is plotted over a complex plane of values for the effective index. Alternatively, a scan for minimums can be made first on the real axis and then consequently on the imaginary axis; although more computationally efficient, this method is not as accurate. Additional information about appropriate minimum finders appears in the following citations [29, 63]. The field coefficients for a particular mode are found through a singular value decomposition or by determining the eigenvectors for the smallest eigenvalues when the $\mathcal{M}$ -matrix is evaluated with the corresponding mode index. At least one eigenvalue will be approximately equal to zero if the mode is valid and multiple eigenvalues that equal zero will exist if the mode is degenerate. The modal fields are then calculated using these coefficients and the global expansion of Eq. (5.4).

The implementation of the multipole method as a Matlab program was successful, arriving at accurate effective index solutions and mode fields as compared to those examples given in reference [59]. Examples of the field output for the Matlab program are given in Figure 5-5 and Figure 5-6 for two modes of a photonic crystal fiber with a single ring of air holes, wavelength of 1.45 μm, air hole separation or pitch of $\Lambda = 6.75$ μm, and air hole diameter $d = 5$ μm. The index of refraction of the fiber is $n = 1.45$ and the index of the air holes is 1. The number of terms in the multipole expansion was 11, therefore $m = 5$.

In this fiber, the air holes are arranged in a triangular or hexagonal lattice structure, also referred to as having C_{6v} symmetry in group theory, and the fundamental mode is therefore two-fold degenerate [64-67]. In Figure 5-5, the field components of one of the degenerate fundamental modes are shown. Notice that the nodal plane of the mode does not happen to fall along the obvious x- or y-axis. While the exact orientation of this nodal plane is not significant, the reason the field is equally distributed in the x- and y- components, rather than appearing x- or y-polarized, is a result of the mismatch between the orientation of the nodal plane and the components of the field. Figure 5-6 shows the components of the field for the first higher order mode. These plots are typical of PCFs of this type and are very similar in shape to the modes of a step-index fiber.

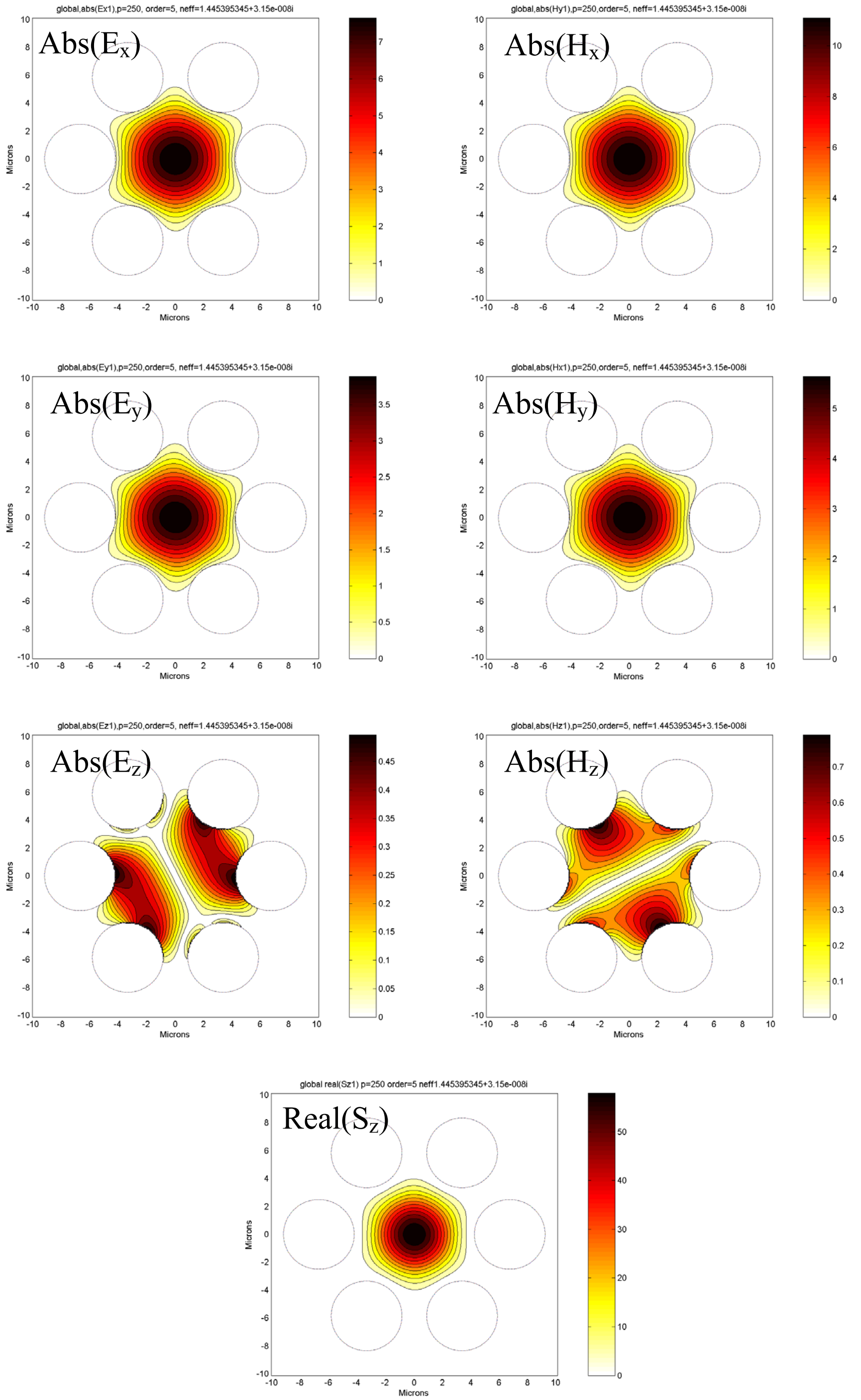

Figure 5-5. One of the degenerate fundamental modes of the PCF described in the text.

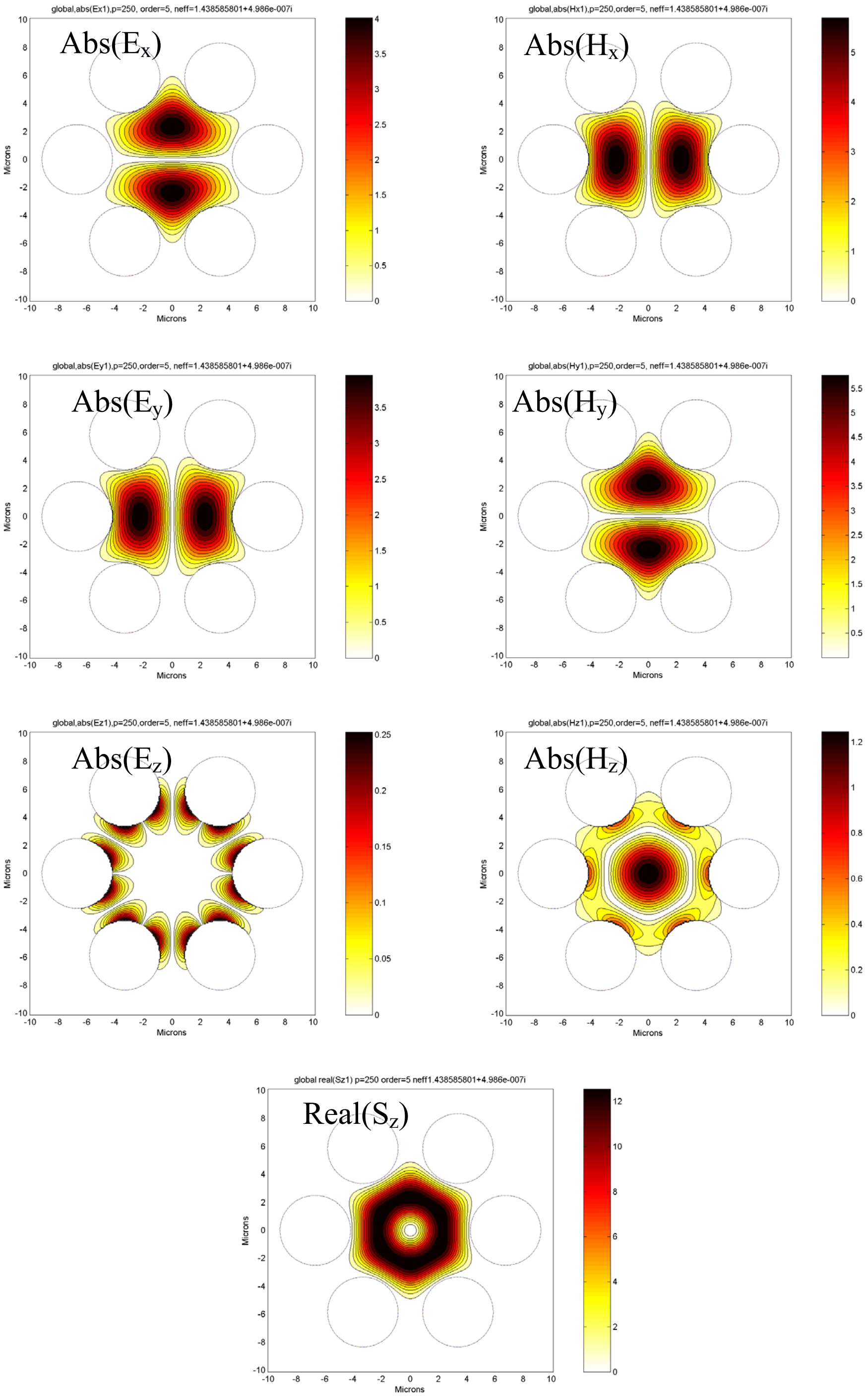

Figure 5-6. Modal fields for the first higher order mode of the PCF described in the text.

When using numerical simulations for research, it is extremely important to understand how the precision of the program output as well as the time duration of the calculation can be manipulated. Typically, these two factors exist in a trade-off; that is, given unlimited time, an extremely precise result can be obtained. For the multipole method calculations, the number of air holes or cores and the multipole expansion order determine the size of the $\mathcal{M}$-matrix and thus the computation time; however, these two parameters are also intimately tied to the reliability of the output. If the number of terms used in the multipole expansion is insufficient, the results and predicted behavior for the fiber are inaccurate and can appear non-physical. In addition, certain properties of PCFs do not change significantly with additional rings of air holes, while other properties, such as the loss, are extremely sensitive.

To reduce computation time, the simulated structure should include only the minimum number of air holes necessary. For example, if the actual PCF contains five rings of air holes around a single core, there will be 90 air holes included in the simulation. This number can be reduced by incorporating symmetries into the program [29, 63]. For a structure with six-fold symmetry, only one-sixth of these air holes would need to be included in the simulation, thus reducing the size of the $\mathcal{M}$-matrix. Furthermore, depending on the parameter being calculating, one or two rings of air holes may be sufficient. In general, the calculated loss is extremely sensitive to the number of air holes while parameters based on the value for the real part of the effective index (such as the dispersion or coupling length) tend to require only a single ring of air holes unless d/Λ is on the order of 0.5 [50, 51]. The number of rings of air holes needed can be easily verified by performing calculations first with a single ring and then adding more rings to verify convergence. A point will be reached where the extra computation required will not justify such a small change in the output value. In a practical situation, a minimum degree of precision can be estimated based on the use for the results of the calculation.

The optimum number of multipole terms to include in the expansion can also be determined through tests of convergence [63]. For example, the first calculation performed should include a smaller number of terms. As the number of terms is increased, the values for the real and imaginary part of the effective index should converge to a single value. The amount of change the index incurs with increasing orders will decrease and a point will be reached where increasing precision is not worth the increased computation time. The convergence of the real and imaginary part of the mode effective index is shown in Figure 5-7 for an example PCF.

An additional parameter for monitoring the accuracy of the MM program has been defined by Kuhlmey et al. [63]. This parameter is referred to as the W-parameter and is a measure of how closely the local and global (or Wijngaard) expressions for the field agree. The W-parameter is defined in Eq. (5.17) as

$$W = \frac{\int_{C_1} \left| E_z^{local}(\theta_1) - E_z^{Wijngaard}(\theta_1) \right| d\theta_1}{\int_{C_1} \left| E_z^{Wijngaard}(\theta_1) \right| d\theta_1} \tag{5.17}$$

where C_1 represents the boundary of core 1; therefore θ_1 is in the local coordinate system of core 1. The MM method is based on the forced consistency of these two expressions which will only be identical on a core boundary when all multipole orders are included. As the number of included multipole terms increases, W will decrease and the value for the effective index will stabilize [63]. The convergence of W is shown in Figure 5-8(a) for the same fiber as Figure 5-7. Additional insight can be gained by comparing the values for the z-component of the field on a core boundary as a function of that local coordinate system angle and as calculated by both the local and global expansions. This comparison is shown in Figure 5-9 (theta is in units of radians). The real part of the z-component of the electric field is plotted in Figure 5-9(a) when *m* = 2. The number of multipole terms is increased in Figure 5-9(b) to *m* = 7. Likewise, the imaginary part of the field is plotted in Figure 5-9(c) and Figure 5-9(d) for the same orders, respectively. Notice that the global and local expansions are nearly indiscernible when more terms are included. By plotting the differences $\left|\mathrm{Re}(E_z^{wijn} - E_z^{local})\right|$ and $\left|\mathrm{Im}(E_z^{wijn} - E_z^{local})\right|$, the agreement between these expressions can be assessed more closely. These values are plotted in Figure 5-8(b) for *m* = 2 and in Figure 5-8(c) for *m* = 7 and it is evident that the magnitude of the difference decreases for larger values of *m*. An analysis of this kind provides a detailed understanding of the precision of the program. Additional information about assessing the accuracy and precision of the numerically implemented MM are given in [29, 63]. In general, as the size of the air core increases and as the pitch increases, more terms must be included in the expansion.

Other sources of inaccuracy or error are inevitable when performing numerical calculations. Comparisons with already established values may assist in determining if these problems exist. When implementation of the MM Matlab program was complete, several comparisons with published results were made in order to establish the accuracy of the program. In addition, the size of the computation space chosen or the step size can also be sources of error. Convergence tests can again be used to establish a minimize number of points for an accurate computation. Above all, results from numerical simulations should be constantly scrutinized for physical plausibility.

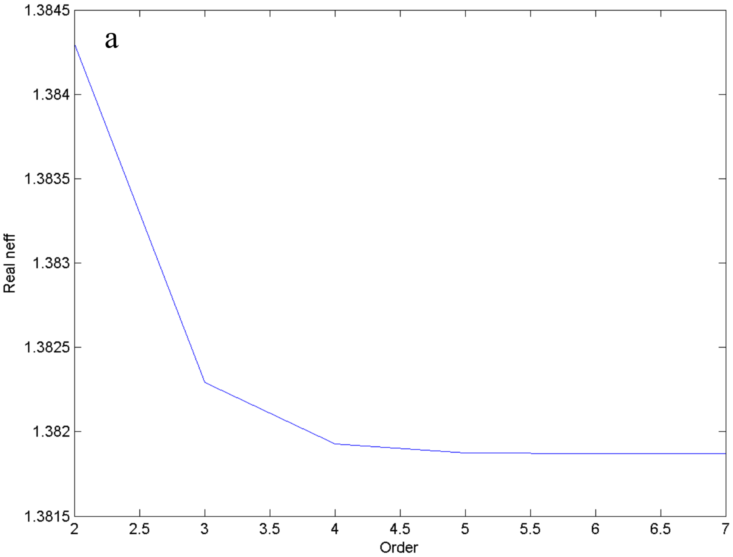

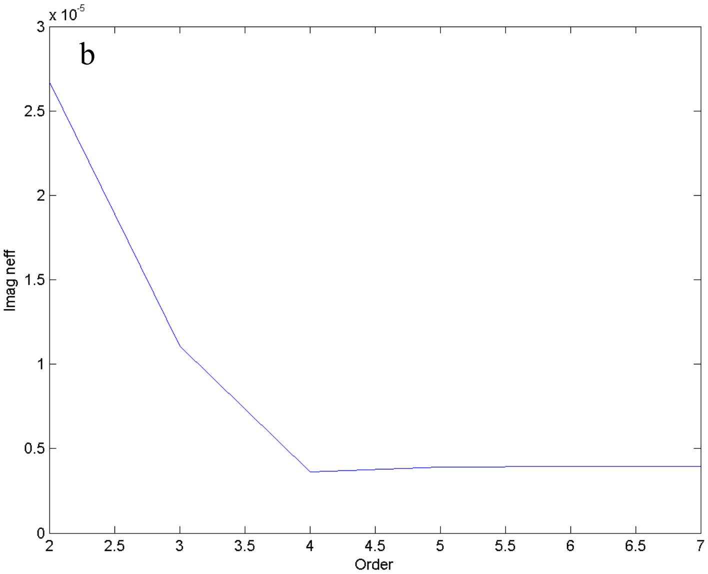

Figure 5-7. The convergence of the real a) and imaginary b) part of the mode effective index for a PCF with d/Λ = 0.90, Λ = 0.75 μm, and λ = 0.60 μm.

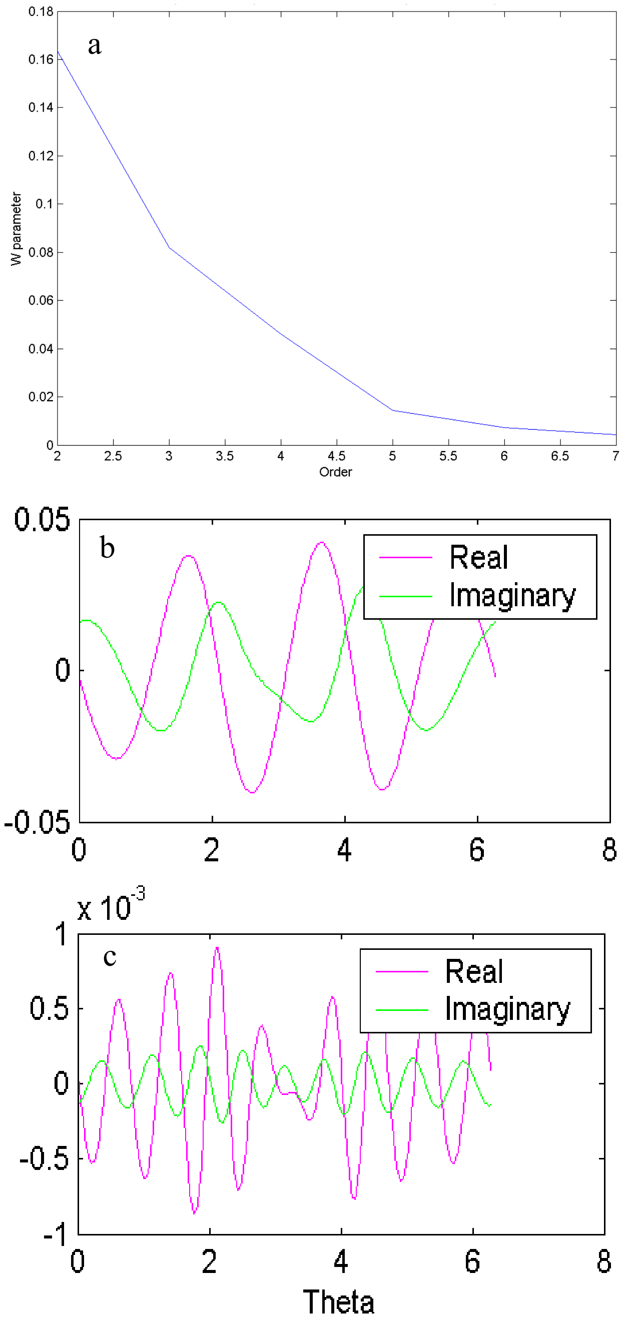

Figure 5-8. The convergence of the W-parameter is shown in a). In b) and c) the difference between the z-component of the electric field as calculated by global and local expansions is shown for two different orders. *m* = 2 in b) and *m* = 7 in c)

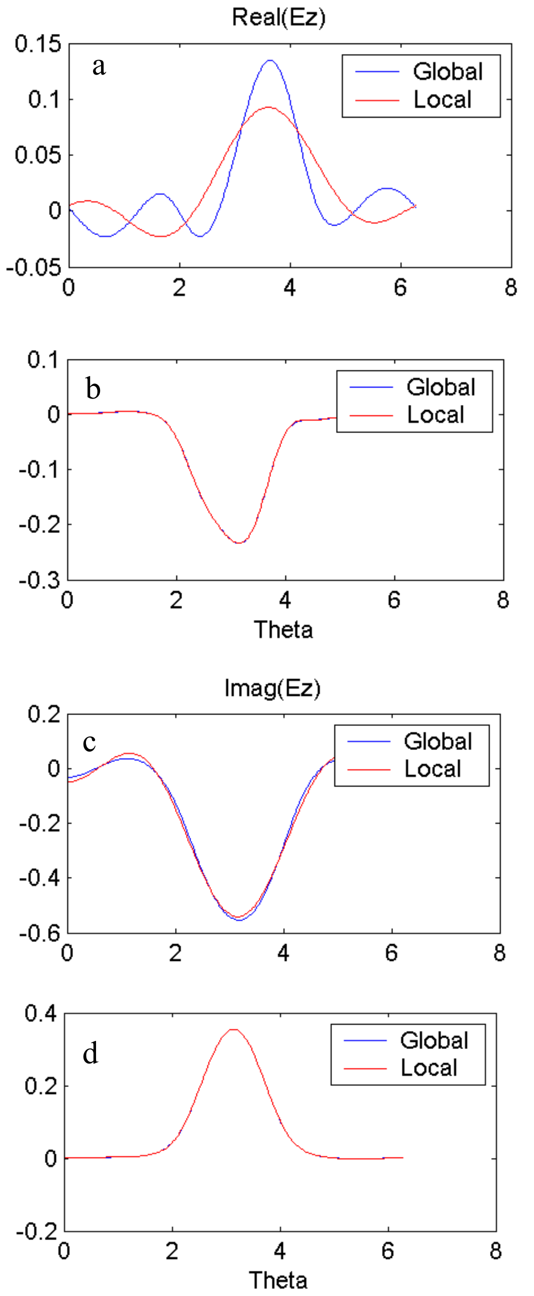

Figure 5-9. The real a) and b) and imaginary c) and d) parts of the z-component of the electric field are plotted versus the local angle as calculated using the global and local expansions. *m* = 2 in a) and c) and *m* = 7 in b) and d).

Utlizing the CUDOS and Matlab MM programs

A Fortran based program using the multipole method has also been distributed by the Centre for Ultra-high bandwidth Devices for Optical Systems (CUDOS) at the University of Sydney [3]. The CUDOS MOF Utilities Software is freely available on the internet and was also used by the author. The CUDOS software uses text files as inputs, which are executed through a command window. The outputs are text files of the mode indices as well as files specific to Winfield, the CUDOS field plotting program. The program itself and more information on the use of the CUDOS MOF Utilities Software can be found at the following reference [3].

The CUDOS program is a more user friendly and a faster implementation of the MM than the author's Matlab version. The speed advantage of the CUDOS program is most likely due to the use of the Fortran programming language and a faster minimum finding algorithm. The MM Matlab program was rather slow for computing the mode indices because the method for finding the minimums in the $\mathcal{M}$-matrix was not optimized. Moreover, the CUDOS program takes advantage of the symmetry in some fibers through the application of group theory. In these cases, a matrix of only a fraction of the original size is computed. This tool was not yet incorporated into the MM Matlab program since most calculations were performed on structures without symmetry. Besides increased speed and the use of symmetry to further reduce computation time, the theory and understanding of these two programs are identical.

The CUDOS program has a few additional advantages when certain parameters are being calculated. The CUDOS Software includes an additional algorithm for quickly calculating the dispersion across a large range of wavelengths; many points can be calculated in a fraction of the time it would take to search for the modes individually. Due to the use of a two-dimensional minimizing algorithm, the CUDOS program is also more accurate for high loss fibers.

Because the CUDOS MOF Utilities Software cannot automatically output the data for the calculated modal fields, the two programs are used in unison to take advantage of the strengths of each implementation. Matlab was used to generate the structure files and the parameter files (both are text files) that are the required input for the CUDOS program in such a manner that a large number of structures could be solved for sequentially. The CUDOS prompt window was used to execute the files and then Matlab opened and interpreted the output files. Specifically, when solving for the modes of a particular fiber, the CUDOS output that is accessed by Matlab is a text file containing the complex indices for the modes along with the computational precision. Matlab can then calculate the fields directly from the mode indices or it can read another CUDOS text file that includes the $\mathcal{B}$ and $\mathcal{A}$ coefficients for the electric and magnetic fields. The modal fields are then calculated using the global expansion and these coefficients.

A few noteworthy problems have arisen through use the CUDOS program itself and through the combined use of the two programs. First of all, it was discovered that the CUDOS program produces false minimums when solving multi-core step-index fibers when symmetries are considered. Calculations without symmetries, however, produced accurate results for these types of fibers. When using the CUDOS program, it is also difficult to accurately detect closely spaced modes for non-symmetric structures. Several test runs of increasingly small windows must be performed in order to estimate the index value before an accurate result can be found.

In addition, the dispersion calculations can be compromised when modes are non-degenerate because the program will arbitrarily follow one or the other mode as the wavelength is changed. One limitation of the multipole method in general is that it does not converge for single core step-index fibers. Due to the foundation of the method on a system of interacting scatterers, one core is not a viable situation.

A general problem of mode non-orthogonality has also manifested itself in the MM programs. It appears that at shorter wavelengths, when modes are well-confined, the degree of non-orthogonality is extremely small. The use of both programs in sequence can exacerbate the non-orthogonality of the modes due a “mismatch” between the mode indices determined from the CUDOS program and the minimums of the MM Matlab $\mathcal{M}$ -matrix. Due to slight differences in the program languages and the implementation, the mode indices calculated by the CUDOS program are not the exact same minimums for the MM Matlab program. This problem can be avoided by using directly the CUDOS output for the $\mathcal{B}$ and $\mathcal{A}$ coefficients of the field. The mode non-orthogonality is especially compromising to results when these modes are used in a normal mode expansion as described in Chapter 3. An additional error is then present in calculations of parameters such as the power which use the mode expansion as an expression for the field; however, if the magnitude of this error is guaranteed to be much smaller than the values being calculated, it is not seen as a problem. Additional research must be done in order to understand the exact source of this error and to understand the regimes when it can be ignored. The integrity of the results presented in this dissertation is not compromised by this inaccuracy.

Chapter 6

COUPLING IN PHOTONIC CRYSTAL FIBERS

Introduction

In this chapter, the theories for predicting coupling behavior as discussed in Chapter 3 will be applied to multi-core PCFs. First, a scalar approximate model and a vector model based on these theories will be compared. A scalar method that takes advantage of the effective index model for PCFs as described in Chapter 4 and coupled mode theory (CMT) appears to be a simple way for approximating the behavior of a two-core PCF. A more accurate method uses the normal mode expansion and requires the calculation of the two-core PCF modes using the Multipole Method explained in Chapter 5. In this chapter, these two methods are compared and then the basic coupling properties of various types of two-core PCFs are described as a function of the fiber parameters. .

Comparison of vector and scalar models

As an assessment of the accuracy of the scalar effective index model for predicting the coupling in two-core PCFs, the coupling lengths for a range of fiber structures are calculated using a vectoral model and then compared to the results of a scalar model. For the scalar method calculations, CMT is applied to a two-core PCF using the effective index model. Recalling from Chapter 3 that CMT is based on the mode solutions for the individual independent waveguides, the mode solutions for a two-core PCF could then be expressed as the linear superposition of the modes of a single core PCF. This concept is illustrated in Figure 6-1 for a two-core PCF. The mode fields for even a single core photonic crystal fiber, however, are fairly complicated and the calculation of the mode overlap from these fields would require incorporation of the vector nature of the fields. In order to create a completely scalar model, each core in the two-core PCF is replaced by an equivalent step index fiber using the effective index model as shown in Figure 6-2. CMT is then applied to this two-core step index fiber in the same manner as described in Chapter 3.

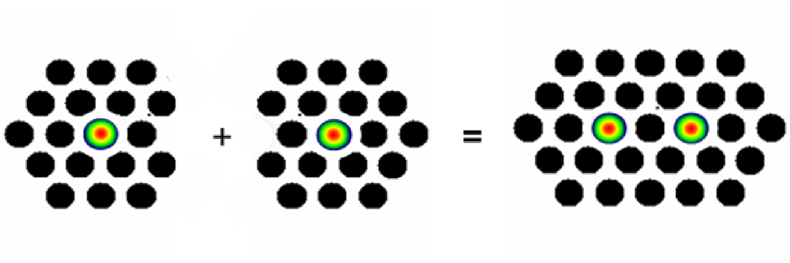

Figure 6-1. CMT interpretation of a two-core PCF as the sum of two single core PCFs

For a step-index fiber, the mode effective indices and the modal fields are fairly quick to compute by solving the scalar wave equation as described in Chapter 2. Only the circularly symmetric fundamental mode is considered in this case which further simplifies the calculations. The coupling constant, K_{ab}, is computed from these fields according to Eq. (3.8), as an integral over the area of core *b* (the right core) and the coupling length is determined from Eq. (3.13). As mentioned in Chapter 3, a scalar and an empirical model have been proposed for calculating the index of the fundamental space filling mode, n_{fsm}, or the cladding index in the effective index model. Both methods are used here in computations of the single core modes, and then K_{ab}. Results for the coupling length using each method for determining n_{fsm} are compared to the vectoral results from the multipole method simulations. The coupling length calculated from the mode overlap of the TM fundamental mode of an

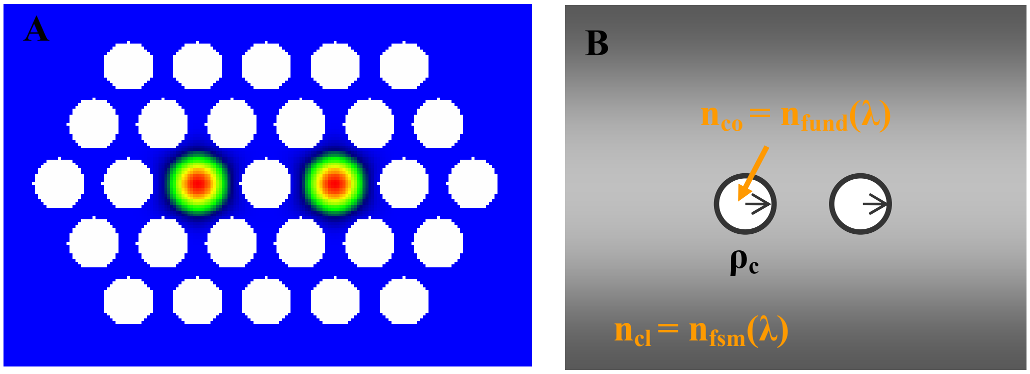

Figure 6-2. Application of the effective index model to a PCF with two cores. Image A is of a two core photonic crystal fiber, while B is the equivalent two-core SIF.

equivalent SIF is compared with the x-polarization coupling length. Likewise, the coupling length calculated from the TE mode is compared to the y-polarization coupling length.

The fully vectoral model uses the numerical simulation program based on the multipole method described in Chapter 5 to calculate the modes of the complete two-core system. The modes of a two-core PCF closely resemble those of a two-core step-index fiber and the real part of the x- and y- components of the electric field are shown in Figure 6-3. The two-fold degenerate fundamental mode of a single core PCF is also shown and can be viewed as an x-polarized and a y-polarized mode. A mode is considered to be y-polarized when the y-component of the electric field is much larger than the x-component, and vice versa for an x-polarized mode. These modes can be categorized according to polarization and symmetry as is typical of a two-core fiber. A more clear comparison of the symmetric and antisymmetric modes for a single polarization is given in Figure 6-4. After the modes are solved, the coupling length can be determined from the power using the normal mode expansion as explained in Chapter 3 using Eq. (3.6).

Figure 6-5 compares the beat length as calculated from scalar and vector models as a function of pitch for photonic crystal fibers of five different relative air hole sizes. In plots A and B, the scalar approximation for n_{fsm} is used [39], while in plots C and D, the empirical method of Saitoh and Koshiba is utilized [41]; the solid lines are the results from the multipole method. Figure 6-5 shows an overall tendency of the effective index model to underestimate the coupling length, based on the assumption that the vector model should produce more accurate results. It is interesting to note that in plots A and B, the general relationship between the coupling length and the pitch is the same regardless of the model; however, the values for the

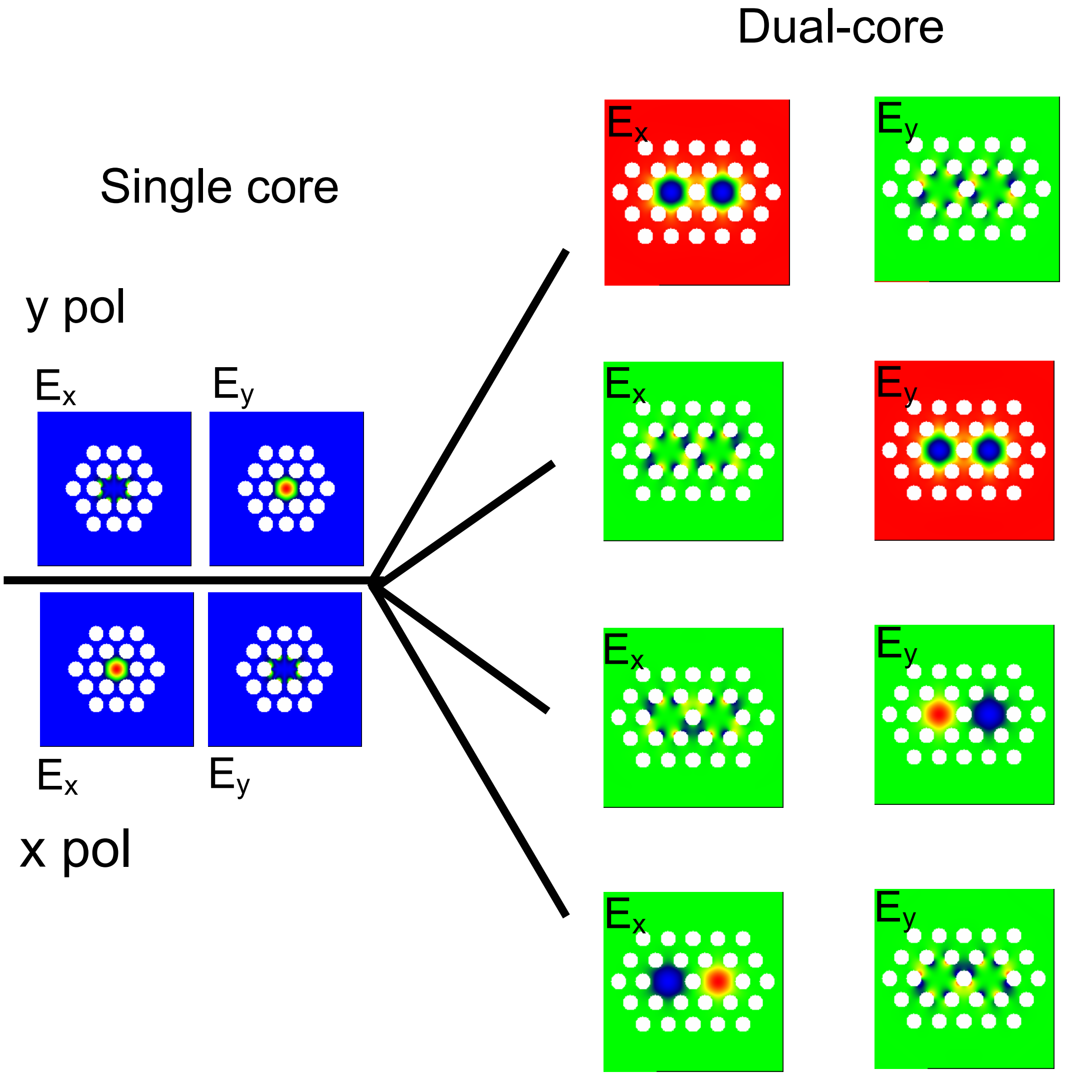

Figure 6-3. The modes of a single core PCF and a two-core PCF. For the two-core fiber, the amplitudes of the field components are shown.

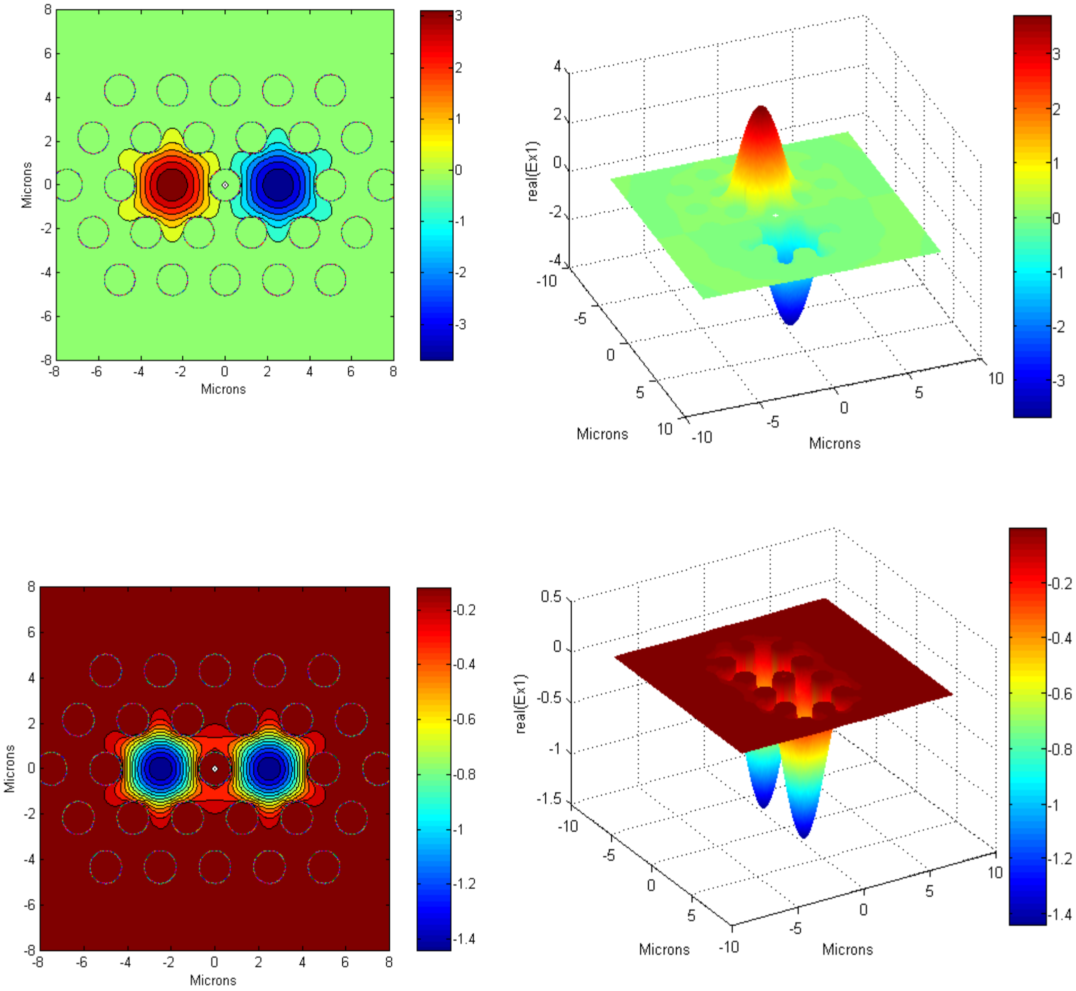

Figure 6-4. A closer examination of the even and odd modes of a single polarization for a two-core PCF.

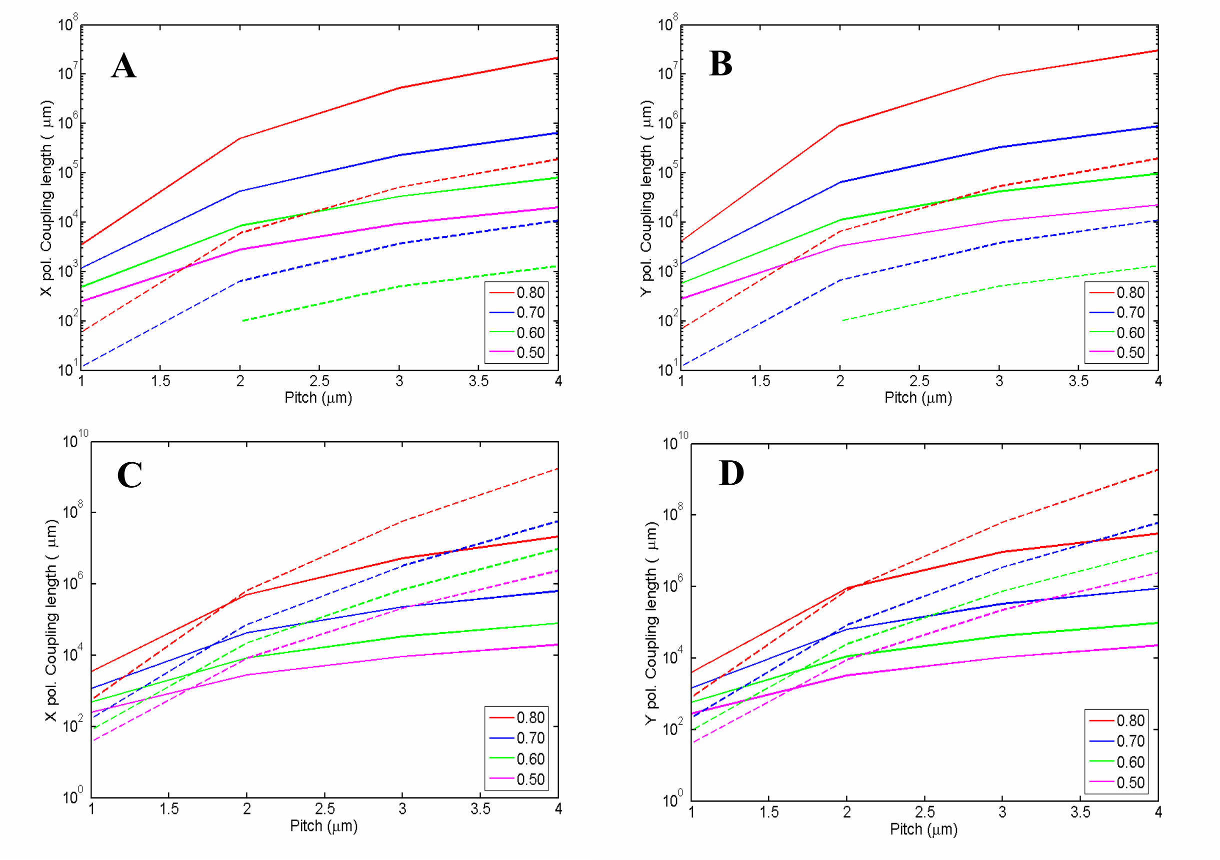

Figure 6-5. Comparison of different methods for obtaining the x- and y-polarization coupling lengths of two core PCF fibers. The dashed lines represent results using the effective index model while the solid lines are values calculated from a vector method. In plots A and B, a scalar method is used for determining n_{fsm}, while in plots C and D n_{fsm} is found using an empirical method. Each color indicates a different ratio of d/Λ. $\Lambda = 0.80$. Data missing from plots A and B indicate regions where the method is no longer valid.

coupling length appear to be low by approximately two orders of magnitude. In plots C and D, the overall magnitudes of the predicted coupling lengths tend to agree between the two models for low pitch values, but the relationship between the coupling length and the pitch as derived from each model is distinctly different.

A misrepresentative definition of ρ_c may have led to some discrepancy between the scalar and vector models. Performing the simulations again with an alternative definition of the core radius, $\rho_c = 0.64\Lambda$ (see Chapter 3), produced very little change in the plots. The relationships were identical but the beat length values shifted only slightly higher. An additional definition of ρ_c that is dependent on the air hole size may be more accurate. The plots were again reproduced for $\rho_c = F\Lambda$, where F is the filling fraction for a triangular lattice:

$$F = \frac{\pi}{2\sqrt{3}}\left(\frac{d}{\Lambda}\right)^2 \tag{6.1}$$

and d is the diameter of the air holes [39]. This value for ρ_c changed the relationships and values in Figure 6-5 in a slight but noticeable manner, yet did not improve the comparison between the scalar and vector models.

Comparing plots A and B with C and D demonstrates a lack of agreement between the scalar and empirical models used for the calculation of n_{fsm}. The empirical model is assumed to be more accurate than the scalar model because it requires fewer approximations and has been shown to produce very accurate results when compared to a vector method for calculating n_{fsm}; however, the relationship between the coupling length and the pitch predicted by the scalar model for n_{fsm} appears to match more closely with the relationship found using the multipole method.

A recent paper performs the same type of comparison, however, using an improved effective index model as the scalar model and the finite element method as the vector model [68]. The development of the improved effective index model (IEIM) [44] was motivated by the problems noticed here such as the lack of a standard definition for the core radius in the PCF equivalent SIF. In IEIM the radius is defined as a function of the pitch and the relative air hole size and is empirically obtained. Yu, Liu et al. demonstrate success in predicting the coupling length of two-core PCFs using this model, as verified using the finite element method [68].

Coupling properties of two-core PCFs

The coupling properties of a two waveguide system are determined by the overlap of the modes of the two individual cores and are therefore extremely sensitive to changes in the mode field area and the core separation. In a two-core SIF, the coupling length is dependent on the core size and separation relative to the wavelength (see Chapter 3), given that the core and cladding materials do not change. For a two-core PCF, the air hole arrangement that makes up the cladding plays a critical role in determining the coupling properties of the fiber. The vector model discussed in the previous section will now be used to describe how the coupling length of a two-core triangular lattice PCF depends on the air hole size and the pitch.

As explained in Chapter 4, for a particular wavelength, increasing the size of the air holes in a PCF will result in a larger index contrast between the core and the cladding and therefore a well-confined mode. Figure 6-6 demonstrates this trend; for a particular value for the pitch, increasing the air hole size decreases the mode effective area. When the mode field area is smaller, the perturbation experienced by the second core will be reduced and the coupling length will increase. Although increasing the pitch increases the mode area, it also increases the separation between the cores. The overall effect of increasing the air hole separation, for the same relative air hole size, is to increase the coupling length. Figure 6-7 demonstrates the relationship between the x- and y- polarization coupling length and both the air hole separation and the air hole size for a particular wavelength. The coupling length for a y-polarized input is always longer in the case that the orientation of the two cores is along the x-axis. In summary, two cores in a PCF will be weakly coupled if d/Λ and Λ are both large.

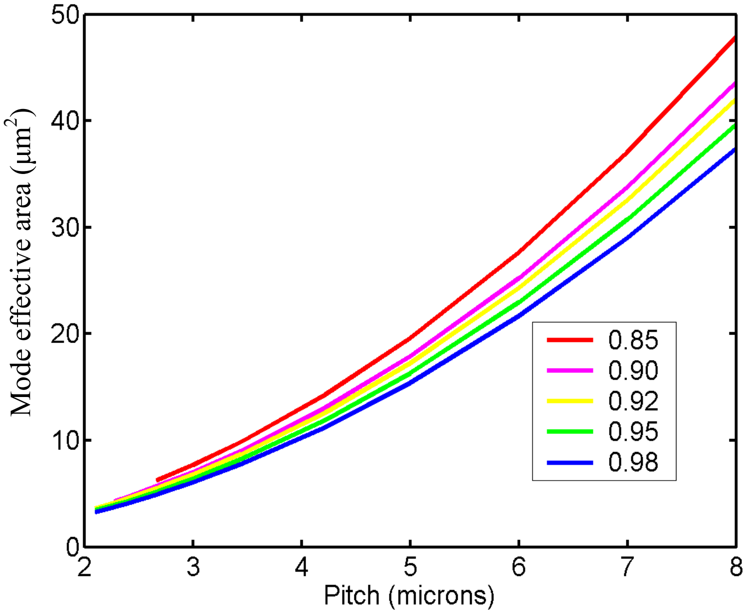

Figure 6-6. The mode effective area is plotted versus the pitch for several different relative air hole sizes. $\lambda = 1.55$ μm.

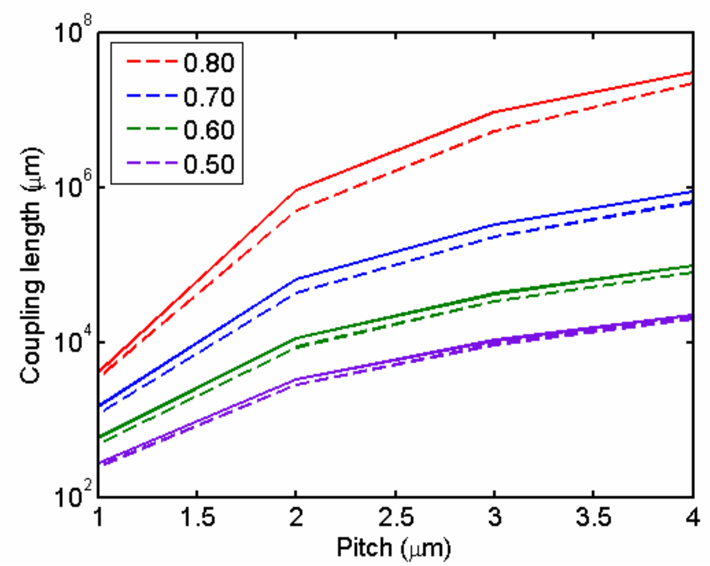

Figure 6-7. The coupling length as a function of the pitch for four values of the relative air hole size. The solid lines indicate the coupling length for a y-polarized input while the dashed represent the x-polarization. The wavelength is 0.80 μm

It is sometimes more convenient to view the relationship in Figure 6-7 as a function of the normalized wavelength. Figure 6-8 displays the coupling length for an x-polarized input as a function of the wavelength divided by the pitch; material dispersion is ignored. From this plot it is evident again that the coupling length increases as the size of the air holes increases. In addition, the coupling length will decrease as the wavelength increases for a particular core separation. As the wavelength increases, the mode will become larger and leak into the neighboring core, increasing the strength of the coupling.

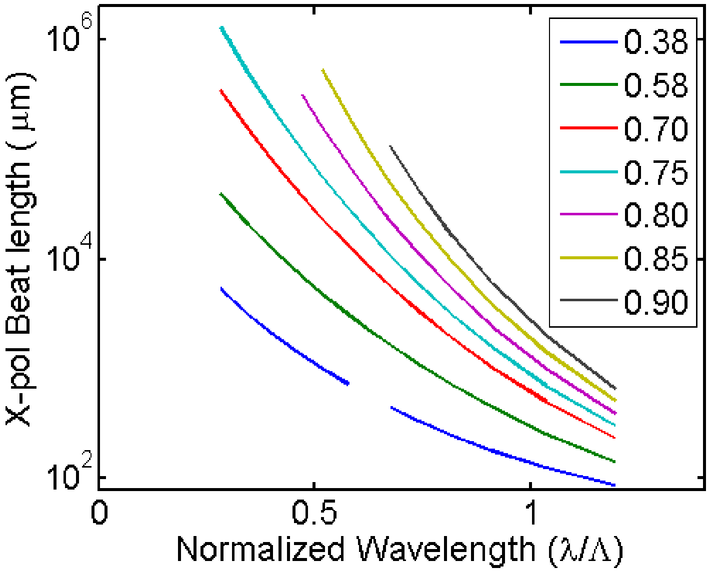

Figure 6-8. Coupling length for an x-polarized input as a function of the normalized wavelength for several different values of the relative air hole size, d/Λ.

In the two-core PCFs examined thus far, the air holes in the cladding are arranged such that an air hole is placed between the two cores, see Figure 6-2. An alternative arrangement appears in Figure 6-9, and has been labeled by some groups as a Type 1 two-core PCF [69]. The coupling lengths for these two types are compared for a particular air hole size in Figure 6-10(a). The coupling length in Type 2 fibers is longer because the placement of the air hole directly between the two cores reduces the rate at which power leaks from one core to the other. In Type 1 fibers, the lack of an air hole between the cores causes an increase in the coupling strength. In Figure 6-10(b), the coupling length for Type 1 fibers is plotted versus the pitch for four different air hole sizes. The same trends are observed in both types of fibers. The

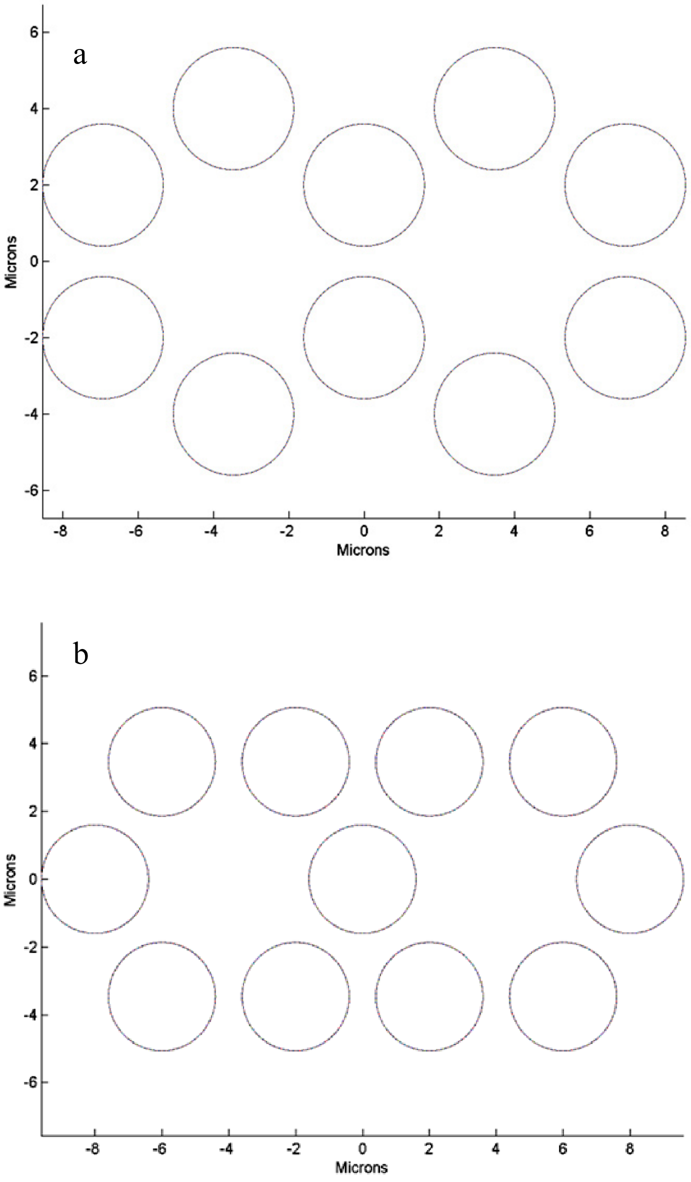

Figure 6-9. Type 1 (a) and Type 2 (b) two-core PCFs.

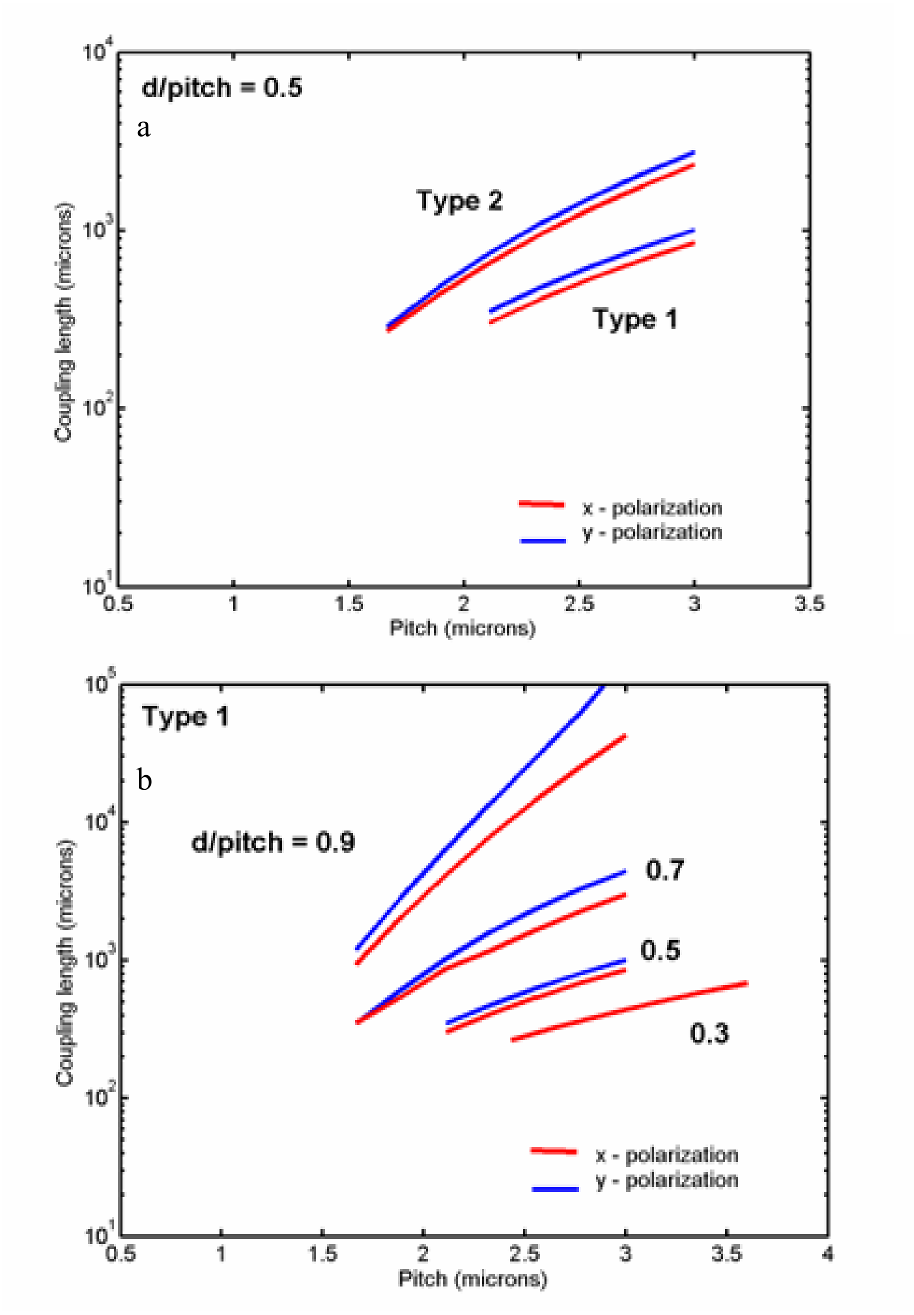

Figure 6-10. The coupling length for Type 1 and Type 2 two-core PCFs are compared for d/Λ = 0.5 (a) and the coupling length as a function of the pitch is shown for Type 1 fibers in (b) for four different values of the relative air hole size.

plots in Figure 6-10 can be compared to Figure 4 and Figure 5 of Reference [69]. The results of this group were duplicated as an additional check for the accuracy of the Matlab multipole program and the normal mode expansion method implemented to compute the coupling length. The finite element method was used to generate the data in this reference.

In summary, when short coupling lengths are desired, the best design would be a Type 1 arrangement of a two-core PCF with small, closely spaced air holes. Because of the motivation to produce smaller couplers and splitters, short coupling lengths are necessary for these types of applications. For applications such as endoscopes, optical interconnects, and sensors, long coupling lengths are necessary in order to prevent the exchange of information between the cores which would degrade the performance of these types of devices. In this latter case, Type 2 fibers with large air holes and large air hole spacing would be preferred.

Calculations of the coupling length use the real part of the effective index of the four modes of the fiber and are fairly sensitive to the precision of these values. If the index is not precise enough, non-physical behavior is predicted. Both the expansion order and the number of rings of air holes included in the multipole method simulation can affect the results. The optimum situation for each two-core PCF depends on both the air hole size and separation. See Chapter 5 for the details of the convergence analysis. In general, PCFs with large air holes require a larger number of terms in the multipole expansion; in addition, increasing the pitch for a particular air hole size also requires the inclusion of more terms in order to obtain accurate results. In Figure 6-11, the coupling length is plotted versus the pitch for a Type 2 two-core PCF with $d/\Lambda = 0.95$ for simulations of order $m = 6, 7, 8, 9$, and 12. Notice that as the order increases, the coupling length converges to a line and the asymptotic behavior

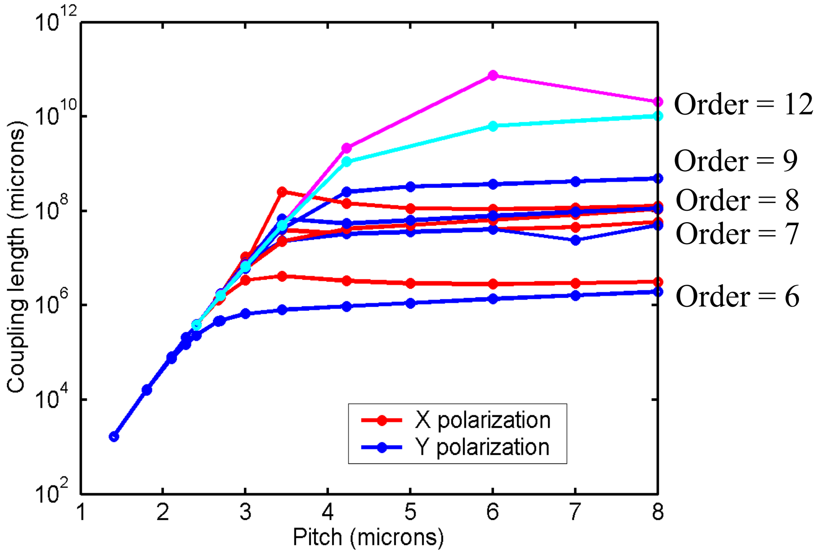

Figure 6-11. The coupling length is plotted versus the pitch for simulations including an increasing number of terms in the multipole expansion.

begins at larger and larger values for the pitch. It is evident from the trends in Figure 6-11 that the calculated values for the coupling length cannot be trusted when the pitch is greater than 5 μm, even when *m* = 12. However, if the pitch is only 2 μm, only 6 orders need to be included for accurate results. These calculations were also performed on a PCF with a single ring of air holes. Additional air holes do not significantly change the results in Figure 6-11 or the predicted behavior of other large air hole PCFs; however, a second ring was necessary when the air hole of sizes were equal to or smaller than d/Λ = 0.50.

A third type of core arrangement to be considered for a multi-core PCF is shown in Figure 6-12. The advantage of studying these types of cores is that they are readily fabricated and would require no new technology—the image in Figure 6-12 is merely a section of the cladding of a typical photonic crystal fiber [70]. Solutions for the modes of these cores are shown in Figure 6-13 through Figure 6-16 for a PCF with

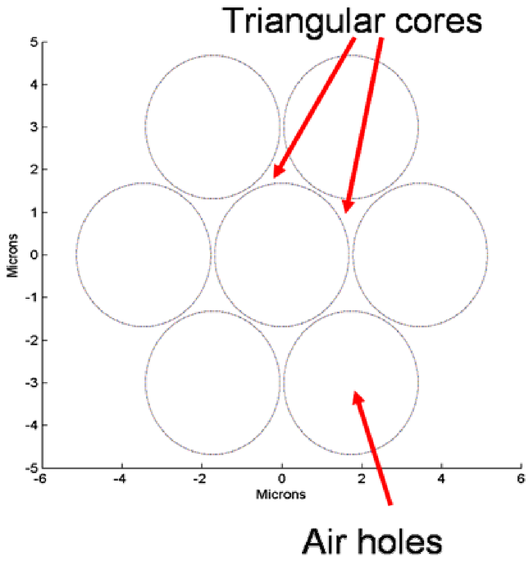

Figure 6-12. Illustrations of the triangular cores in PCFs.

d/Λ~0.98, Λ = 2.33 μm, and λ = 632 nm. The dimensions for this example were chosen based on an essentially single-moded core with the minimum possible bridge width between the air holes, 50nm, which is the estimated manufacturing limit. Because the modes are not well-confined, the coupling lengths are very short, predicted to be 860 μm for one polarization and 3900 μm for a second polarization. The bridge between the cores appears to strengthen the coupling in a similar manner to the Type 1 two-core PCF. The coupling length can be made longer by increasing the pitch and the air hole size. In Figure 6-17, the coupling length is shown to increase

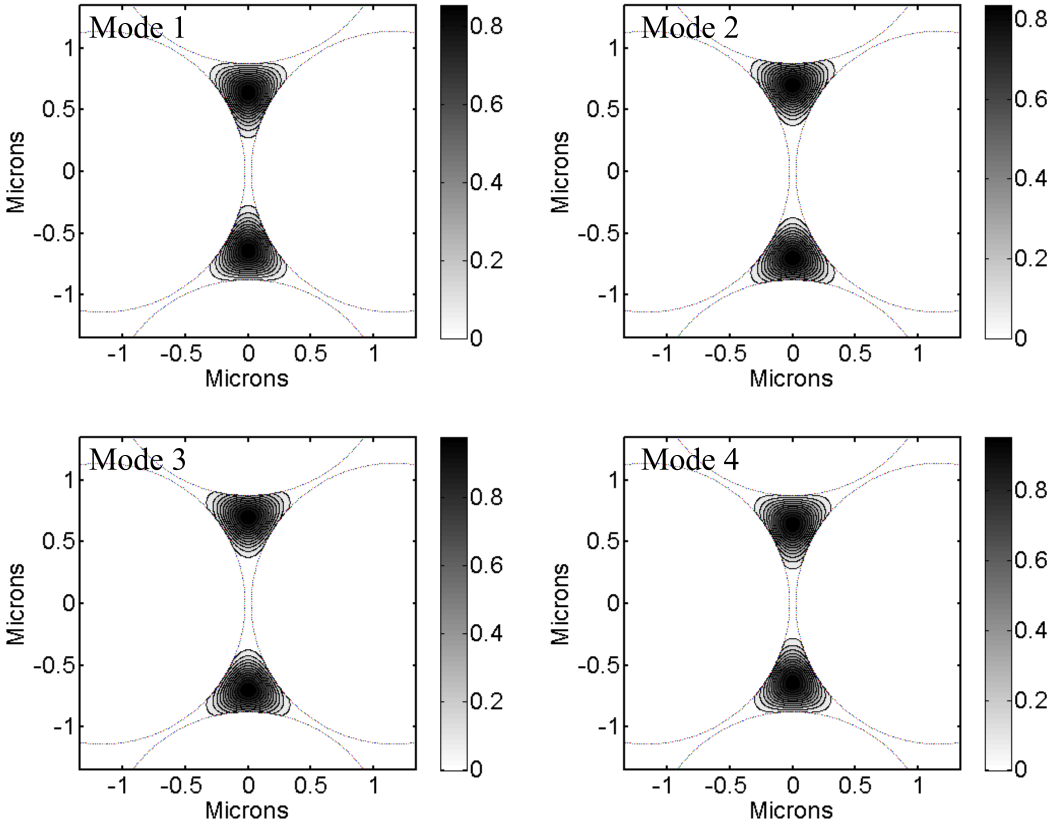

Figure 6-13. Modes of triangular core PCFs. Real(S_z)

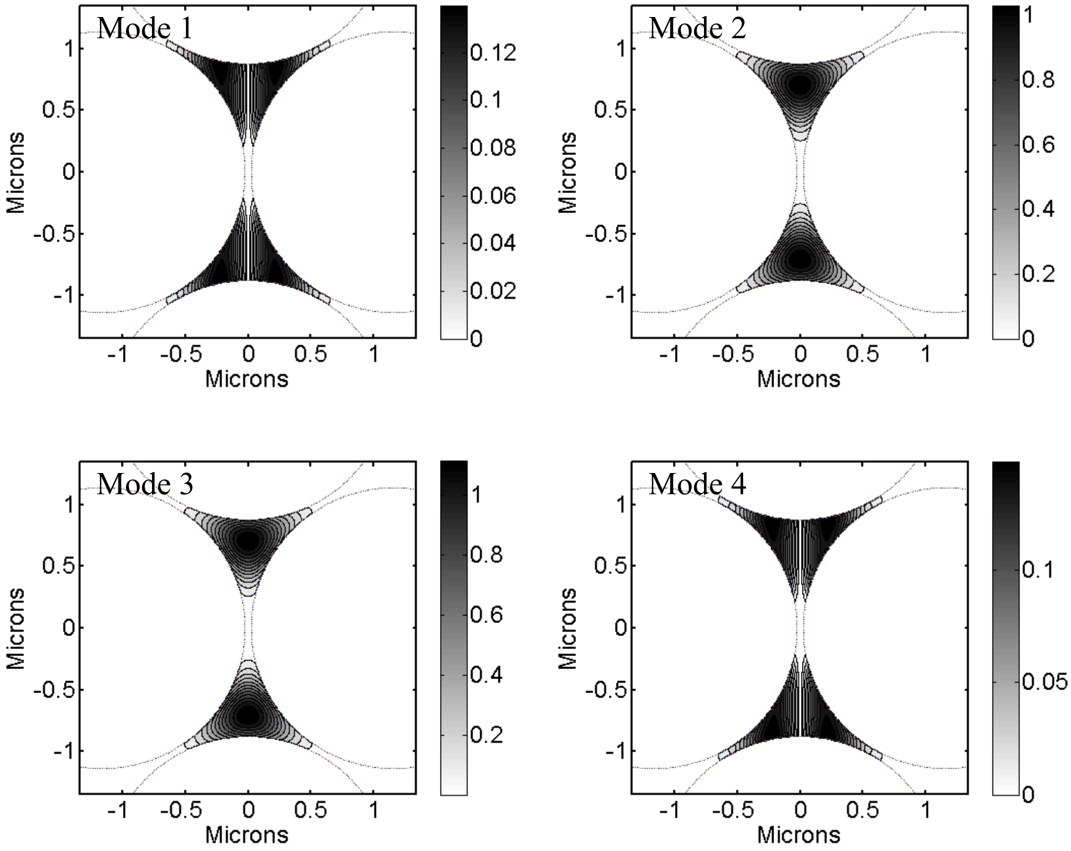

Figure 6-14. Modes of triangular core PCFs. Abs(E_x)

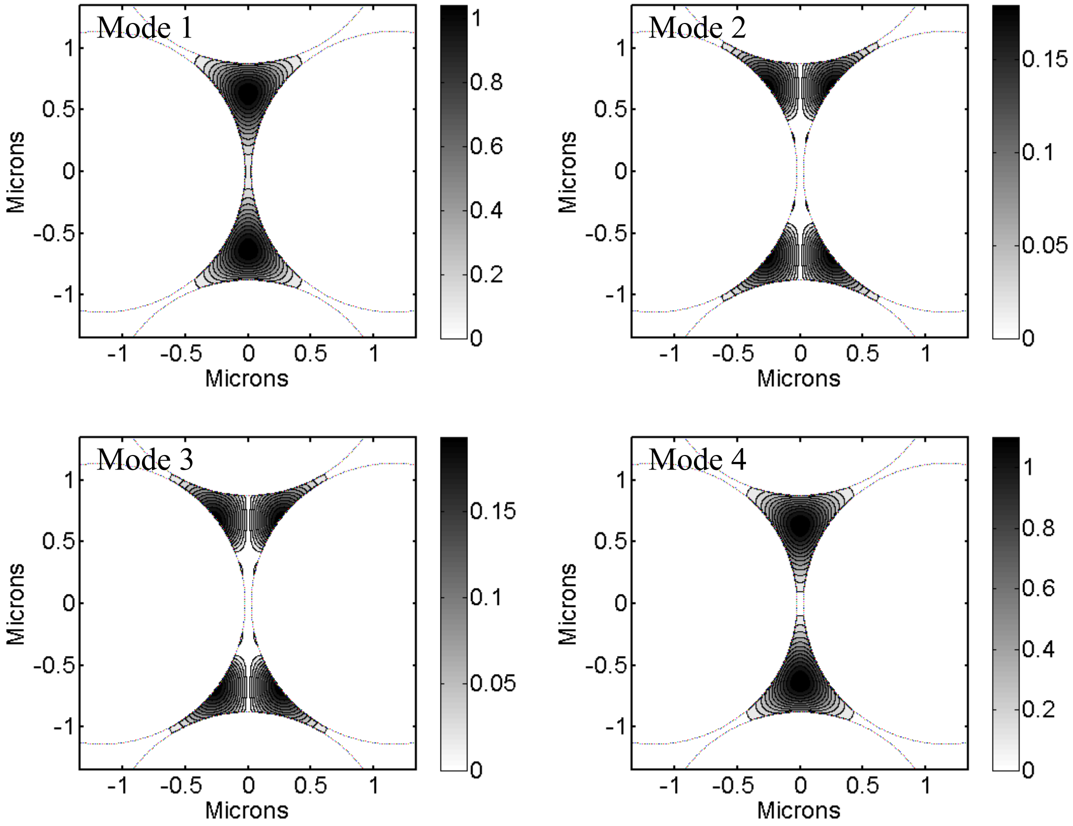

Figure 6-15. Modes of triangular core PCFs. Abs(E_y)

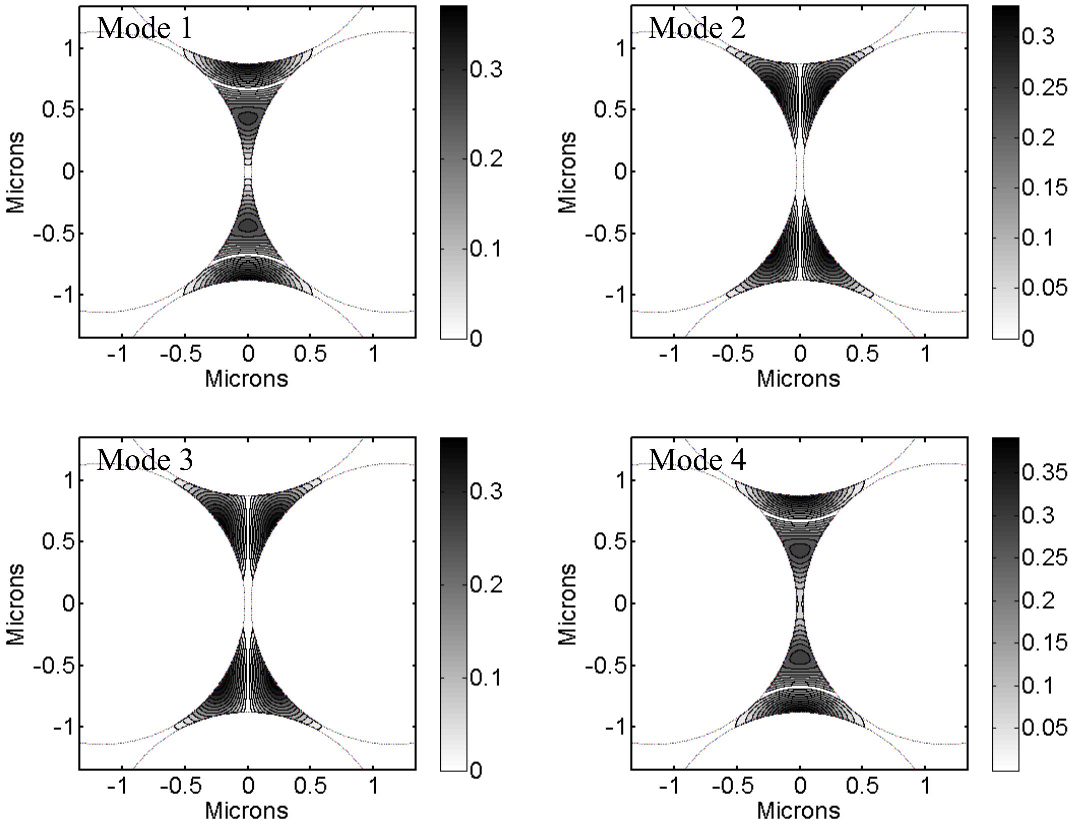

Figure 6-16. Modes of a triangular core PCFs. Abs(E_z)

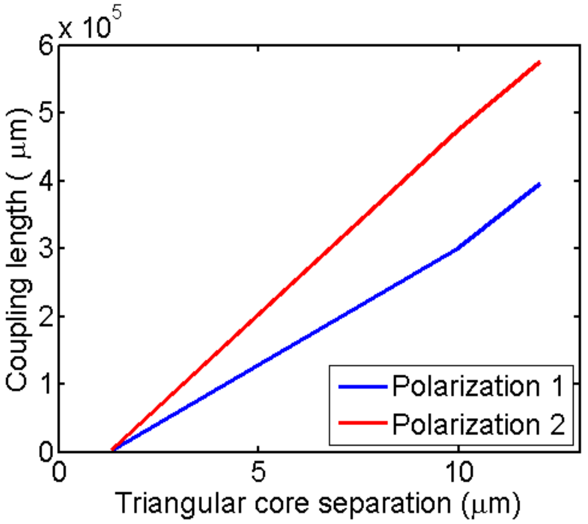

Figure 6-17. The coupling length is plotted versus the triangular cores separation

with the pitch when the air hole size is also increased in a manner to maintain the 50 nm size bridge.

These triangular cores were difficult and time consuming to calculate because a large number of orders in the multipole expansion are necessary for accurate results (twenty multipole orders are included in the mode calculations in Figure 6-13, Figure 6-14, Figure 6-15, and Figure 6-16), most likely because the area where the mode is propagating is much smaller than for the other PCFs studied. Overall, the coupling lengths of triangular core multi-core fibers appear to be impractically short for applications requiring weak coupling, such as endoscopes. In order to reduce coupling, the air hole size would need to be increased to a point where Type 2 two-core PCFs would provide tighter core packing and a longer coupling length. However, these types of cores tend to have a large splitting between the coupling lengths of the different polarizations due to the triangular shape of the core. It is possible this type of multi-core fiber could be beneficial for applications where phase matching or a highly polarization dependent dispersion are needed.

Conclusion

The potential application of multi-core PCFs in flexible endoscopes requires a thorough study of the coupling behavior of different types of multi-core PCFs. The coupling properties of two-core PCFs depend on the air hole size, the air hole separation, and the wavelength. The arrangement of air holes around the two cores also influences the coupling length. From the results presented in this chapter, it is possible to develop a proposal for a PCF endoscope using a multi-core PCF with a long coupling length. A detailed description of a potential design appears in Appendix A.

Chapter 7

THE EFFECTS OF RANDOMLY OCCURRING NONUNIFORMITIES ON PROPAGATION IN PHOTONIC CRYSTAL FIBERS

Introduction

Photonic crystal fibers (PCFs) have received significant attention from the scientific community due to their unique propagation characteristics [26, 39]. The use of PCFs for both system and device level applications sometimes requires novel air hole arrangements. Because of the cost and effort necessary for the fabrication of PCFs, precise numerical simulations are essential to guide the design process. A variety of numerical modeling methods are currently available that accurately calculate PCF properties; however, it is fastest and easiest to simulate perfect structures that have precisely located, exactly circular, air holes. Random variations in the photonic crystal lattice are inherent to the fabrication of PCFs and complicate the validity of predictions based on perfect fibers since fiber parameters can only be guaranteed with limited precision. Figure 7-1 illustrates how different the simulated, ideal fiber can be from the actual, fabricated fiber. The degree to which these structural non-uniformities affect the propagation of the fundamental mode has not been completely understood. Awareness of the sensitivity different fiber properties have to lattice imperfections and the degree of structural variations that can be tolerated will be helpful tools for future PCF designs.

Previous studies that have been performed in this area focus predominantly on calculating the birefringence induced from reduced symmetry in the lattice of a PCF [71-75]. The structural variations analyzed are typically not random in nature [72, 73] and therefore do not accurately represent those that result from fabrication. Practical laboratory or industrial use of PCFs for single-mode transmission, dispersion compensation, or white light generation necessitates an understanding of the birefringence as well as the loss and dispersion properties of the fabricated fibers. Multi-core PCF devices such as filters, couplers, and polarization splitters [69, 76] depend on the predictability of coupling behavior between cores. Therefore, in this

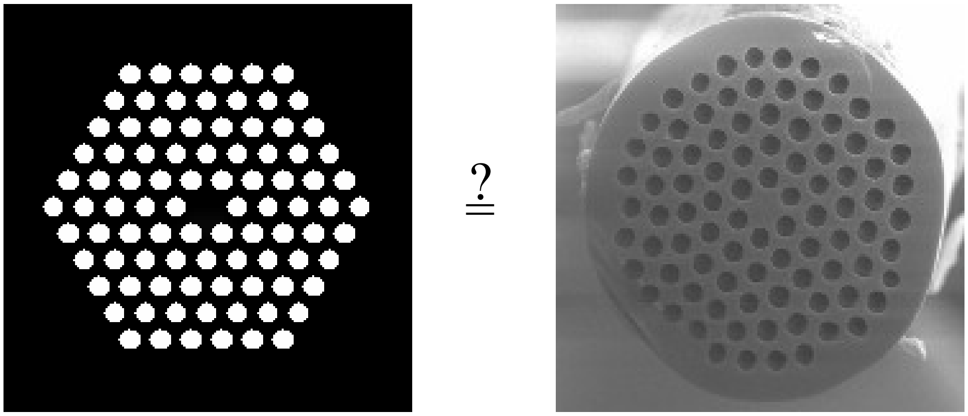

Figure 7-1. The simulated, ideal PCF is compared to an actual fabricated PCF on the right. [Université de Franche-Comté -- Laboratoire d'Optique http://imfc.univ-fcomte.fr/lopmd/onl/frameonl2.htm]

chapter, we study the effect of stochastic variations in a PCF cross-section on the birefringence, the confinement loss, and the dispersion of a single core PCF and on the coupling length of a two-core PCF.

Method

Numerical simulations based on the multipole method are used to determine the mode effective indices of the PCF structures studied. The presented results are a combination of data from a program written by the author and from the CUDOS MOF UTILITIES Software created and distributed by the University of Sydney [3]. The precision of the calculated mode indices is at least 1e-11 for the real part [3] and the precision for the imaginary part of the index is 1e-15 [63]. Because the smallest index differences examined in this paper are on the order of 1e-6, we are confident about the numerical precision of our modeling tool.

The fibers simulated are composed of air holes arranged in a triangular lattice and centered around a silica defect where the light is guided. The structure of a PCF is completely described by two parameters: the air hole diameter, d, and the air hole separation or pitch, Λ. The effects of variations in the air hole size (d) and in the location of the air holes (Λ) are analyzed separately by generating a Gaussian distribution of random values for d or Λ with standard deviations δd or δΛ and mean values d_o or Λ_o. Each air hole in the fiber cross-section is independently assigned a value for the given parameter from the distribution in order to create one test fiber. An illustration of these terms and variations appears in Figure 7-2 as well as an example distribution for the pitch. As shown in Figure 7-2(a), variations in Λ are two dimensional, therefore random in both magnitude and direction. Fiber non-

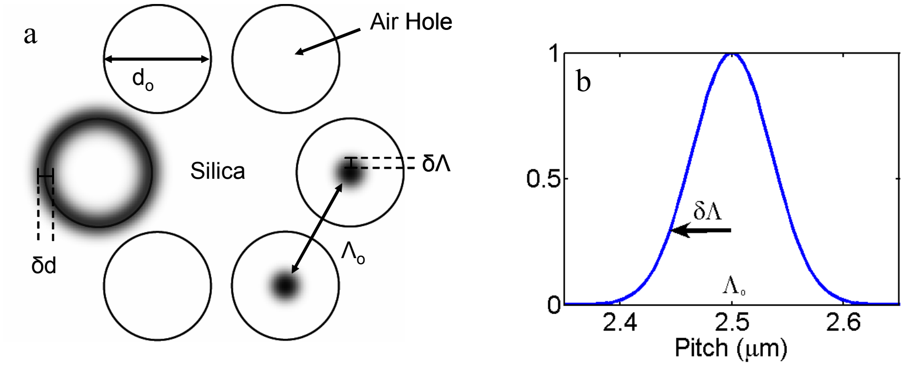

Figure 7-2. An example of the geometry analyzed including definitions of important parameters and variations, a), and an example distribution for the value of the pitch with the average value and standard deviation indicated, b).

uniformities are quantified through the definition of a percentage of variation as the ratio of the standard deviation to the mean of the distribution (ie. $\delta d/d_o$ or $\delta\Lambda/\Lambda_o$) times 100. The range of percentages was chosen to practically represent the degree of irregularity in current PCFs. Example cross-sections are shown in Figure 7-3 for a single core PCF with the two types of variations for a 1% and a 4% degree of variation.

The wavelength of light is 1.55 μm unless otherwise stated and the index of refraction of silica is determined according to the Sellmeier equation [7]. A minimum number of air holes are simulated without sacrificing accuracy in order to maintain manageable computation times.

Variation in air hole size, d

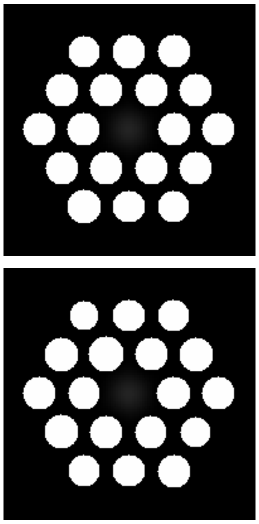

Variation in air hole separation, Λ

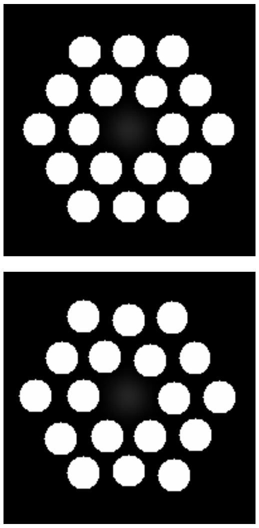

Figure 7-3. Illustrations of the two types of variation and two different degrees of variation for of a single core PCF with Λ_0= 2.5 μm and d_o/Λ_0 = 0.70.

Birefringence

Theoretical calculations based on group theory have shown that fibers with six-fold rotational symmetry, like the standard triangular lattice PCF, will never show splitting in the fundamental mode [64]. Small imperfections in the photonic crystal lattice that are produced during the fabrication process, however, create asymmetries that break the degeneracy and lead to birefringence. The birefringence, defined as the difference in the index of the x and the y polarized modes, was calculated for the fundamental mode of fibers with randomly generated structural variations and the results appear in Figure 7-4. The average value for the pitch was chosen to be Λ_o = 2.5 μm for two different air hole sizes: d_o = 2.25 μm and d_o = 1.75 μm.

An image of the energy distribution of the fundamental mode of each fiber is inset in Figure 7-4. The marker indicates the average value for the birefringence of thirty random structures with each type of variation at each percentage variation, while the bars represent the spread or standard deviation of the data set. The dotted lines demonstrate a linear relationship between the induced birefringence and the percentage variation, therefore supporting earlier results obtained in numerical simulations using the plane wave expansion method [75]. With the data presented here, these conclusions are extended to fibers with much larger air holes. For the two air hole sizes studied, we found that fibers with larger air holes experience a greater induced birefringence than fibers with smaller air holes (Figure 7-4). In fact, the values for the birefringence appearing in Figure 7-4 are more than an order of magnitude larger than the values calculated by Reference [75] for fibers with even smaller air holes (d/Λ = 0.46 and λ/Λ = 0.48) and the same degree of lattice nonuniformity [75]. As shown in Figure 7-4(a), birefringence comparable to standard

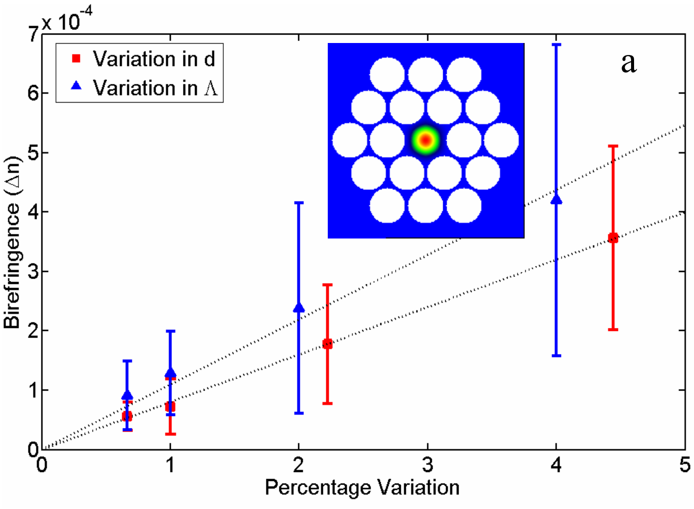

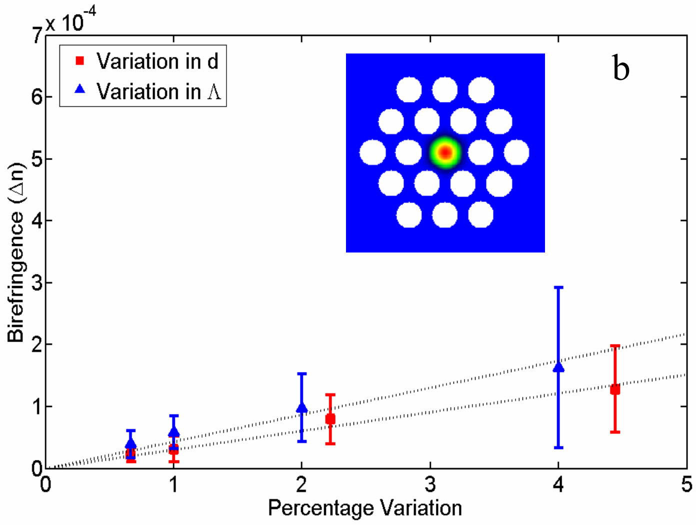

Figure 7-4. The calculated birefringence for two different fibers with Λ_o = 2.5 μm and λ = 1.55 μm: (a) d_o = 2.25 μm therefore $d_o/\Lambda_o = 0.90$ and (b) d_o = 1.75 μm therefore $d_o/\Lambda_o = 0.70$. Markers indicate the average birefringence for a data set of 30 random structures for each percentage variation and each type of variation, while the bars represent the spread or standard deviation. The fit is linear. Insets display the fundamental mode for the fibers calculated.

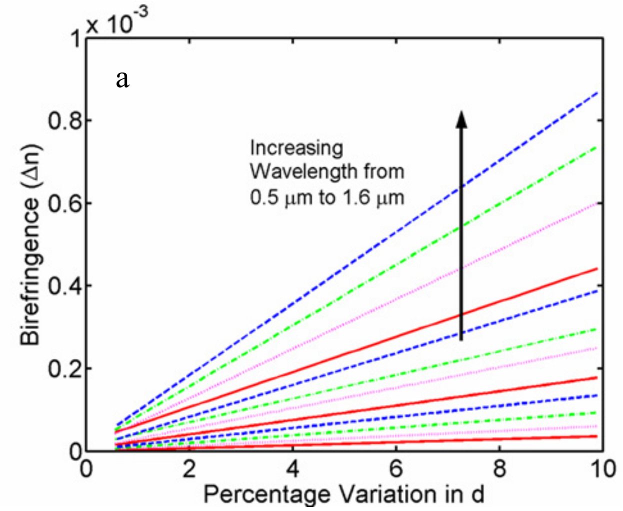

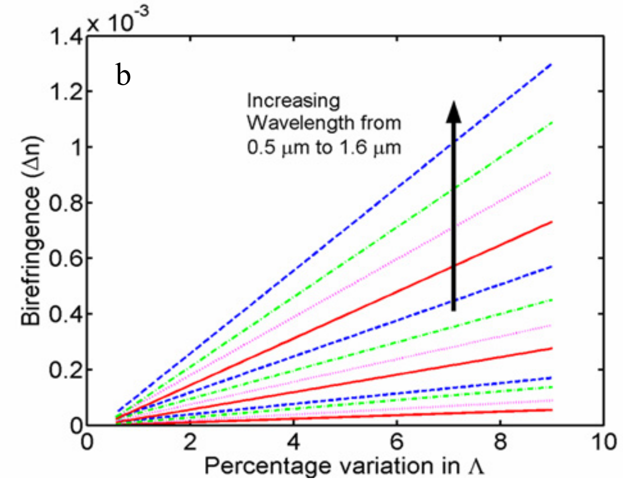

Figure 7-5. The birefringence is shown as a function of the variation in the air hole size (a) and the air hole location (b) for several values for the wavelength. The fiber is a single core PCF with $d_o/\Lambda_o = 0.90$ and $\Lambda_o = 2.5$ μm.

polarization maintaining fibers can be induced from a relatively low degree of random structural nonuniformity in PCFs with air holes that are large relative to the pitch. In Figure 7-5, the birefringence as a function of the percentage variation is plotted for the two types of variation and over several wavelengths for the PCF with larger air holes, $d_o/\Lambda_o = 0.90$. As the wavelength increases, the mode field area increases and more of the cladding is sampled by the mode; therefore, smaller variations in the photonic crystal cladding result in a higher induced birefringence.

Confinement loss

Due to the finite nature of the photonic crystal lattice in PCFs, all modes are leaky and the resulting confinement loss can be calculated from the imaginary part of the mode index using Eq. (7.1):

$$Loss(dB/km) = \frac{20}{\ln(10)} \frac{2\pi}{\lambda} \Im(n_{eff}) \times 10^9 \tag{7.1}$$

where λ is the wavelength in units of μm and n_{eff} is the effective mode index. Loss calculations were performed on a PCF with average parameter values of $\Lambda_o = 2.5$ μm and $d_o = 2.25$ μm, therefore $d_o/\Lambda_o = 0.90$. In Figure 7-6, the markers represent the calculated loss for thirty randomly generated structures with each type of variation for each percentage variation. Although the average loss as well as the spread in the loss values increase with the degree of random imperfections in the fiber structure, the loss remains much below the actual loss of current PCFs, which is dominated by Rayleigh scattering and IR absorption for index guiding PCFs. Similar results were also found for a different fiber with smaller air holes. Thus, the impact of the imposed structural

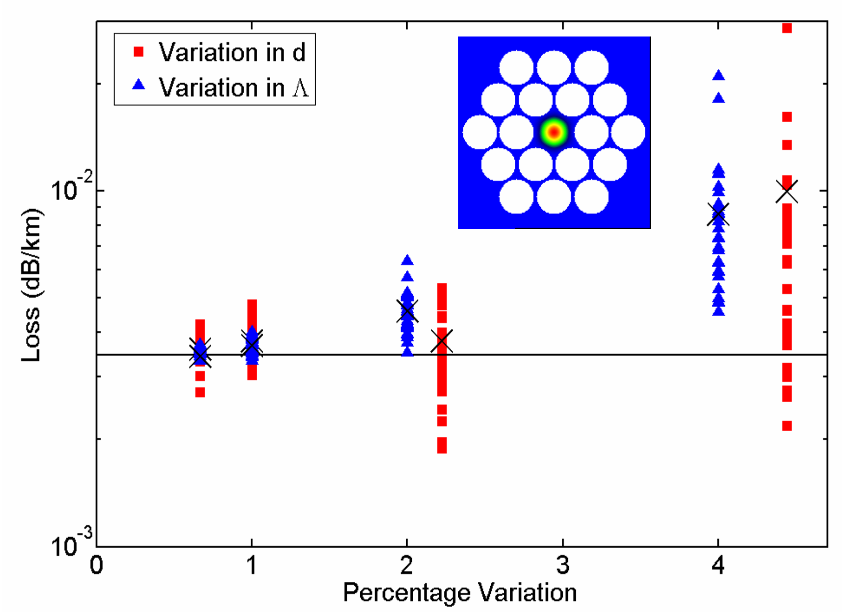

Figure 7-6. Loss plotted versus the percentage variation; the solid line is the predicted loss for the structure with a perfect lattice. The markers represent the values for the loss calculated from 30 random structures for each percentage variation and type of variation. The X indicates the average loss for the data set. Inset is an image of the fundamental mode of the fiber with $\Lambda_o = 2.5$ µm and $d_o = 2.25$ µm, λ=1.55 µm.

irregularities on the actual propagation loss is inconsequential for PCFs with low confinement loss.

Dispersion

The design of PCFs demonstrating novel dispersion properties, such as ultra-flattened dispersion and anomalous dispersion at shorter wavelengths than 1.3 µm, relies on the accuracy of numerical simulations for predicting these behaviors and for easily testing new ideas. PCFs characterized by dispersion properties that cannot be exhibited by conventional fibers, such as ultra-flattened or oscillating dispersion, tend to fall within a cutoff region [29, 77]. This region is defined by the transition the mode-field area (MFA) experiences as the wavelength increases and the mode changes from being well confined with low loss to a high loss, space filling mode [29, 77]. PCFs whose dimensions fall within this region are also predicted to be extremely sensitive to lattice imperfections [29, 77]. We calculated the dispersion for a standard single core PCF with the average parameters $\Lambda_o = 0.8$ μm and $d_o = 0.56$ μm, therefore $d_o/\Lambda_o = 0.70$, over a wavelength range of 0.4 μm to 1.7 μm. The dimensions of this PCF and the span of wavelengths cross the cutoff region. The dispersion is calculated from the second derivative of the mode index with respect to wavelength using Eq. (7.2):

$$D = \frac{-\lambda}{c}\frac{\partial^2 n_{eff}}{\partial \lambda^2} \tag{7.2}$$

The results appear in Figure 7-7, where the markers represent the calculated zero dispersion wavelengths (ZDWs) for thirty randomly generated structures with each type of variation for each percentage variation. At the shorter ZDW, a percentage variation in the fiber parameters of about 4% or less will lead to a calculated ZDW within approximately ±20 nm of the predicted value from a perfect lattice. Near the second ZDW, the MFA has increased as the mode becomes less well confined and variations less than 2% are required in order to attain the same amount of certainty in the ZDW. Over the entire wavelength range examined, the MFA increases by a factor of three and the spread in calculated values for the dispersion as a function of wavelength increases dramatically but then begins to decrease again when leaving

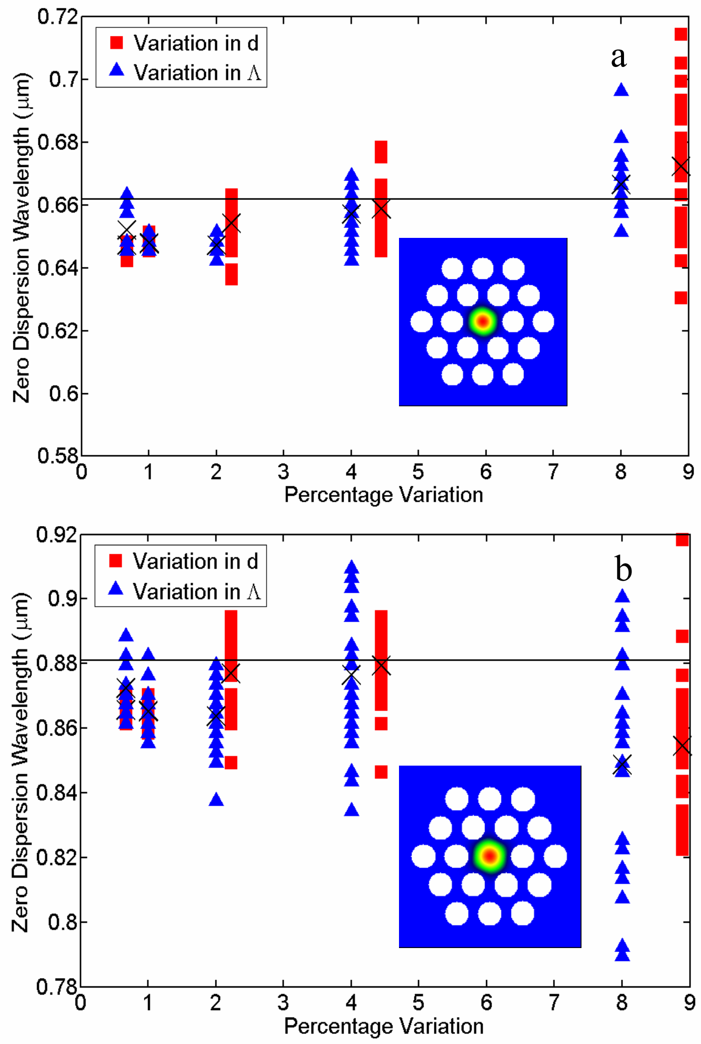

Figure 7-7. The two zero dispersion wavelengths for a fiber with d_o/Λ_o = 0.70 and Λ_o = 0.8 μm are plotted versus percentage variation. The markers indicate the values calculated for 30 randomly generated structures for each percentage variation and for two types of variations. The X represents the mean of the data and the solid line indicates the value for the perfect structure. The insets display the fundamental mode for the fiber at the respective wavelength.

the cutoff region. These results support the existence of a cutoff region where structural variations have a significant impact on the dispersion.

PCFs with large air holes can be designed specifically for use in supercontinuum (SC) generation where high effective nonlinearities are required. For a wavelength range of 0.5 μm to 1.6 μm, we calculated the dispersion of a typical highly nonlinear fiber (HNLF) with $\Lambda_o = 2.5$ μm and $d_o = 2.25$ μm, therefore $d_o/\Lambda_o = 0.90$ (not falling in the cutoff region). A percentage variation of 2% or less resulted in an uncertainty in this structure's ZDW of about ±4 nm. Since SC generation using direct degenerate four-wave mixing has been demonstrated through numerical simulations to be robust to variations in the ZDW of less than ±3 nm [78], variations of less than 2% are necessary for the HNLF studied here. The MFA increases by a small amount (~25%) over the wavelength range examined and the uncertainty in the dispersion as a function of wavelength remains relatively constant, increasing only slightly. These calculations suggest that the dispersion properties of PCFs not falling in the cutoff region are relatively robust to small imperfections in the crystal lattice.

Two-core coupling

PCFs with two defects, or two-core PCFs, have been designed with unique air hole sizes and arrangements in order to customize the coupling properties between cores. Practical application of these concepts requires accurate predictions of the coupling, which may be altered by unintentional imperfections in the fabricated fiber [79]. A key parameter for describing the coupling in a two-core structure is the beat length or coupling length. The fundamental mode of these fibers is split into four modes with slightly different indices and the coupling length is defined here as π

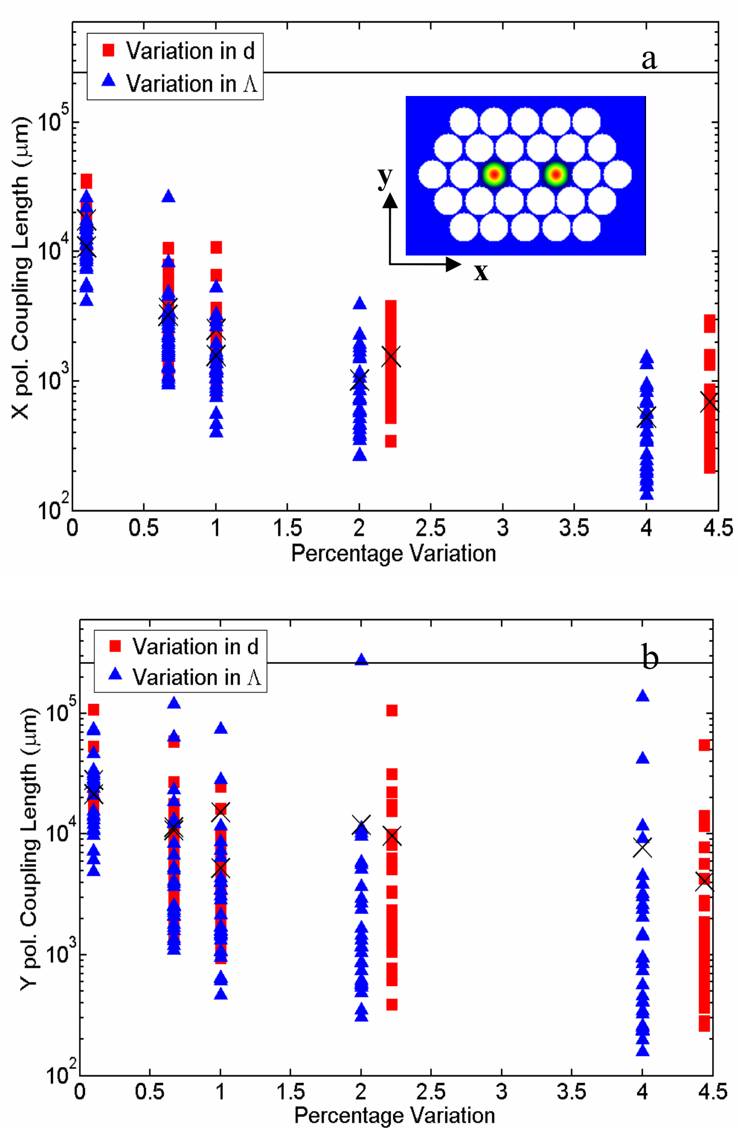

Figure 7-8. The markers represent the calculated beat lengths for the x and y polarizations in (a) and (b), respectively; the X indicates the average for the data set. The solid lines are the predicted values for the structure with a perfect lattice. 30 random structures were simulated for each percentage variation for each type of variation. The inset in (a) displays the fundamental mode for the fiber calculated with $\Lambda_o = 2.5$ μm and $d_o = 2.25$ μm, therefore $d_o/\Lambda_o = 0.90$, and $\lambda = 1.55$ μm.

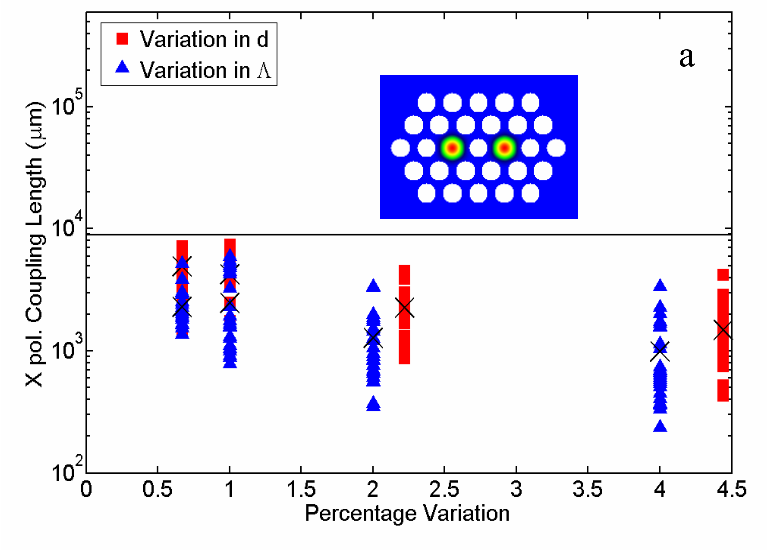

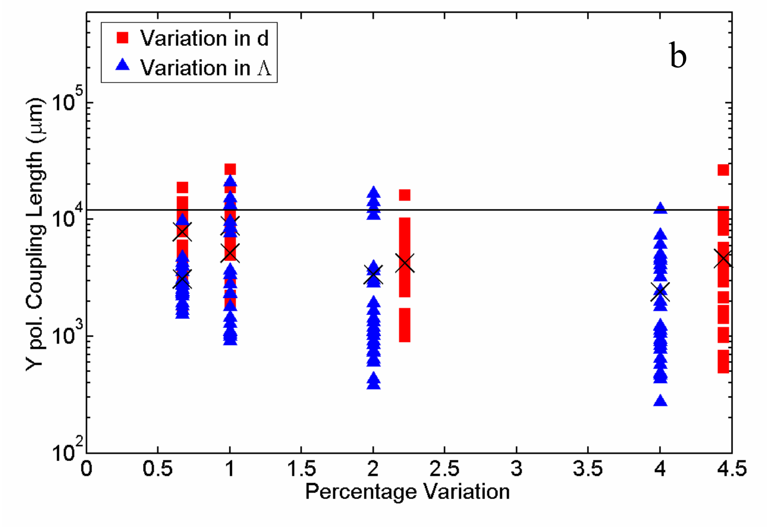

Figure 7-9. The markers represent the calculated beat lengths for the x and y polarizations in (a) and (b), respectively; the X indicates the average for the data set. The solid lines are the predicted values for the structure with a perfect lattice. 30 random structures were simulated for each percentage variation for each type of variation. The inset in (a) displays the fundamental mode for the fiber calculated with $\Lambda_o = 2.5$ μm, $d_o = 1.75$ μm, $d_o/\Lambda_o = 0.70$, and $\lambda = 1.55$ μm.

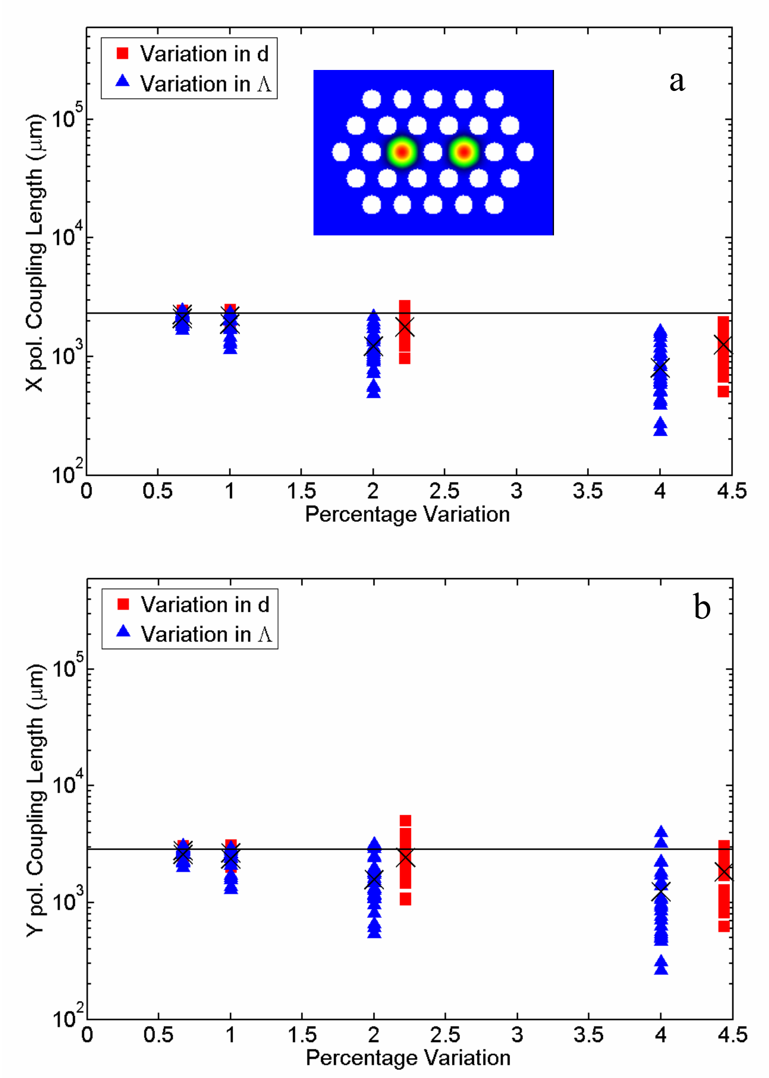

Figure 7-10. The beat lengths for the x and y polarizations are plotted versus percentage variation for two fibers when λ =1.55 μm for d_o = 1.45 μm and d_o/Λ_o = 0.58. The solid lines are the predicted values for the structure with a perfect lattice. The markers represent the calculated values for the coupling length while the X indicates the average for the data set; 30 random structures were simulated for each percentage variation for each type of variation. Insets display the fundamental mode for the fiber calculated.

divided by the difference in the propagation constants of modes with the same polarization. Figure 7-8(a) and Figure 7-8(b) show the calculated values for the beat lengths of the x and y polarizations, respectively, for thirty randomly generated two-core fibers with variations in Λ and in d. The PCF parameters are $\Lambda_o = 2.5$ μm and $d_o = 2.25$ μm, therefore $d_o/\Lambda_o = 0.90$, and a reproduction of the fundamental mode of this fiber is inset in Figure 7-8(a). The calculated beat lengths for the imperfect two-core PCFs differ from the predicted value (solid line) by up to two orders of magnitude even for very small degrees of variation and the spread in these values is quite large; consequently, even a slightly irregular crystalline structure significantly alters the mode propagation in this two-core structure and leads to a lack of certainty in the actual coupling properties of the fiber.

Table 7-1. Summary of the fiber structures used in the two-core simulations.

Λ_o	d_o	d_o/Λ_o	λ	MFA[a]	λ/Λ_o
2.5 μm	2.25 μm	0.90	1.55 μm	0.80	0.62
2.5 μm	1.75 μm	0.70	1.55 μm	1.13	0.62
2.5 μm	1.45 μm	0.58	1.55 μm	1.38	0.62

[a] The mode-field area is normalized to the pitch of the structure squared and calculated from the z-component of the Poynting vector.

In order to isolate the characteristics of this fiber that make it so sensitive to lattice imperfections, we also calculated the beat lengths for two-core PCFs with smaller air holes but with the same average pitch. The results for these fibers appear in Figure 7-9 and Figure 7-10. In Figure 7-9 the two-core PCFs have d_o = 1.75 μm, and therefore $d_o/\Lambda_o = 0.70$. In Figure 7-10, d_o = 1.45 μm and $d_o/\Lambda_o = 0.58$. See Table 7-1 for a summary of the parameters of the two-core fibers simulated. For both of these fibers, the properties of the fundamental mode, such as the MFA, the coupling, and the real part of the mode index, change insignificantly with the addition of a third ring of air holes, hence only two are used here in order to reduce computation time while maintaining accuracy. The smaller air holes found in these fibers reduce the index contrast between the air hole cladding and the core, resulting in a less confined mode with a larger area and therefore stronger coupling between the cores. The calculated values for the beat lengths in Figure 7-10 are close to those of a perfect structure for percentage variations less than 2%. This fiber has the smallest air holes and is the least sensitive to lattice irregularities of the fibers studied, with the fiber in Figure 7-8 experiencing the most effect. This behavior demonstrates that the air hole size and the coupling strength determine a two-core fiber's vulnerability to fabrication induced nonuniformities.

Conclusion

The susceptibility of a PCF to being fabricated with unintentionally high birefringence is strongly influenced by the air hole size of the fiber relative to the pitch, and birefringence comparable to polarization maintaining fibers can be induced from a relatively low percentage variation in the photonic crystal lattice when the air holes are large. For practical PCFs with very low confinement loss, the effect of lattice imperfections will not be discernable, although their impact on other types of loss, such as scattering, is unknown. The dispersion properties of PCFs are most susceptible to nonuniformities if the fiber falls within the cutoff region; however, outside of this region the fibers are more robust. For a typical HNLF, SC generation is predicted to tolerate variations in the fiber parameters of less than about 2% when the fiber is not within the cutoff region. Lastly, the coupling length has been shown to be very sensitive to perturbations in the lattice surrounding the defects when the air holes are large. Two-core fibers with smaller air holes and shorter coupling lengths are remarkably more robust. These results have strong implications for applications such as filters, couplers, and polarization splitters whose performance directly depends on the coupling properties of two or more cores.

The work presented in this chapter has been published in a the Optics Express journal and in a conference proceedings [80, 81].

Chapter 8

INDEPENDENT CORE PROPAGATION IN TWO-CORE PHOTONIC CRYSTAL FIBERS RESULTING FROM STRUCTURAL NONUNIFORMITIES

Introduction

The design flexibility and unique propagation characteristics of photonic crystal fibers (PCFs) offer many new possibilities for fiber based devices. Multi-core PCFs with novel air hole arrangements take advantage of these properties for applications such as filters, couplers, switches, and polarization splitters [69, 76, 82]. The realization and performance of these designs depend on the predictability of the coupling behavior between cores. Accurate numerical methods exist for simulating multi-core PCFs and their properties; however, fabrication processes generate random nonuniformities in the photonic crystal lattice that can potentially alter the actual performance of the fiber from that which is predicted by simulation. By imposing random variations in the air hole size and in the air hole location of two-core PCFs and then using numerical simulation tools to calculate certain properties of these fibers, a better understanding of the impact of fabrication induced irregularities can be gained.

The rate and the efficiency of power transfer between cores are important parameters to examine when designing a fiber coupler or any other device that utilizes the properties of a multi-core fiber. Previous work has shown that the rate of power transfer between the cores of two-core photonic crystal fibers, described by the coupling length, can be extremely sensitive to irregularities in the "cladding" of the PCF, or in the lattice surrounding the cores [80]. For large air hole fibers, nonuniformities in the photonic crystal lattice of less than 1% were shown to produce, on average, a deviation in the coupling length of at least an order of magnitude from the predicted value which is calculated from a fiber with a perfect lattice [80]. In this paper, we demonstrate numerically that in addition to decreasing the coupling length, imperfections in the photonic crystal lattice drastically reduce the coupling efficiency, or the fraction of the power that is transferred between cores, depending on the relative size of the air holes. Two-core fibers with relatively small air holes and shorter coupling lengths are markedly more robust to nonuniformities than two-core PCFs with large air holes and long coupling lengths. The coupling efficiency is shown to be minimal for fibers with large air holes when only small nonuniformities are present, resulting in essentially independent core propagation. The effects of imperfections in the lattice on the coupling properties of two-core PCFs, as well as the dependence of this response on the size of the air holes, are explained through a comparison with coupled mode theory.

An obvious approach to achieving independent core propagation in a multi-core fiber is to engineer a long coupling length by increasing the core separation and the mode confinement. This method, however, places restrictions on the fiber design as well as how densely the cores can be packed in a fiber. An alternative solution is to decrease the efficiency of the coupling such that an insignificant amount of power is transferred between the cores regardless of the coupling length or the rate of the coupling. Our results show that structural nonuniformities in two-core PCFs that could be a consequence of normal fabrication processes have the potential to drastically reduce the efficiency of the coupling allowing coupling to be practically ignored. The imperfections in the cladding cause the two cores to become decoupled and, as a result, light propagates essentially independently in each core.

Method

In order to understand how the introduction of nonuniformities affects the core coupling in a two-core PCF, we use a vector normal mode expansion to compare how power in each core fluctuates as a function of the propagation distance for many randomly generated fibers with imperfect lattice structures and for fibers without imperfections. See Chapter 3 for a complete description of the normal mode expansion.

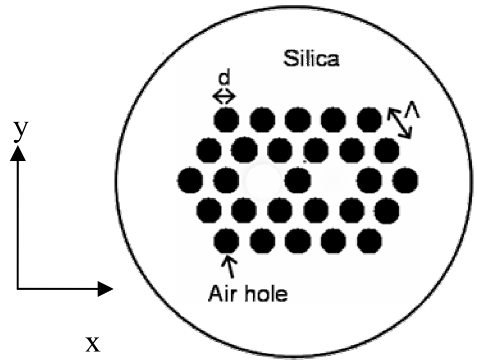

Figure 8-1. Illustration of the endface of a two-core PCF.

The PCFs simulated are composed, in cross-section, of air holes arranged in a triangular lattice around two silica defects separated by a single air hole, as shown in Figure 8-1. The x and y axes are also defined in Figure 8-1. The core area is assigned as the area on either side of a line that bisects the central air hole along x = 0. The input field is x-polarized, $E_y = 0$, and has a Gaussian profile that is centered on the left core with a spot diameter ($1/e^2$ intensity) equal to the pitch. Reflections at the input interface are ignored.

The photonic crystal lattice that makes up the cladding of a PCF is described by two parameters: the air hole diameter, d, and the air hole separation or pitch, Λ. Nonuniformities are introduced into the fiber by independently imposing stochastic variations on the air hole size and on the location of the air holes in the same manner as in Chapter 7 or Reference [80]. Each imperfect two-core PCF is generated by randomly assigning every air hole in the fiber a value from a Gaussian distribution of values for d or Λ. The degree of irregularity in the lattice is defined as the ratio of the standard deviation to the mean of this distribution (ie. $\delta d/d_o$ or $\delta\Lambda/\Lambda_o$) times 100, or as a percentage of variation. The average value used for the pitch is always 2.5 μm, unless otherwise stated, therefore a variation of 1% indicates that the standard deviation of the imposed structural perturbations is 25 nm. The modal fields and the mode propagation constants of two-core PCF structures with and without imperfections are calculated for the wavelength of light of 1.55 μm using numerical simulations based on the multipole method as described in Chapter 5. The highest index mode group contains four modes with slightly different indices whose energy distributions within the individual cores are all approximately Gaussian with azimuthal symmetry, as characteristic of a fundamental mode. The normal mode expansion is truncated after these four lowest order modes since they represent the most significant contribution to the sum due to their large overlap with the input field. Our modeling showed that ignoring the higher order modes results in negligible error because the modal amplitudes, a_j, are extremely small.

Results

The power in the left and right cores as a function of z is shown in Figure 8-2 for a two-core PCF with d/Λ=0.58. Figure 8-2(a) shows the power transfer when the lattice of the fiber is perfectly uniform. Because the two cores are identical, energy is distributed equally between the cores for each of the four modes in the fundamental mode group. The two highest index modes in this group exhibit symmetric behavior when the amplitude of the field is considered, while the lowest two are antisymmetric.

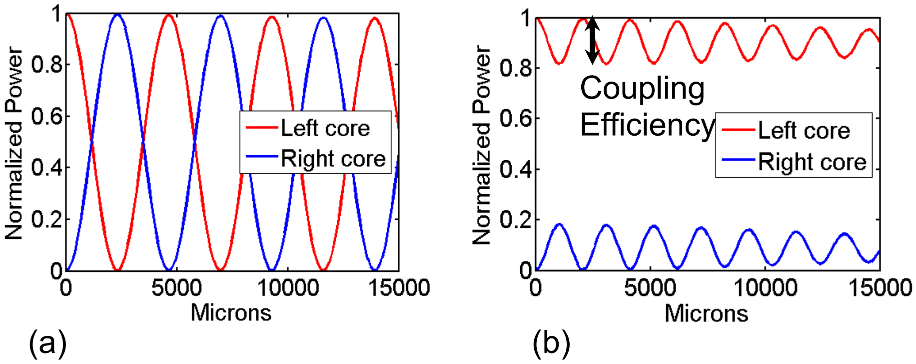

Figure 8-2. The normalized power in each core is plotted versus the propagation distance. The coupling efficiency changes from (a) 1 to (b) 0.20 when a random variation of 2.2% in the air hole size is introduced, Λ = 2.5 μm and d/Λ = 0.58.

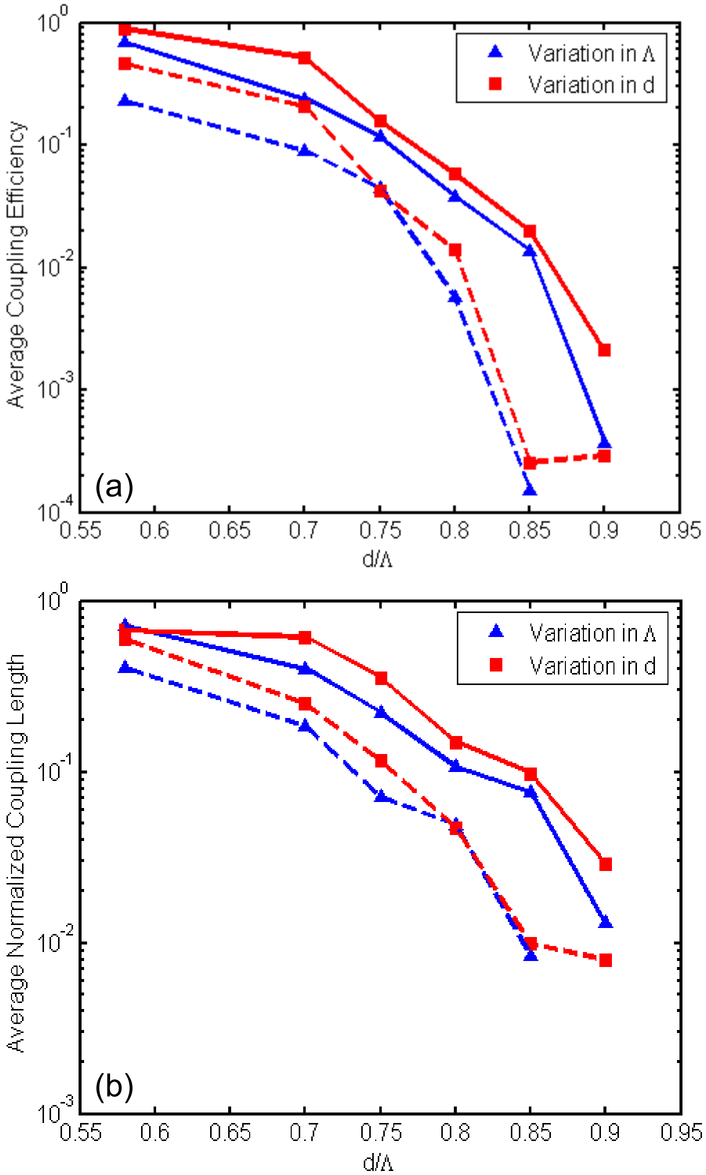

Figure 8-3. The average coupling efficiency (a) and the average coupling length, normalized to the value for a perfectly uniform structure, (b) are plotted vs. d/Λ for a percentage variation of 1% (solid line) and 4% (dashed line), Λ = 2.5 μm. The lines have been added to facilitate the eye.

Polarized light incident on one of the cores is represented by a linear superposition of a symmetric and an antisymmetric eigenmode of the two-core system, each of which propagate according to a slightly different effective propagation constant. The beating of the eigenmodes causes power to oscillate between cores as a function of the propagation distance along the fiber. Figure 8-2(a) shows that, as expected, after a propagation distance equal to the coupling length, ~2000μm, one hundred percent of the power transfers from one core to the other because the energy is equally distributed between the cores for the eigenmodes of the structure. Introducing a random variation of 2.2% in the air hole size caused, in this particular structure, the coupling length to be reduced by half and the efficiency of the coupling to decrease to 20% as shown in Figure 8-2(b). The definition of the coupling efficiency as it is referred to elsewhere in this chapter is illustrated in Figure 8-2(b).

In Figure 8-3(a), the coupling efficiency is plotted versus the relative air hole size, d/Λ, for two different values of the percentage variation for each type of variation. Each marker represents the average efficiency of a data set containing thirty randomly generated two-core PCFs. As the relative size of the air holes increases, and as the nonuniformity in the fiber increases, the coupling efficiency decreases. Large air hole two-core fibers exhibit extremely low coupling efficiency; for example, a PCF with d/Λ=0.90 and structural imperfections of only 1% will have a coupling efficiency, on average, of less than 1%.

The coupling length exhibits a similar response to lattice variations, as shown in Figure 8-3(b), where the average normalized coupling length is plotted versus d/Λ. In order to examine the relationship between these two properties of two-core PCFs, the coupling efficiency is plotted versus the coupling length in Figure 8-4 and Figure 8-5 for different values of d/Λ. Each marker represents the coupling efficiency and

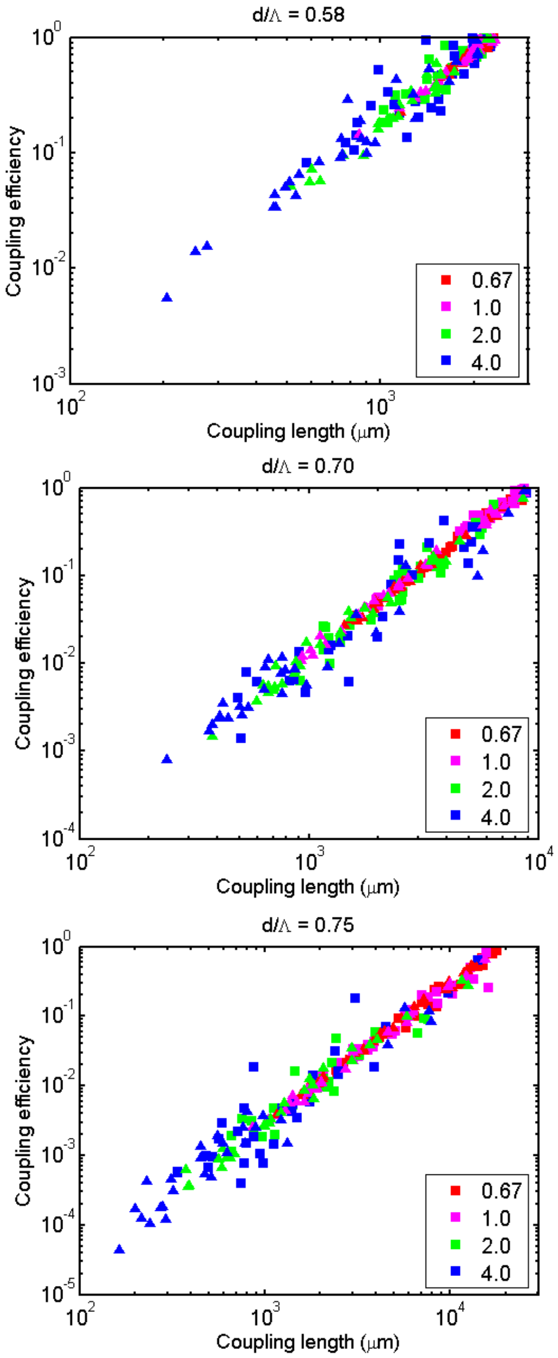

Figure 8-4. The coupling efficiency vs. the x polarization coupling length for $\Lambda = 2.5$ μm and $d/\Lambda = 0.58$, 0.70, and 0.75, from top to bottom. Note that the axis scaling differs for each plot.

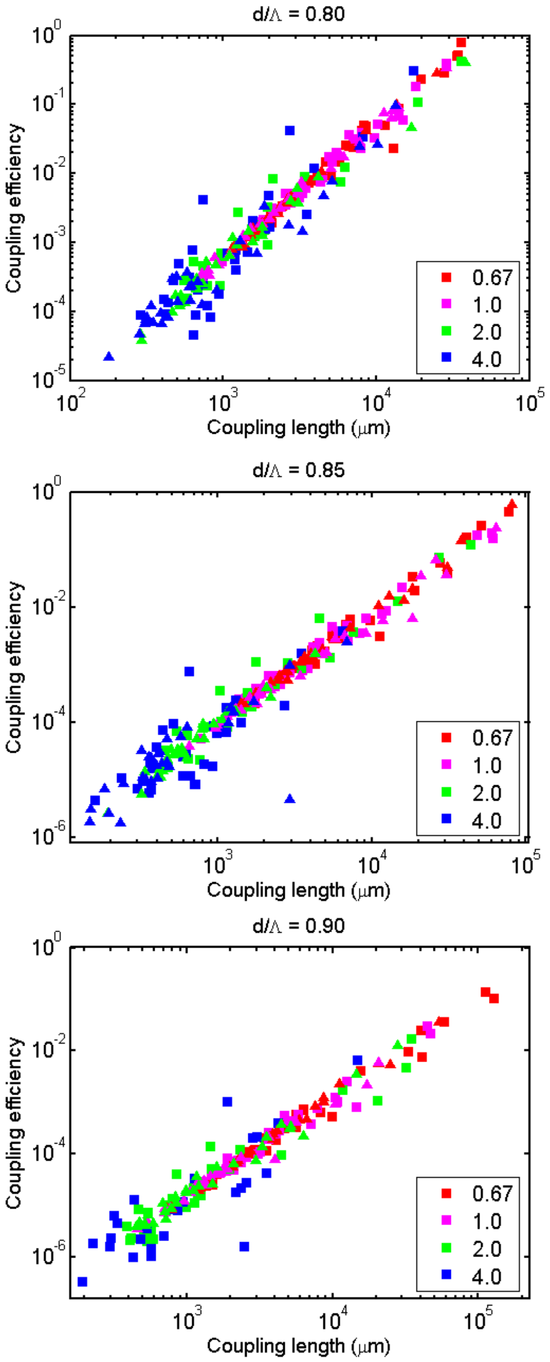

Figure 8-5. The coupling efficiency vs. the x polarization coupling length for Λ = 2.5 μm and d/Λ = 0.80, 0.85 and 0.90 from top to bottom. Note that the axis scaling differs for each plot.

the coupling length of a randomly generated two-core fiber with variations of 0.67% to ~4% in either the air hole size or the air hole separation. Fibers with large air holes, see the bottom of Figure 8-5, typically exhibit a coupling efficiency of less than 1%.

All the structures examined in Figure 8-4 and Figure 8-5 are multi-moded. By increasing the wavelength to pitch ratio (i.e. the normalized wavelength) for the relative air hole sizes studied here, or by decreasing the value of d/Λ into the endlessly single mode regime, a single mode will be guided. Changing the structure by increasing the normalized wavelength results in a larger mode size as does decreasing the air hole size; therefore, altering the normalized wavelength in this manner should follow the same trend shown in Figure 8-4 and Figure 8-5 for changes in d/Λ. This is indeed the case. Data in Figure 8-4 and Figure 8-5 moves up and to the left as the structure becomes less multi-moded because of changes in the air hole size or in the normalized wavelength. This behavior demonstrates that two-core fibers become less sensitive to variations as the coupling length decreases and the mode field area becomes larger.

Upon inspection of the plots in Figure 8-4 and Figure 8-5, the efficiency is noticed to decrease at a quicker rate than the coupling length in a clear power relationship, inferred from the linear distribution of data points in the log-log plots. The fact that the data exhibits similar slopes across all plots indicates that the nature of the relationship between these parameters does not appear to depend on the relative air hole size. A linear fit of the log-log data is demonstrated in Figure 8-6 for three different relative air hole sizes. The slope values are given in Table 8-1 for fits to each of the plots in Figure 8-4 and Figure 8-5 and reveal an approximately quadratic relationship between the two parameters. In order to develop an understanding of this

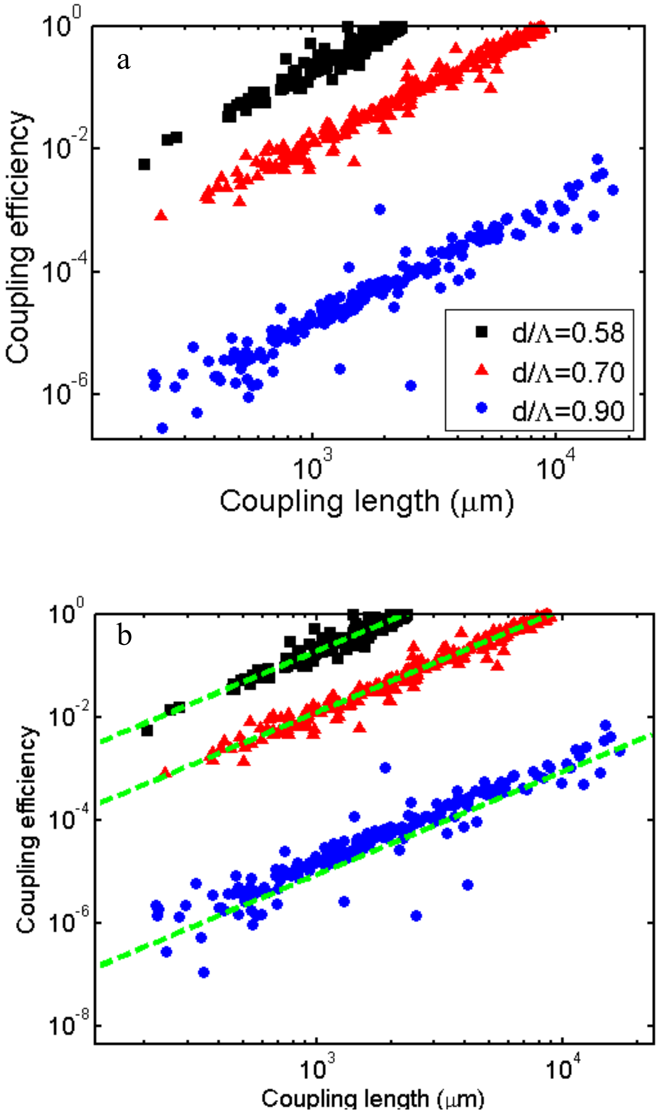

Figure 8-6. Data for three different relative air hole sizes from Figure 8-4and Figure 8-5 is re-plotted in a) and then shown with the linear fits to the log-log data, b), as described in Table 8-1.

relationship, we applied coupled mode theory to two-core PCFs with imperfect lattice structures.

Table 8-1. The slopes of linear fits to the log-log data of Figure 8-4 and Figure 8-5.

d/Λ	Slope
0.58	1.93
0.70	1.94
0.75	1.93
0.80	1.88
0.85	1.92
0.90	1.91

Couple Mode Theory

In coupled mode theory (CMT), each core is treated as an independent waveguide that is perturbed by the presence of fields propagating in the other core. When the field from one core enters the high index core region of the second waveguide, it becomes a source for a new field. See Chapter 3 for a complete derivation and discussion of the conventional CMT used here. Because a different notation is used for the arguments presented in this chapter, the expressions for the power found in Eq. (3.12) are repeated [11].

$$P_b(z) = |b(z)|^2 = \left|\frac{K_{ab}}{\psi}\right|^2 \sin^2 \psi z,$$

$$where: \psi = \sqrt{\frac{(\beta_b - \beta_a)^2}{4} + K_{ab}K_{ba}} \tag{8.1}$$

The coupling properties of the two-core PCF are again defined from the power transfer, $P_b(z)$. The coupling length is the distance, L_c, at which the power in waveguide *b* has oscillated to its first maximum, ie. $\psi L_c = \pi/2$. The coupling efficiency can be defined from Eq. (8.1) as the maximum possible value for the power in waveguide *b*, or $|K_{ab}/\psi|^2$. As the mismatch between the modes, β_b-β_a, increases, it can be seen from these relationships that the coupling efficiency and the coupling length will decrease. When the variable ψ is solved for in the expression for the coupling length and substituted into the expression for the coupling efficiency, the efficiency is shown to be proportional to the square of the coupling length:

$$Efficiency = \frac{4|K_{ab}|^2}{\pi^2} L_c^2 \tag{8.2}$$

Improved coupled mode theory, where the coupling is no longer assumed to be weak, results in the same relationship between the efficiency and the coupling length as in Eq. (8.2), but with a different proportionality constant still dependent on the mode overlap that is modified by an amount determined by the cross power [10, 11]. For simplicity, we will continue without including the effects of the cross power. The quadratic relationship of Eq. (8.2) substantiates the relationship predicted from the power law fits of the plots in Figure 8-4 and Figure 8-5 and from the values in Table 8-1.

The applicability of CMT can be further assessed by comparing the coupling length, L_c, as calculated from CMT using Eq. (8.2) to the value derived directly through the multipole method for a perfect structure. Beginning with Eq. (8.2), if K_{ab} is assumed to be constant, a quadratic polynomial fit, where the linear and zeroth order terms in the polynomial are forced to be zero, can be applied to the data of Figure 8-4 and Figure 8-5 and the fit parameter can be used to estimate K_{ab}. The assumption that

Table 8-2. The fit parameter, or the coefficient of a quadratic fit to the data in Figure 8-4 and Figure 8-5, is listed according to the relative air hole size. K_{ab} is calculated from the fit parameter according to Eq. (8.2). The final columns compare the coupling length as calculated from the fit using CMT with the value determined directly from the perfect structure.

d/Λ	Fit parameter (μm^{-2})	$\lvert K_{ab} \rvert$ (μm^{-1})	CMT L_c (μm)	L_c (μm)
0.58	1.88E-07	6.82E-04	2.30E+03	2.32E+03
0.70	1.23E-08	1.74E-04	9.01E+03	8.89E+03
0.75	2.74E-09	8.22E-05	1.91E+04	1.83E+04
0.80	4.25E-10	3.24E-05	4.85E+04	4.16E+04
0.85	7.41E-11	1.35E-05	1.16E+05	1.03E+05
0.90	8.66E-12	4.62E-06	3.40E+05	2.49E+05

K_{ab} is constant claims that the induced structural perturbations do not significantly change the amount of overlap between the mode fields of the two cores from that of a uniform two-core PCF. Table 8-2 lists the fit parameters from the quadratic fit for each ratio of d/Λ studied and the coupling coefficient, K_{ab}, as solved for from these values. An estimate of the coupling length for a perfect fiber can be calculated from K_{ab} using CMT and Eq. (8.1) with a mismatch set to zero. These values are compared in the final two columns of Table 8-2 with the coupling length as determined directly from two-core fibers with a perfectly uniform photonic crystal lattice. This comparison implies that CMT in the weak coupling regime adequately describes the behavior of these two-core PCFs when nonuniformities are present. The discrepancy between the values for L_c from the two methods most likely results from neglecting the cross power and from the parameter K_{ab} not remaining constant for all imperfect structures. In fact, for a few cases, generated imperfect two-core PCFs exhibited longer coupling lengths than a fiber with a perfectly uniform lattice; in order to satisfy Eq. (8.2) without predicting an efficiency greater than one, K_{ab} would have to be much different than that of the perfect fiber. The data from these structures was left out of the fit on the basis that it did not satisfy the condition that K_{ab} be approximately constant. Revisiting the power law fit results shown in Table 8-1 with these data points removed leads to fits that are closer to quadratic; for example, for d/Λ=0.58 and d/Λ=0.70, the slopes increase to 1.98 and 1.99 respectively.

Discussion

Nonuniformities in the lattice structure of two-core PCFs cause the cores to be no longer identical, thus creating a mismatch in the indices of the fundamental modes of the two individual cores. A nonzero mismatch results in a decreased coupling length and coupling efficiency as compared with the values that would be predicted from a perfect structure with no mismatch. The coupling properties of a two-core fiber structure with imperfections are determined by the parameter ψ, as defined in Eq. (8.1), which depends on both the mismatch and K_{ab}. Thus, knowledge of K_{ab} alone, which can be gained from simulations based on a perfect two-core fiber, is not sufficient to accurately predict the coupling behavior of a particular PCF that is not completely uniform. It is the magnitude of the mismatch relative to K_{ab} that determines how different the core coupling will be from that of a perfect structure. If K_{ab} is small relative to the induced mismatch, the fiber is more sensitive and the coupling properties will change significantly when nonuniformities—and therefore core mismatch—are introduced. For example, K_{ab}, which is proportional to the mode overlap, will be smaller when the modes are well confined, which is generally true of PCFs with large air holes (see Table 8-2). The magnitude of the mismatch, or β_b-β_a, can be estimated from the birefringence induced in a single core PCF when nonuniformities are introduced into the cladding structure. From Figure 7-4, the average induced birefringence of PCFs with $d/\Lambda = 0.70$ and $d/\Lambda = 0.90$ for Λ=2.5μm are shown to be of approximately the same order of magnitude, $\Delta n \sim$ 1e-4, across percentage variations of 0.67% to 4%. It can be seen in Table 8-2 that this Δn is two orders of magnitude larger than the coupling coefficient, K_{ab}, for $d/\Lambda = 0.90$, while it is actually slightly smaller than K_{ab} for $d/\Lambda = 0.70$. Therefore, the same mode mismatch between two cores will result in a much greater change in the coupling properties when the modes are tightly confined ($d/\Lambda = 0.90$). Clearly, small perturbations have a greater impact on fibers with larger air holes because they are characterized by a relatively large mismatch and a small overlap.

The mismatch and the coupling coefficient do, however, depend on the normalized wavelength. The impact of changing the normalized wavelength on the relative magnitude of these two parameters can be assessed from Figure 8-7. The coupling coefficient is calculated from a perfect two-core structure and Δβ is defined as the mismatch divided by 2 so that the two parameters plotted represent the two contributions to ψ. The mismatch is calculated in the same manner as in Chapter 7 and Reference [80] from the average induced birefringence of a single core PCF with

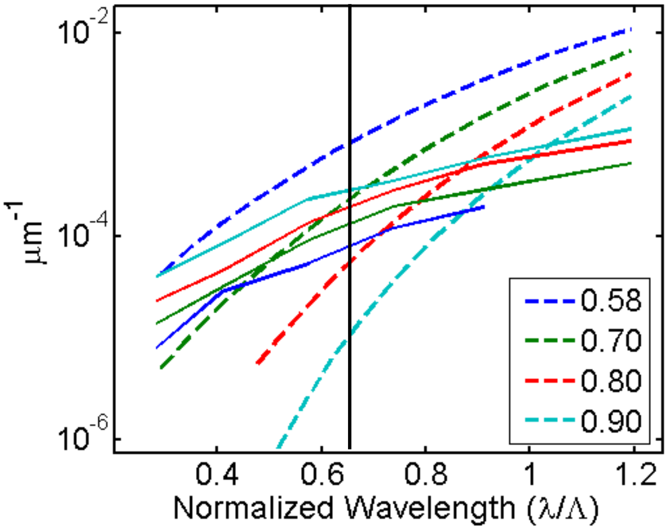

Figure 8-7. K_{ab}, as computed from a perfect structure, (dashed lines) and Δβ, calculated from the birefringence induced from variations in the lattice of a single core PCF, (solid lines) are plotted versus the normalized wavelength. Δβ is the average value for 20 structures with variations of 1% in the air hole separation. The solid vertical line indicates the value for the normalized wavelength used in this paper, λ=1.55, Λ=2.5

variations in the air hole separation of 1%. Regions of high and low sensitivity to lattice imperfections can be predicted from this plot. When $\Delta\beta >> K_{ab}$, a two-core PCF will generally exhibit high sensitivity to variations; this region corresponds to small λ/Λ. On the other hand, when λ/Λ is larger, $K_{ab} >> \Delta\beta$, indicating a low sensitivity to structural nonuniformities. In this region, the PCFs tend to have fewer guided modes. Large air hole fibers will, in general, be sensitive to variations over a larger range of wavelengths and it appears that fibers in the single-moded regime, or

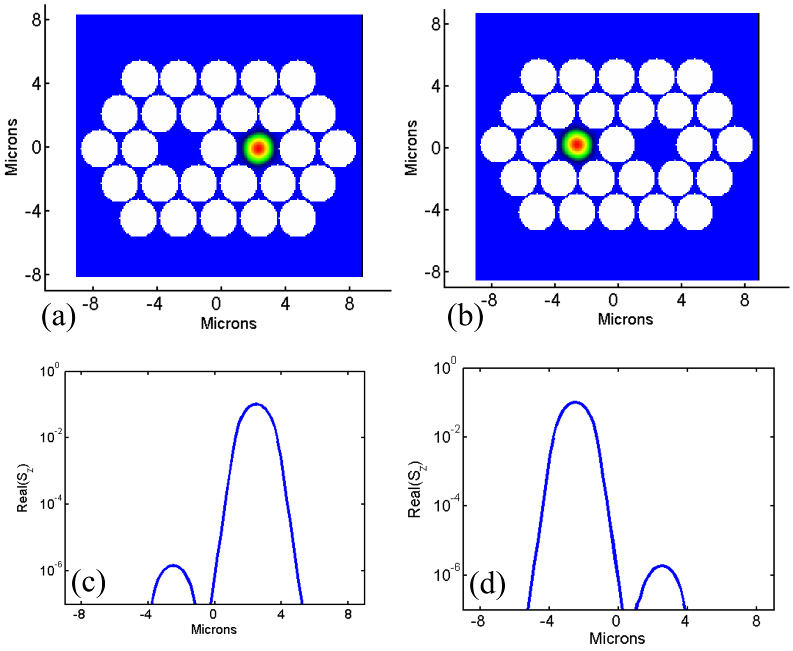

Figure 8-8. A cross-sectional view of the z-component of the real part of the Poynting vector for two of the modes from the highest index mode group of a two-core PCF with $\Lambda = 2.5$ μm and $d/\Lambda = 0.90$ and nonuniformities of 0.67% appears in (a) and (b), while (c) and (d) show the profile along the line where $y = 0$. Similar behavior is observed for the two other modes in the group.

large λ/Λ, are more robust to variations.

Consequences of the non-identical nature of the cores are also manifested through a modification of the mode structure. Exploring the change in the mode shape provides a more intuitive understanding of the impact of nonuniformities on the coupling behavior of two-core PCFs. As stated previously, the eigenmodes of the unperturbed two-core system are perfectly symmetric or antisymmetric in amplitude and distribute energy evenly between the two cores. However, imperfections in the lattice cause the eigenmodes to evolve towards those of the decoupled cores as evidenced by the z-component of the Poynting vector shown in Figure 8-8 for a fiber with d/Λ = 0.90 and variations of 0.67%. The energy of each mode is almost completely concentrated in one core.

Figure 8-9 shows the extinction ratio between the two cores, or the ratio of energy in one core to that in the other, for fibers with different relative air hole sizes and for two degrees of variation in the fiber structure. Each marker is an average over thirty structures. As the percentage of variation in the lattice structure increases, and as the ratio of d/Λ increases, the mode energy becomes more concentrated in one core or the other. When d/Λ is greater than 0.80, the amount of energy localized in one core is, on average, at least three orders of magnitude greater than the energy in the other core for all the fundamental modes of the fiber, even when variations are as small as 1%. The two modes in the fundamental mode group with the highest indices will be almost entirely right (or left) modes while the remaining two modes will be left (or right) modes.

From a scalar point of view, this change in the eigenmode structure explains the observed decrease in the coupling efficiency since the single-core input field closely resembles one of the eigenmodes of the perturbed structure. Light that is incident on one of the cores will now couple predominantly into an eigenmode of the system and travel along the fiber according to the propagation constant of this mode with an almost constant transverse energy profile. Large air hole structures are more sensitive to decoupling because the modes are already well confined in the individual cores.

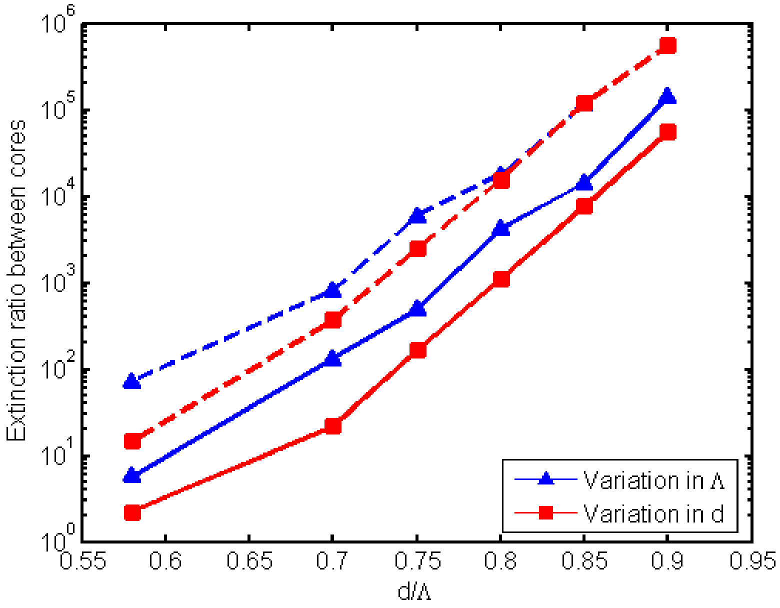

Figure 8-9. The ratio of power in the left core to that in the right core for a mode that is predominantly left is shown as a function of the normalized air hole size, d/Λ, for a percentage variation of 1% (solid line) and 4% (dashed line), Λ = 2.5 μm. The lines have been added to facilitate the eye. The value for a perfect two-core fiber is 1.

For applications where independent core propagation is a requirement, two opposing approaches exist. A long coupling length achieved by increasing the core separation is the obvious method for obtaining this effect. The results presented in this paper, however, illuminate a more simple solution which is to reduce the coupling efficiency. The cores can be packed very closely but in a photonic crystal lattice that is very sensitive to perturbations, such as a PCF with a high ratio of d/Λ or well confined modes. When even slight nonuniformities are present, the two cores in these PCFs can be assumed to be decoupled and light will propagate independently in each core. Typical variations in the structure due to fabrication can actually drastically reduce the coupling length; however, since the efficiency of the coupling is approximately zero, all coupling can be essentially ignored.

We also note that due to the random nature in which the variations were imposed on the structures simulated in this paper, the results should remain robust to additional perturbations not accounted for, such as bending.

Conclusion

Through numerically simulating two-core fibers with different air hole sizes and introducing random variations into their cladding structure, we have shown that the coupling length and the coupling efficiency can be altered by imperfections in the photonic crystal lattice and that the sensitivity of these parameters to imperfections depends on the relative air hole size. Two-core PCFs with relatively small air holes or a large normalized wavelength are more robust to nonunformities where large air hole fibers or fibers with a small normalized wavelength can be extremely sensitive. In fact, for a fiber with d/Λ = 0.90, Λ = 2.5μm, and structural variations of only 1%, the average coupling length can be expected to be reduced by two orders of magnitude and the amount of power transferred between the cores will be less than 0.1%. The observed quadratic relationship between the coupling length and the efficiency was confirmed through a comparison with coupled mode theory and the reduced coupling efficiency was explained intuitively by examining the change in the eigenmode shapes. Our results clearly indicate that practically independent core propagation can be easily obtained in a large air hole PCF when structural imperfections are present.

The work presented in this chapter has been published in the Optics Express journal and a conference proceedings [83, 84]. Additional simulation results for two-core PCFs with variations appear in Appendix B.

Chapter 9

NUMERICAL ANALYSIS OF LIGHT PROPAGATION IN IMAGE FIBERS

Introduction

A fiber bundle contains thousands of high index cores in a common lower index cladding. The core sizes and separations are on the order of a few microns, thus differing from a simple bundle of step-index fibers. The index contrast is increased from that of standard single mode fiber in order to more tightly confine the light and reduce crosstalk between cores. Fiber bundles are used primarily for confocal and multiphoton endoscopic imaging [85-98] but have also been employed in areas such as optical interconnects [99-101], sensing [102], and optical coherence tomography [103]. In coherent fiber bundles, or image fibers, the input and the output are spatially correlated such that an image transmitted through the fiber can be reconstructed from either endface in an identical manner. A distal image is transported to the proximal end of a flexible endoscope allowing *in vivo* observation and measurement of internal tissue or organs. The images, however, have an inherent pixilation due to the individual cores or pixels that transmit the information, and the quality of the image is limited by the size and separation of these cores as well as by the degree of coupling between cores.

Applications for image fibers motivate the production of higher resolution or higher information density fibers with smaller cores that are more closely packed. In general, image fibers with smaller, closer pixels (ie. high core density) are desired in order to reduce endoscope size while retaining a large number of resolvable pixels. Decreasing the fiber dimensions, however, will increase the strength of coupling or crosstalk between cores, resulting in blurred images and a lower signal to background ratio.

Available image fibers manufactured by Fujikura and Sumitomo, for example, already have dimensions well below the acceptable theoretical limit for crosstalk. Numerical simulations of these fibers reveal short coupling lengths relative to the typical length of fiber utilized. That is, the strength of the coupling between adjacent cores is predicted to be such that power will begin to disperse amongst the cores after a propagation distance of much less than a meter, placing impossible limits on the practical use of these fibers. In addition, these image degrading effects are not dramatic in practice. A closer look at these fibers reveals a significant degree of nonuniformity in the size and shape of individual pixels or cores. In this chapter, we will describe how the introduction of nonuniformities disrupts coupling by creating a mode mismatch between adjacent cores. In certain fiber structures, despite high core density, even a small mismatch is sufficient to cause the cores to de-couple. We further verified this behavior using coupled mode theory, suggesting methods for assessing the performance of a particular image fiber and giving guidelines for choosing an image fiber for a particular wavelength.

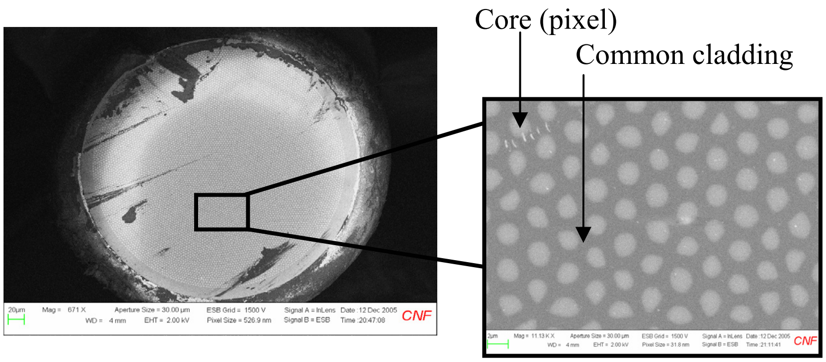

Figure 9-1. SEM images of an image fiber showing the irregularity of pixel size and shape.

The authors anticipate that a greater understanding of coupling in multi-core fibers and the effects of nonuniformities on crosstalk will not only motivate the production of more reliable image fibers but also facilitate the more effective use of existing fibers.

Theoretical analysis

The numerical simulations in this chapter are based on two image fibers manufactured by Fujikura, distributed by Myriad Fiber Imaging Technology, Inc. The fiber specifications are given in Table 9-1 and, unless otherwise noted, the values are those given by the distributor. The samples are approximately one foot in length. These two fiber types were chosen because their dimensions are typical of imaging applications and of current research [87, 88, 94]. SEM imaging was performed on each fiber in order to verify their dimensions and the pixel size for the 350S fiber was corrected. The final column in Table 9-1 provides an estimate for the variation in pixel diameter taken from the standard deviation of elliptical fits to the cores in the

SEM images using an image processing program. The nonuniformity in the pixel cores is evidenced by the SEM image of Figure 9-1. The degree of nonuniformity in the core shape and size observed in these fibers appears to be typical of other commercially available fiber bundles, such as those manufactured by Sumitomo, and has been noted previously [93, 104-109].

Because the coupling behavior between the thousands of cores of an image fiber would be extremely complicated to model, smaller systems of two, three, and seven cores are examined in detail in order to make informed assumptions about the larger system. The nature of the coupling between cores can be understood by calculating the power or energy distribution in each core at different points along the fiber length. In a multi-core system, the power oscillates between cores as a function of the propagation distance, z. The percentage of power transferred between cores is referred to as the coupling efficiency, related to crosstalk, and the rate of power transfer is described by the coupling or beat length. The coupling length and the coupling efficiency are used to quantify the strength of coupling and depend on the

Table 9-1. Image fiber specifications.

Fiber type	# of Pixels	Fiber diameter	Pixel spacing	Pixel diameter (d)	Index contrast	% Variation in pixel size
FIGH-10-500N	10K	600 μm	4.5 μm	2.9 μm	1.5 to 1.446	10 – 15% [a]
FIGH-10-350S	10K	450 μm	3.2 μm	2 μm [a]	1.5 to 1.446	7 – 10% [a]

[a] Value estimated from SEM images of fiber endface

interactions between cores or on the beating of the modes of the fiber. The power can be determined from a normal mode expansion of the field solution in the fiber given a Gaussian single core input field. The method used here follows Chapter 3 and Reference [83].

In Figure 9-2, the power in each core is plotted over z for two-core fibers with dimensions taken from the two image fiber samples of Table 9-1. The energy distribution in the cores at different points along the z-axis is included below Figure 9-2(a). The input field is an x-polarized Gaussian, $E_y = 0$, that is centered on the left core with a spot diameter ($1/e^2$ intensity) equal to the radius of the core. As shown in Figure 9-2, the coupling efficiency is 100% when the two cores have identical diameters, indicating that all the power coupled into the fiber oscillates back and forth between the two cores. The coupling length is defined in Figure 9-2(b) as the distance after which all power, when incident initially on one of the cores, will be coupled into the second core. For the case when the cores are identical, the coupling length for each polarization can be calculated directly from the beat frequency of the modes in the following manner:

$$L_c = \frac{\pi}{\beta^e - \beta^o} = \frac{\lambda}{2(n_{eff}^e - n_{eff}^o)} \tag{9.1}$$

where e and o indicate the even and odd modes. This distance is 0.25 m for fiber 500N and 1.4 cm for fiber 350S. Because practical applications with fiber bundles use lengths much longer than these distances, coupling between two cores should be readily observed in endoscopic systems.

A three-core system can be generated by adding another core to a two-core system in two possible formations as illustrated in Figure 9-3 and Figure 9-4 for fiber type 350S. In Figure 9-3, the two unique energy distributions of the six modes of a

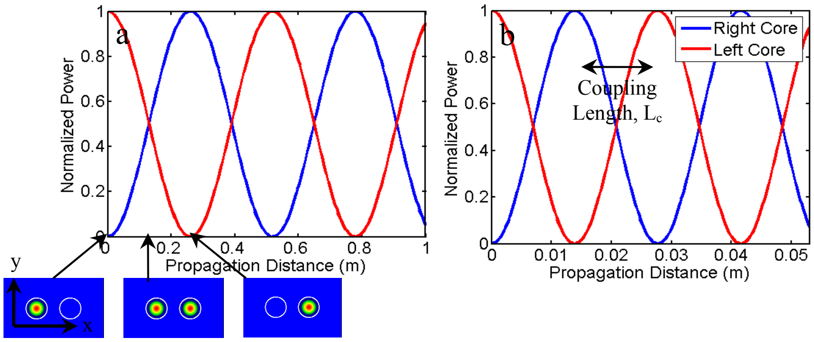

Figure 9-2. The normalized power in each core of a two-core fiber is plotted as a function of the propagation distance. The two cores have identical diameters. a) FIGH-10-500N, $L_c = 0.25$ m; b) FIGH-10-350S, $L_c = 1.39$ cm. $\lambda = 600$ nm.

linear three-core system are shown. One of the six modes is degenerate while the remaining four modes are non-degenerate. When light is incident on the central core, 50% of the power is coupled into each of the outer cores, returning eventually to the central core, and the process repeats. The triangular three-core system, as shown in Figure 9-4, has two two-fold degenerate modes and two non-degenerate modes. Although the oscillating behavior of this core arrangement is similar to the linear three-core system, complete extinction no longer occurs. Note also that the coupling length in these three-core fibers is shorter than the two-core fiber of Figure 9-2(b).

In an image fiber, a single core has not just one but six nearest neighbor cores and the impact of these additional cores is to increase the rate at which power is transferred between the cores. In Figure 9-5, the power in each core of a seven-core fiber is plotted versus the propagation distance when light is incident on the central

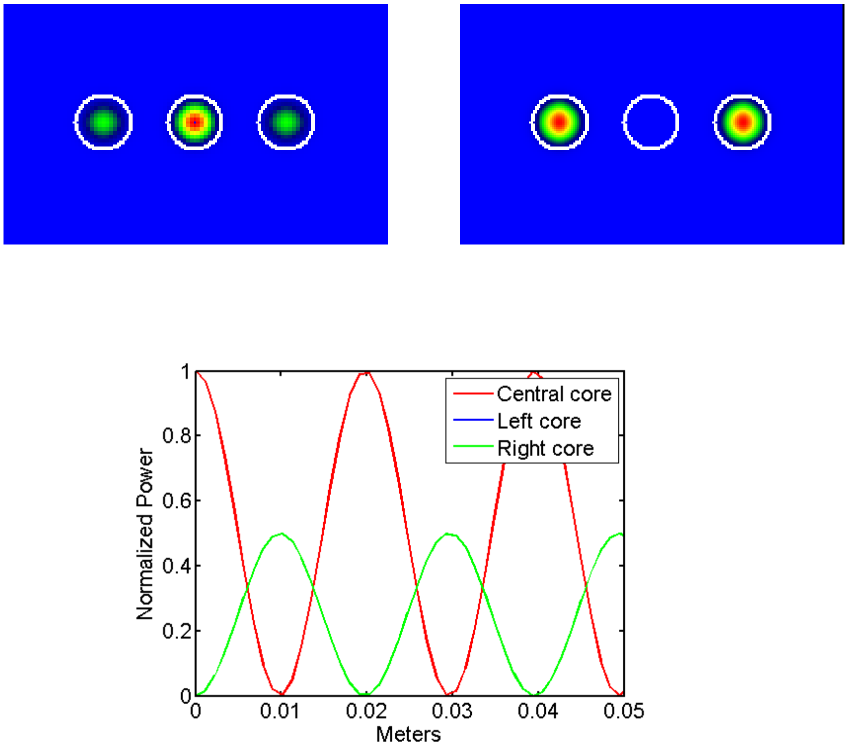

Figure 9-3. The two unique energy distributions for the modes of a linear three-core 350S fiber are shown at top. The plot is of the power in each core as a function of the propagation distance when light is incident initially on the central core. The power in the left and right core show identical behavior and therefore can’t be distinguished on the plot.

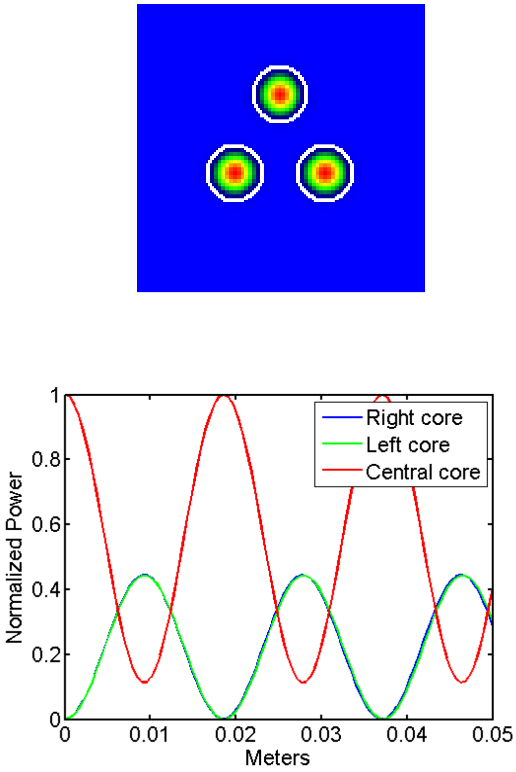

Figure 9-4. The energy distribution for the modes of a triangular three-core 350S fiber are shown at top. The plot is of the power in each core as a function of the propagation distance when light is incident initially on a central core. This plot is identical regardless of the incident core. The power in the left and right core show slightly different behavior because of the polarization of the incident light.

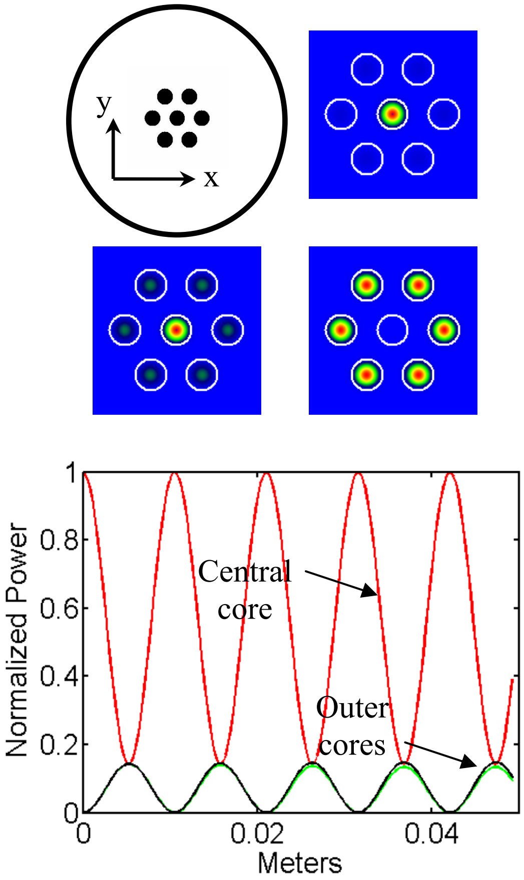

Figure 9-5. The power in each core of a seven-core FIGH-10-350S fiber when the input is in the central core, λ = 600 nm. The three unique energy distributions of the fourteen fundamental modes of the seven-core fiber are shown on the top, along with an illustration of the fiber endface.

core. The core dimensions correspond to the FIGH-10-350S fiber and the wavelength is 600 nm. Along the length of the fiber, the system oscillates between a state where all the power is in the central core (the initial state) and a state where one-seventh of the power is in each of the outer cores and the central core. The slightly differing behavior between cores in the outer ring, visible in Figure 9-5 at the point where the power in the outer cores is labeled, is a result of the linear polarization of the input field and the six-fold symmetry of the seven-core system. Note that the coupling length, or the distance to the first minimum of the power in the input core, is reduced from that of a two-core system (compare with Figure 9-2(b)), providing further evidence that severe crosstalk is predicted to greatly reduce the practical use of these fibers.

Numerical simulations obviously demonstrate a discrepancy between theoretical predictions of strong crosstalk and the experimentally demonstrated successful image transmission of the image fibers in Table 9-1. Considering the case of only two cores, in order for at least 90% of the propagating power to remain in the initial core, simulations predict that the fiber FIGH-10-500N could be no longer than 10 cm while a length less than 0.5 cm would be necessary for fiber FIGH-10-350S. In addition, the trend demonstrated by Figure 9-5 indicates that this length will decrease when more neighboring cores are considered. Typical flexible endoscopes utilize fibers on the order of a meter long; thus, core coupling or crosstalk should produce detrimental effects on the transmitted images. Yet, experimental results with similar sized fibers [92-94] do not show the significant blurring predicted here. This obvious contradiction between demonstrated fact and numerical results indicates that the simulated system does not accurately represent the fiber used in the lab. As is evident in the images of Figure 9-1, available image fibers are not composed of identical cores. Numerical simulations lead to drastically different conclusions when nonuniformity is introduced into the cross-sections of the simulated multi-core fibers [80, 83].

Numerical analysis

Although both the shape and size of the image fiber cores are quite irregular, only variations in the diameters of adjacent circular cores will be examined here. The effects of other types of nonuniformity, such as core ellipticity and irregular core separation will be briefly discussed later in the chapter. In order to numerically study random variations in the core diameter, each core in a multi-core fiber is randomly assigned a diameter from a Gaussian distribution with an average value of d_o (taken from Table 9-1) and a standard deviation of δd. The degree of nonuniformity in the fiber is quantified by the ratio of the standard deviation to the mean of this distribution ($\delta d/d_o$) times 100, referred to as a percentage of variation. If the average value used for the diameter is 2.0 μm, a variation of 1% indicates a standard deviation of 20 nm. The core separation is the average value from Table 9-1.

Returning first to the simple system of only two cores, asymmetry resulting from random variations in the core diameters will alter the coupling properties of a fiber differently depending on the average size of the cores, the wavelength, and the degree of nonuniformity. In general, both the coupling efficiency and the coupling length decrease in magnitude from their value when the cores are identical. Figure 9-6 shows an example of how the power in each core is altered from that of Figure 9-2(b) when the core diameters of a FIGH-10-350S two-core fiber are no longer equal. Both

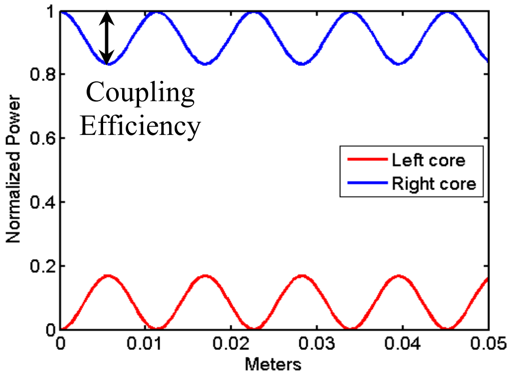

Figure 9-6. The normalized power is plotted versus propagation distance for a FIGH-10-350S two-core fiber with a percentage variation of 1%. λ = 600 nm. The difference in the diameters of the two cores is 16 nm.

types of fibers were analyzed at three different wavelengths, 600 nm, 980 nm and 1300 nm (material dispersion was neglected), for several degrees of variation. Because 100% power transfer may not occur, the coupling length is defined as the distance to the first power minimum of the incident core and the efficiency is the maximum power transferred out of the incident core.

For each randomly generated two-core fiber, the efficiency is plotted versus the coupling length in Figure 9-7. Comparing these plots with those in Figure 8-4 and Figure 8-5, similar trends appear. Notice, however, that the spread in the data is less significant in Figure 9-7, which is most likely a result of the reduced complexity of the variations examined for the step-index fibers. In Figure 9-8, the average coupling efficiency is shown to decrease as the degree of variation increases and as the wavelength decreases for both types of fibers at three different wavelengths. Each marker represents the average efficiency for a set of 99 two-core fibers whose core diameters were randomly assigned from a Gaussian distribution of values. Notice the

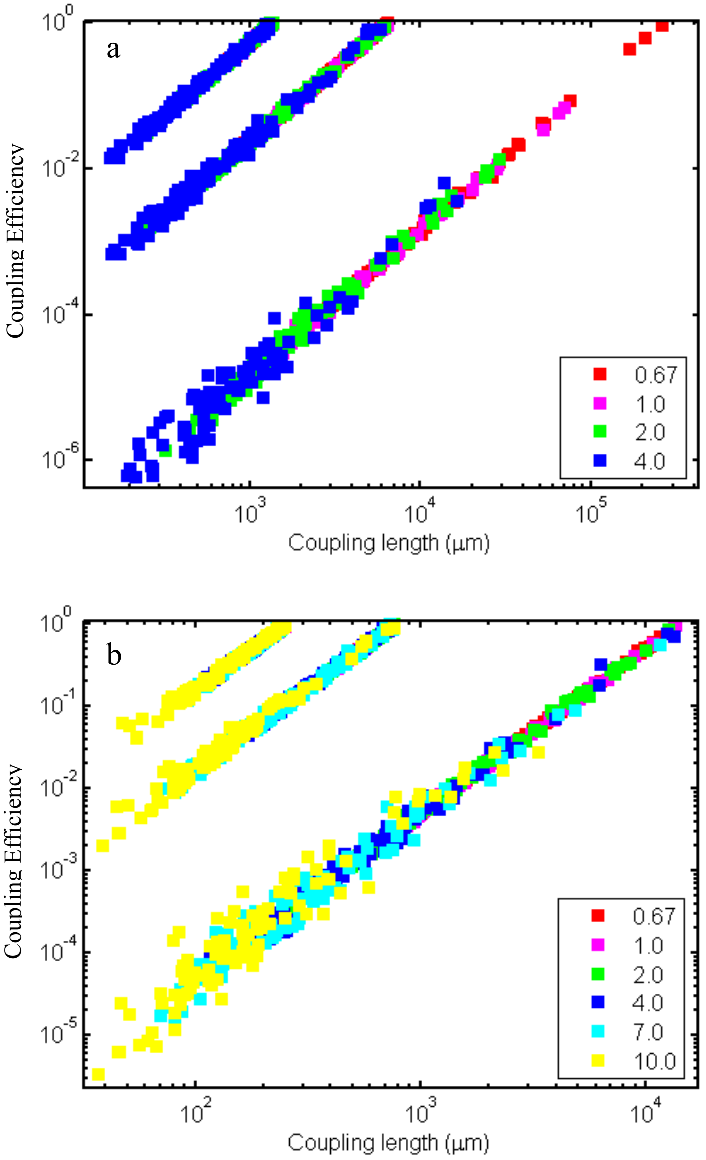

Figure 9-7. Plots of the efficiency versus the coupling length for fiber type 500N (a) and fiber type 350S (b) for λ = 0.60 μm, 0.98 μm and 1.30 μm, with the longest wavelength data in the upper left on each plot. The color of the marker indicates the percentage variation.

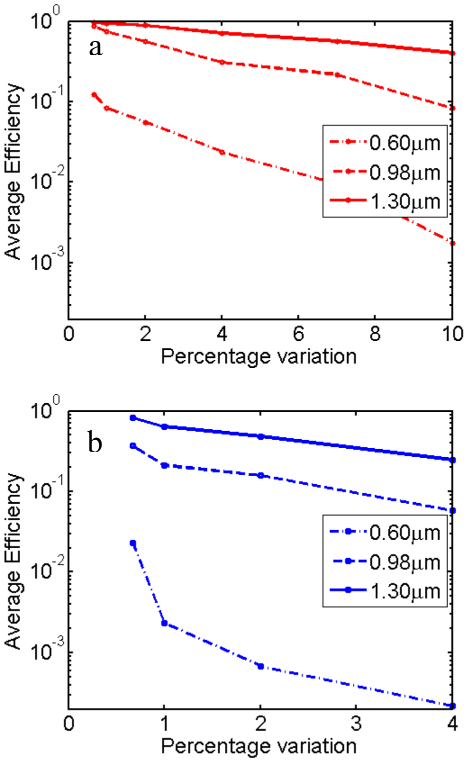

Figure 9-8. The average efficiency for data sets of 99 two-core fibers is plotted versus the percentage variation for a) FIGH-10-350S and b) FIGH-10-500N at three different wavelengths. The lines have been added to more clearly show the trends in the data. Note that the horizontal scales differ.

FIGH-10-500N image fiber is more sensitive to nonuniformity; smaller variations produce a more drastic reduction in the coupling efficiency for the FIGH-10-500N fiber as compared to the FIGH-10-350S type. When the wavelength is 600 nm, a variation of 1% in a FIGH-10-500N fiber results in an average efficiency of approximately 2e-3, indicating essentially independent core propagation or greatly reduced crosstalk. A variation of at least 10% would be needed in the FIGH-10-350S type fiber in order to obtain this same condition. If the coupling efficiency is small, very little power oscillates between the cores of a fiber and the coupling length ceases to be a relevant estimate for crosstalk or the strength of coupling. The introduction of nonuniformities in core size can therefore reduce the crosstalk in cores that would otherwise be strongly coupled.

The conclusions made from studying two-core fibers are applicable to multi-core fibers because they correctly predict the response of larger seven-core systems when the core diameters are no longer equal. For a situation where the diameters of

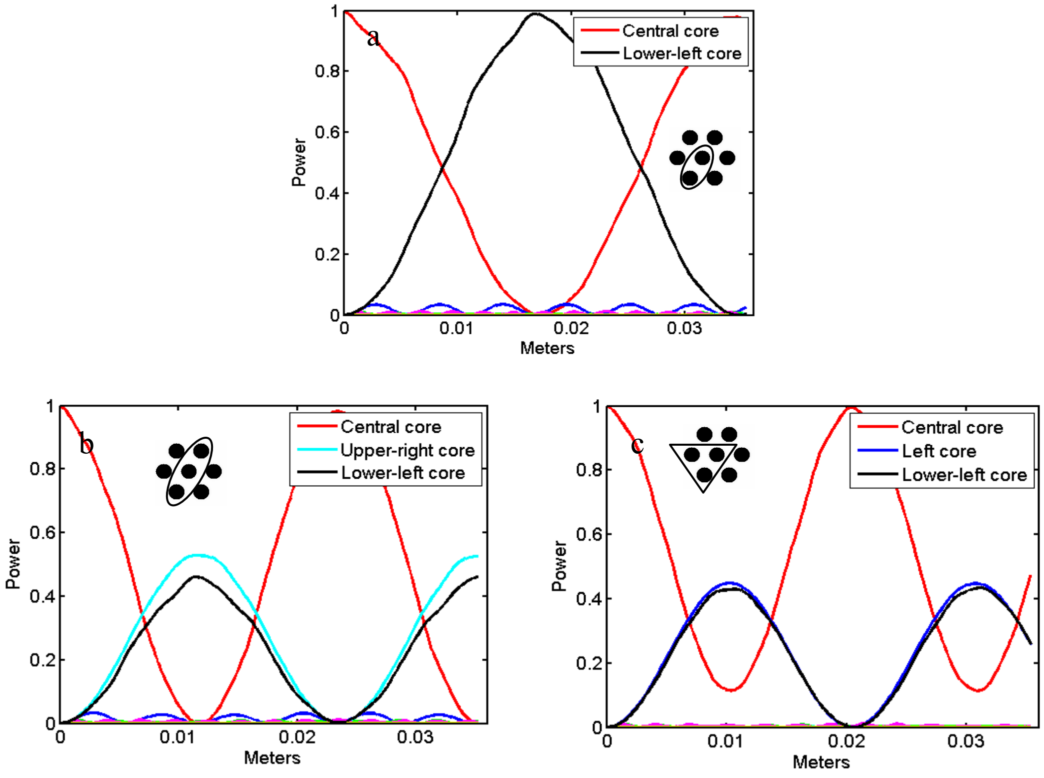

Figure 9-9. Power in a seven-core system when a) one of the outer cores has a similar radius to the central core and when b) and c) two outer cores have a similar diameter to the central core. The insets illustrate which cores are active in the coupling.

seven cores have been randomly selected with a percentage variation of 2% and one outer core happens to have a diameter nearly identical to that of the central core, the power evolution in all seven cores is shown in Figure 9-9(a). The potentially complicated behavior of a seven-core system is essentially reduced to that of a two-core system. The two cores with almost identical diameters—the difference is less than a tenth of a nanometer—transfer power in a manner similar to the two-core system of Figure 9-2, while the remaining cores exhibit behavior similar to Figure 9-6, participating very little in the power exchange. Additional simulations reveal that when the diameter of a second core in the outer ring is forced to match that of the already participating outer core, the system behaves like the respective three-core system, depending on the orientation of the three similar cores, either in a line, Figure 9-9(b), or a triangle, Figure 9-9(c) (compare with Figure 9-3 and Figure 9-4).

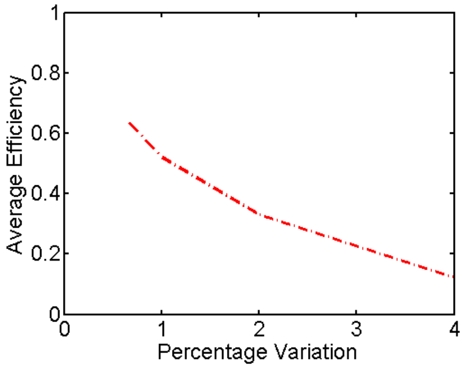

Figure 9-10. The average coupling efficiency of the central core is plotted versus the percentage variation for λ = 600nm. Each marker represents an average over thirty structures and the fiber dimensions are those of FIGH-10-350S.

The average coupling behavior of a seven-core system with randomly varying core diameters is similar to that of the two-core fibers in Figure 9-8. When the diameters of the cores are no longer identical, the maximum amount of power remaining in the central core is, in general, increased. In Figure 9-10, the average coupling efficiency of the central core is plotted versus the percentage variation for type FIGH-10-350S seven-core fibers at λ = 600 nm. Notice that the average efficiency in Figure 9-10, for each degree of variation shown, is approximately six times the corresponding value in Figure 9-8(a) for the same wavelength. Figure 9-8(a), therefore, provides, in the weak coupling regime, an average efficiency for each two-core interaction in a many core system. When a single core is surrounded by six cores, and on average the interactions with each of these cores have a coupling efficiency of 10%, then approximately 60% of the power will oscillate back and forth between the center core and the outer cores while the remaining 40% will be retained in the central core. Obviously, this argument is no longer relevant when the coupling is strong; for fibers with strongly coupled cores, the coupling behavior is similar to that of the symmetric structure in Figure 9-5. Thus, as in the two-core system, a large percentage of variation will increase the power that remains in the input core; however, this amount will be decreased by the interactions with each neighboring core.

A more practical way to view the data in Figure 9-8 and Figure 9-10 is as a function of the diameter difference between the input core and the other cores in the fiber. In this way, the coupling properties of two cores can be related directly to their size mismatch. These relationships are plotted in Figure 9-11 for the same fibers used for the data in Figure 9-8. Each marker represents a different randomly generated

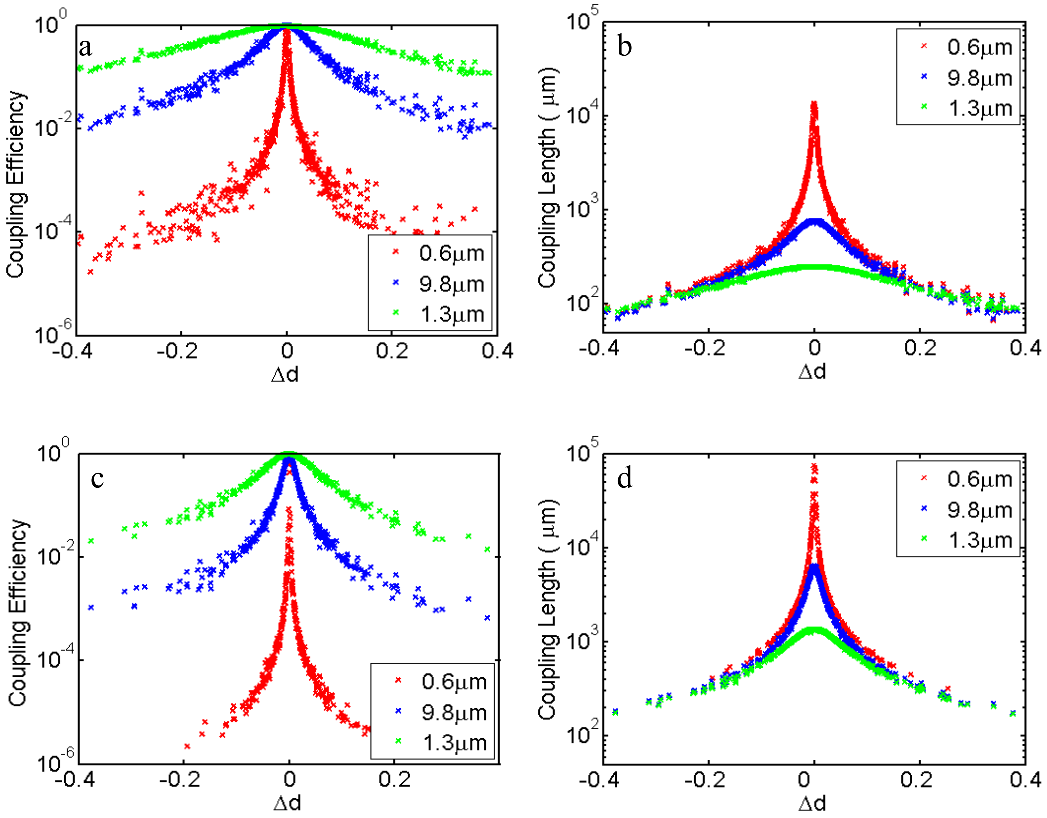

Figure 9-11. The coupling efficiency a),c) and the coupling length b),d) are plotted versus the difference in diameters of the two cores for two fiber types FIGH-10-350S a),b) and FIGH-10-500N c),d). For a percentage variation of 2%, the Δd for a two-core fiber at the standard deviation of the distribution would be 0.04 µm for FIGH-10-350S and 0.058 µm for FIGH-10-500N.

fiber, including all the degrees of variation. As the difference between the diameter of the input core and that of the other core, or Δd, increases, both the coupling length and the efficiency decrease. This decrease occurs more or less quickly depending on the wavelength and the average core size. For example, the efficiency decreases more dramatically at shorter wavelengths and for fiber type FIGH-10-500N, indicating that sensitivity to nonuniformity increases as the wavelength decreases and as the average core size increases. In addition, the coupling length is nearly wavelength independent when the mismatch is large. The spread in the data is due to the fact that the diameters of both cores are varied randomly about an average value; therefore, each Δd does not refer to a unique structure and can be associated with a different coupling length and coupling efficiency.

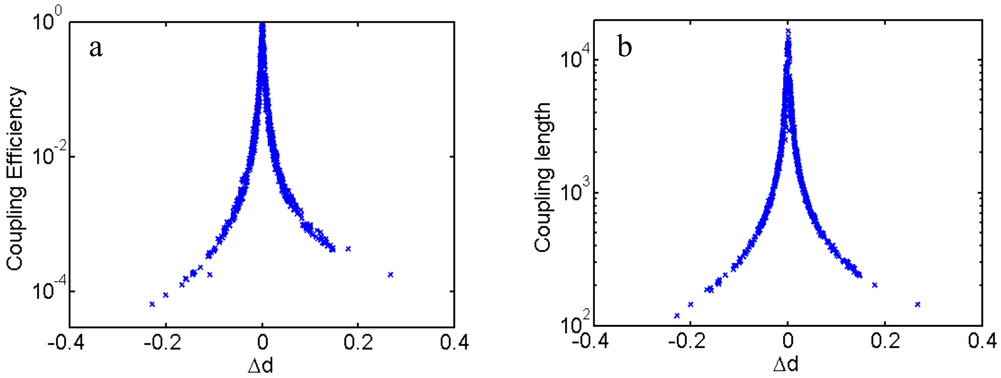

Figure 9-12. The coupling efficiency, a), and the coupling length, b), for the outer cores of a seven-core system plotted versus the difference between the diameter of an outer core and that of the central core. $\lambda = 600$ nm and fiber dimensions match those of FIGH-10-350S. Only fibers with a percentage variation up to 4% are included.

Similar trends appear when the efficiency and the coupling length of each of the outer cores of a seven-core fiber are plotted versus their difference in diameter from the central core, as shown in Figure 9-12 for the 350S fiber at a wavelength of 600 nm. For these fibers, the central core is kept at d_0, the average value, and the diameters of the outer cores are randomly assigned according to a percentage variation of up to 4%, thus reducing the spread in the data points from the two-core data. The close resemblance of Figure 9-11(a) and Figure 9-11(b) to Figure 9-12(a) and Figure 9-12(b) indicate that the behavior of a seven-core fiber can be predicted by studying two-core fibers. Provided an estimate can be made for Δd in a particular fiber, understanding these relationships could lead to a method for predicting the coupling behavior of image fibers with variations.

Coupled mode theory

Coupled mode theory (CMT) is commonly used for obtaining approximate analytical solutions to systems of coupled waveguides, such as multi-core fibers. In CMT, each core is solved for independently and interactions with neighboring cores are treated as a perturbation. For a description of conventional CMT, as used in this chapter, please refer to Chapter 3.

Recall from Eq. (3.12) that the maximum power transferred out of waveguide *a*, or the coupling efficiency, is F^2 and β_d is related to the beat frequency or the rate of power transfer. The coupling length is the distance, L_c, at which the power in waveguide *b* has oscillated to its first maximum, ie. $\beta_d L_c = \pi / 2$. As the mismatch between the modes of the individual cores, β_a-β_b or $\Delta\beta$, increases, these relationships also dictate that the coupling efficiency and the coupling length will decrease, as observed previously.

These expressions for the coupling efficiency and the coupling length can now be applied to the data presented in Figure 9-11. Specifically, the trend in the coupling efficiency in Figure 9-11(a) and Figure 9-11(c) should be described by F^2, or

$$Efficiency = \frac{1}{1+\frac{\Delta\beta^2}{4K_{ab}K_{ba}}} \tag{9.2}$$

and the coupling length is $\pi/(2\beta_d)$ or

$$L_c = \frac{\frac{\pi}{2\sqrt{K_{ab}K_{ba}}}}{\sqrt{1+\frac{\Delta\beta^2}{4K_{ab}K_{ba}}}} \tag{9.3}$$

The mismatch, or $\Delta\beta$, is then considered to be a function of Δd and the product $K_{ab}K_{ba}$ is treated as a constant, which is typically a valid assumption [110]. Because $\Delta\beta$ is determined from the propagation constants of the modes of the individual waveguides, this value can be approximated by calculating β over a range of core diameters for a standard step index fiber [5, 6]. For the degree of variation considered here, β is an approximately linear function of diameter, and $\Delta\beta$ can be written as the slope times Δd. Equations (9.2) and (9.3) are then rewritten as the following:

$$\begin{aligned} Eff &= \frac{1}{1+a(\Delta d)^2} \\ L_c &= \frac{b}{\sqrt{1+a(\Delta d)^2}} \end{aligned} \tag{9.4}$$

where the constant *a* is equal to slope^2/(4$K_{ab}K_{ba}$) and *b* is the coupling length for the system when the two cores are identical. The fitting of Eq. (9.4) to the data in Figure 9-11 is shown for fiber FIGH-10-500N in Figure 9-13.

Table 9-2 displays the product $K_{ab}K_{ba}$ as solved for from the fit parameter *a* for the four plots in Figure 9-11. The values for $K_{ab}K_{ba}$ derived from the two fit parameters in the coupling length plots are approximately equal; therefore, only $K_{ab}K_{ba}$ as derived from the *a* parameter are shown in Table 9-2 for Figure 9-11(b) and Figure 9-11(d). The final column of Table 9-2 gives the value for $K_{ab}K_{ba}$ that is calculated from a two-core system with identical cores by setting Eq. (9.1) equal to Eq. (9.3) for $\Delta\beta = 0$ and solving for $K_{ab}K_{ba}$.

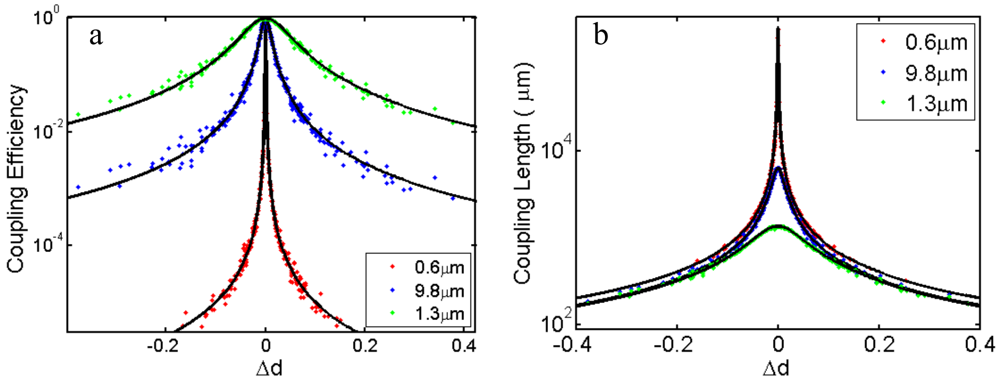

Figure 9-13. Data from Figure 9-11(c) and Figure 9-11(d) replotted and fitted from Eq. (9.4) for fiber FIGH-10-500N. The coupling efficiency is plotted in a) while the coupling length is plotted in b).

Table 9-2. Values for $K_{ab}K_{ba}$ based on the fits of data in Figure 9-11, solved for from the parameter *a*.

FIGH-10-350S			
Wavelength (μm)	Figure 9-11(a)	Figure 9-11(b)	$K_{ab}K_{ba}$
0.6	1.39E-08	1.24E-08	1.29E-08
0.98	4.15E-06	4.22E-06	4.21E-06
1.3	3.72E-05	3.91E-05	3.91E-05
FIGH-10-500N			
Wavelength (μm)	Figure 9-11(c)	Figure 9-11(d)	$K_{ab}K_{ba}$
0.6	3.63E-11	3.34E-11	3.66E-11
0.98	6.03E-08	5.95E-08	5.97E-08
1.3	1.31E-06	1.34E-06	1.32E-06

The values for $K_{ab}K_{ba}$ in Table 9-2 are very similar demonstrating that simple conventional CMT is adequate for predicting the coupling behavior for image fibers with core diameter mismatch and that the product $K_{ab}K_{ba}$ is essentially constant for the degree of nonuniformity studied here. The efficiency of the left core and the efficiency of the right core were also found to be equal to within the error of the program—which is more than two orders of magnitude smaller than the values calculated—further evidence that $K_{ab}{\sim}K_{ba}$. Referreng to Eq. (3.12), the power in core *a* and the power in core *b* have the same amplitude when $(K_{ab}/K_{ba}){\sim}1$, which defines the regime where conventional CMT is valid. In addition, these fits are consistent for the long wavelength data as well, indicating that the expressions in Eqs. (9.2) and (9.3), derived using conventional CMT, retain accuracy even in a stronger coupling regime. Therefore, these equations can be used for predicting the coupling behavior of nonuniform two-core fibers, which we have shown are a good model for multi-core fibers such as fiber bundles.

The quality of images transmitted by an image fiber depends on the amount of crosstalk between cores, or the coupling efficiency; however, because crosstalk can be reduced through the introduction of mismatch between adjacent cores, the performance of a particular fiber depends on the amount of nonuniformity, the wavelength, and the average core size. In order to better understand the interplay of these different parameters and the sensitivity of a particular fiber to core diameter mismatch we compare the two parameters that determine the efficiency, $K_{ab}K_{ba}$ and $\Delta\beta^2/4$, see Eq. (9.2). The relative magnitude of these values determines how sensitive a system is to asymmetry, and also the average amount of crosstalk in a fiber. Because $K_{ab}K_{ba}$ is essentially constant over variations of approximately 10%, it is therefore a property of the symmetric system and can be calculated reliably from Eq. (9.1) for any two-core fiber. The parameter $\Delta\beta$ can be estimated from the degree of nonuniformity in a particular image fiber. If a particular two-core fiber is weakly coupled with a small value for $K_{ab}K_{ba}$, a small $\Delta\beta$ caused from nonuniformities can significantly decrease the coupling efficiency; this fiber would be considered as very sensitive. In Figure 9-14, these two parameters are plotted versus wavelength for the fiber type FIGH-10-350S in (a), and type FIGH-10-500N in Figure 9-14(b). The solid lines indicate $K_{ab}K_{ba}$, as calculated from Eq. (9.1). The non-solid lines are $\Delta\beta^2/4$ for different degrees of asymmetry, where $\Delta\beta = \beta^b(\lambda) - \beta^a(\lambda)$. For simplicity, the core labeled, *a*, maintained a diameter of d_0, the average core diameter given in Table 9-1, while the diameter of core *b* was increased by 1%, 4% and 10%. The propagation constant, β, was calculated over wavelength for each core separately and subtracted in order to obtain $\Delta\beta$.

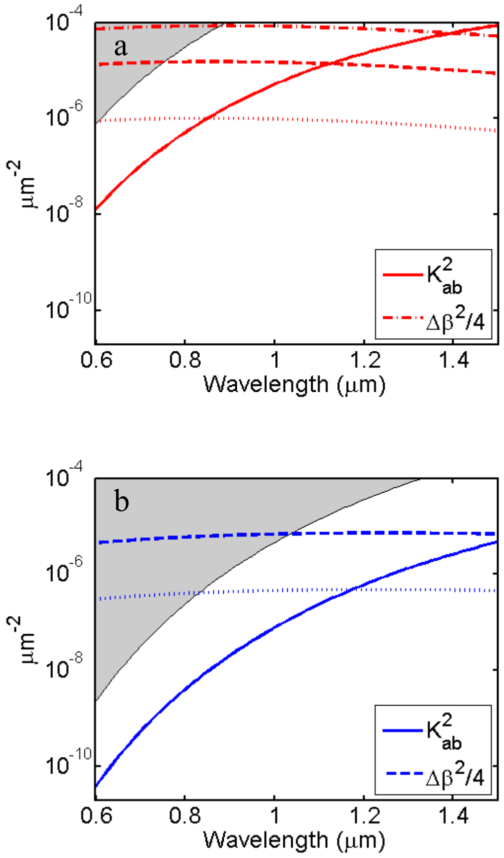

Figure 9-14. $K_{ab}K_{ba}$ is plotted with a solid line and $\Delta\beta^2/4$, as defined in the text, is represented by non-solid lines for different Δd. The dotted lines are for a diameter difference of 1%, the dashed 4%, and dot-dashed 10%. Fiber FIGH-10-350S is shown in (a) while FIGH-10-500N is in (b). When the wavelength and value for Δβ fall in the gray shaded region, the two cores will have less than 1.67% coupling efficiency.

The utility of these plots can be understood by examining, for example, the point where a solid line crosses a non-sold line. At the wavelength of this crossing point, the predicted efficiency, from Eq. (9.2), will be 50%. Above this wavelength, the efficiency will increase and at lower wavelengths it will decrease. As the wavelength and $K_{ab}K_{ba}$ decrease, a fiber becomes more sensitive to nonuniformities, approaching a region of independent core propagation. For example, when the wavelength and value for $\Delta\beta$ fall in the gray shaded region, the two cores will have less than 1.67% coupling efficiency. For the opposite trend in wavelength and $K_{ab}K_{ba}$, a fiber enters a strongly coupled regime where reducing crosstalk becomes more and more difficult. Notice also that fiber type FIGH-10-500N has a larger wavelength range with low efficiency coupling demonstrating again that this fiber is more sensitive to nonuniformity. Due to the scale invariance of Maxwell's equations, the results in Figure 9-14 can be applied to situations not within the range shown and to fibers of different core sizes, if the wavelength and fiber dimensions are scaled appropriately. These plots can also be generated for any two-core fiber given a step-index fiber mode solver and the average coupling length when the cores are identical.

Discussion

The dramatic impact of nonuniformity on the coupling properties of multi-core fibers can be understood more intuitively by examining the changes that occur in the modal fields when variation in core size is present. When the core diameters of a seven-core fiber differ significantly, the modes of the multi-core system decouple into those of the individual cores. The existence of localized modes in a disordered waveguide system such as a fiber bundle has also been observed by others [111].

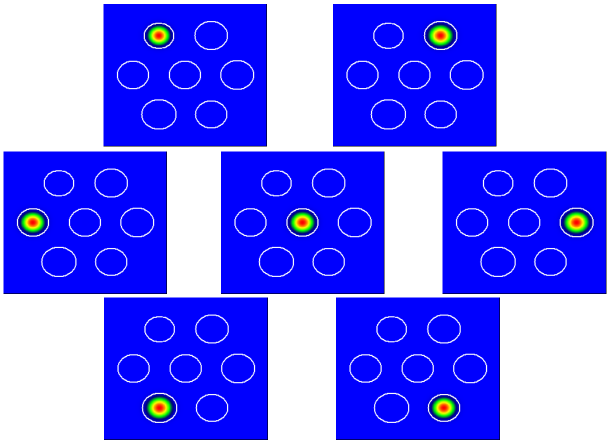

Figure 9-15. The decoupled modes of a seven-core system with a percentage variation in core diameters of 4% and dimensions of FIGH-10-350S, $\lambda = 600$ nm.

Figure 9-15 shows the seven unique energy distributions of the fourteen nondegenerate modes of a decoupled seven-core system, which can be compared to the modes of the identical core fiber shown in Figure 9-5. Light incident on a single core of the fiber in Figure 9-15 will couple almost completely into just one mode of the system and therefore not mix with other cores or modes along the length of the fiber. The field expansion will contain essentially one mode and the energy distribution is no longer a strong function of z. The cores of this image fiber behave independently of their neighbors because differing adjacent core diameters have created a mode mismatch that will inhibit coupling.

In addition to variations in size, the cores of image fibers also vary in shape and separation. The impact of these nonuniformities can be estimated to be less than that of variation in core size. The increase in $\Delta\beta$ caused by core ellipticity can be estimated from studies on the geometric birefringence of elliptical core fibers [112-114]. For example, if the variation in core diameter is 10%, a maximum birefringence can be estimated by defining the major and minor axes of an elliptical core as 10% more and 10% less than the average core diameter, resulting in an ellipticity of approximately 0.182. This shape distortion would cause a $\Delta\beta$ on the order of 10^{-4} [112-114]. Comparing the square of this value to the non-solid lines in Figure 9-14, it is evident that ignoring the effect of nonuniformity in core shape is appropriate due to the relatively small size of this parameter compared to the $\Delta\beta$ caused by variation in the core diameters. Ellipticity results in a minimal amount of mode mismatch because the overall core area is not altered as dramatically as when the core radius is changed; the propagation constant is affected more by a change in the modal area than by a change in the modal shape. Irregularity in the core spacing will affect the coupling length rather than the coupling efficiency when the core diameters are the same. For non-identical cores, changing the separation will make the two-core system more or less sensitive to core diameter mismatch, depending on whether the cores become closer or farther apart. Because an increase in the core separation has the opposite consequence from decreasing the core separation, the net effect on a fiber with thousands of cores is expected to be small. Core diameter mismatch is, therefore, the dominant effect in these multi-core fibers.

Our numerical and analytical assessments of multi-core fibers provide a method for analyzing the crosstalk in a particular fiber bundle. The plots of Figure 9-14, based on the parameters in Eq. (9.2), can be used to estimate the coupling efficiency of two core interactions given a certain degree of nonuniformity. Based on arguments present in this paper, this two-core analysis can be applied to cores with six neighboring cores. In this manner, the reliability of a pixel in an image fiber can be estimated give a certain acceptable amount of crosstalk and an average degree of nonuniformity. For example, if the pixel size of the FIGH-10-350S fiber type is preferred for an experiment, yet a coupling efficiency of no more than 0.1 can be tolerated at $\lambda = 780$ nm—in other words, 90% of the signal power is expected to be retained in each core—the average coupling efficiency for each core pair should then be approximately 0.0167, when six near neighbor interactions are considered. The value for $\Delta\beta$ that would produce this efficiency would need to be at least sixty times larger than $K_{ab}K_{ba}$ (using Eq. (9.2)); the shaded region in Figure 9-14 indicates the values for $\Delta\beta$ that satisfy this condition. Referring to Figure 9-14, a diameter difference of at least 4% would result in a difference of this order of magnitude. Since this type of image fiber has approximately a 10% variation in core diameter, as measured by SEM (Table 9-1), and given a Gaussian distribution, there is a 70% chance that two cores will have a diameter difference of exactly 4% or higher. Therefore, approximately 30% of the pixels will be limited by crosstalk given this situation and tolerance. Due to the higher sensitively of the FIGH-10-500N fiber, better performance would be anticipated given the same efficiency restrictions.

This example illustrates the fact that the coupling will typically not be reduced below a desired limit in one hundred percent of the cores in an image fiber; some degree of error is inevitable. Table 9-3 provides an estimate of the pixel accuracy of the two fibers studied given two different values for the total percentage of power coupled out of the input core that can be tolerated in an experiment. The estimates also assume the fiber exhibits 10% variation in the core size and that the wavelength is 780 nm. A percentage of 95% indicates that around 500 of the total ten thousand cores will exhibit stronger coupling than desired. In fact, strong core coupling in these image fibers has been demonstrated experimentally and is described in Chapter 10.

These effects will be manifested as an overall reduction in the image resolution and the reliability of each pixel value.

Table 9-3. Pixel accuracy based on 10% variation in pixel diameter.

Total coupling efficiency tolerance	FIGH-10-350S	FIGH-10-500N
10%	70%	95%
50%	85%	99%

Conclusion

Theory and simulation indicate that due to the small core size and separation of current image fibers, crosstalk between pixels should make the transmission of images through flexible endoscopes severely blurred. However, nonuniformity in the core size is shown to reduce the efficiency of the coupling between adjacent cores, substantially suppressing this crosstalk. The manufacture of functional image fibers with closer and smaller pixels requires the pixels to be nonuniform in order to enhance mismatch between neighboring cores. The degree to which two cores will interact or couple depends on the wavelength, the degree of variation, and the average core size. Coupled mode theory was used to generate expressions that can predict the amount of nonuniformity that will reduce crosstalk to acceptable levels in addition to assessing the pixel reliability of available image fibers.

The work presented in this chapter has been submitted for publication in the Optics Express journal and appears in the abstracts of the Biophysical Society's 50th Annual Meeting [115].

Chapter 10

ANALYSIS AND MEASUREMENT OF LIGHT PROPAGATION IN COHERENT FIBER BUNDLES

Introduction

In Chapter 9, it was stated that image fibers, or coherent fiber bundles, are able to transmit images as a result of nonuniformity in the cross-section that reduces core coupling. Due to the random nature of this effect, however, strong core coupling can still be observed. In this chapter, we experimentally demonstrate strong coupling in fiber bundles typically used for endoscopic imaging. This coupling depends on the wavelength as well as on the polarization of the input light. These results indicate that the performance of currently available image fibers, and therefore the quality of images transmitted, is still compromised by crosstalk.

Theory

A summary of the numerical results presented in Chapter 9 is given in Figure 10-1 for a two-core 350S fiber at a wavelength of 780 nm, which is near the wavelengths used in the experiments of this chapter. Figure 10-1 compares a two-core

350S fiber with identical cores to a 350S fiber with the diameter of one core increased by 2% (40 nm). The modes of the symmetric fiber are the familiar even and odd modes of a coupled oscillator with equal energy distribution between each core, see Figure 10-1(a) and Figure 10-1(b). When the two cores are identical, an input into one core will be completely transferred to the second core after propagating a distance referred to as the coupling length, Figure 10-1(c). When the wavelength is 780 nm, the coupling length for fiber type 500N is 3 cm, and for type 350S this distance is only

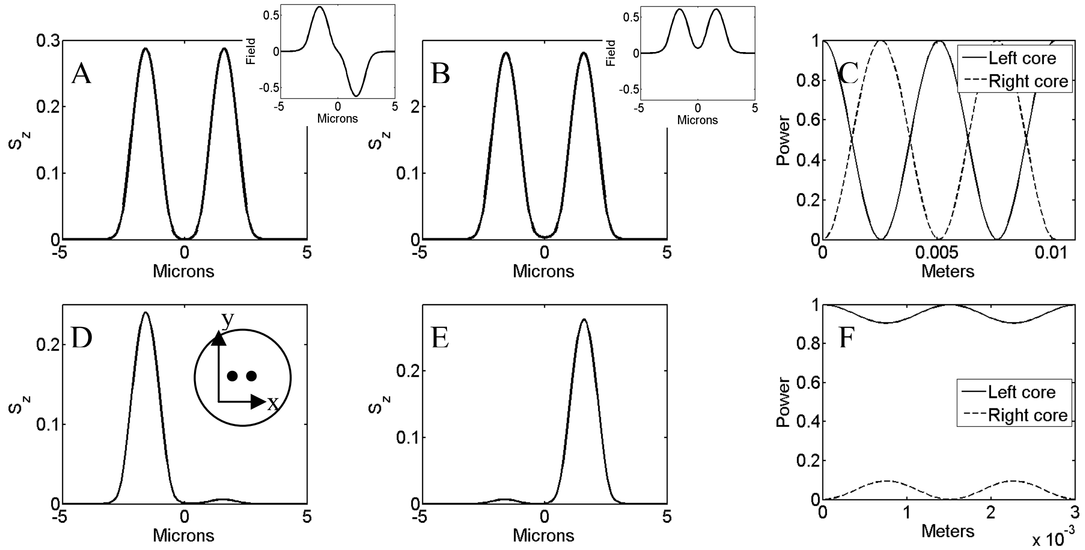

Figure 10-1. Fiber type 350S for a symmetric two-core fiber (a-c) and a two-core fiber with one core diameter increased by 2% (d-f), wavelength = 780nm. Plots a,b,d,e display the z-component of the Poynting vector for the two x-polarized modes. The insets of a) and b) show the characteristic odd/even behavior of the modal fields. The power is plotted versus the propagation distance in c) and f) for an x-polarized input into the left core. The inset of d) shows a two-core fiber cross-section.

2.5 mm. The asymmetric fiber is characterized by modes that resemble the independent individual cores, Figure 1(d) and 1(e). Because the cores become decoupled, a single core input very closely overlaps with a mode of the system such that only a small amount of the power oscillates as a function of the propagation distance, Figure 1(f). For the asymmetric fiber, light incident initially on a single core will remain mostly in that core as it propagates down the fiber. As a result of this effect, image fibers with closely packed cores can transmit an image without severe blurring.

All numerical simulations in this chapter are based on methods presented in previous chapters.

Experimental methods

Because variations in the image fiber cross-section are random in nature, strong coupling between adjacent cores is still possible and can be readily observed in the image fibers we experimentally tested. The experimental set-up is illustrated in Figure 10-2 and pictures of the actual set-up appear in Figure 10-3. A tunable diode laser (EOSI 2010, linewidth of approximately 1e-5 nm) was made into a fiber source by coupling the light into a single mode fiber patch cord. In this manner, drift in the laser beam caused by tuning of the wavelength or change in temperature altered only the power output and not the final beam position or spatial profile. The single mode fiber output was then collimated and focused onto the fiber bundle using an objective that matched the NA of the image fiber (NA = 0.30), such that the spot size was approximately the size of an individual core or pixel. This objective was replaced with a low NA objective (NA = 0.10) for some data collection to try to reduce the multi-moded nature of the fiber cores. Because these results tended to have a larger number of participating cores, due to the larger spot size, the observations of coupling were not as clean; therefore, the 0.30 NA objective that matched the NA of the fiber core was preferred.

A nonpolarizing beam cube was added to the set-up between the patch cord collimator and objective two in order to monitor the wavelength and power of the incident light. The power readings were not used in the final processing of the images although the data was helpful for assessing the stability of the laser. The value for the wavelength was recorded using an optical spectrum analyzer with a resolution of 0.01 nm. The light transmitted through the fiber bundle was imaged onto a CCD camera through an old microscope tube using a 100x objective. A white light source for reflected light imaging was also present in the set-up at this end of the image fiber in

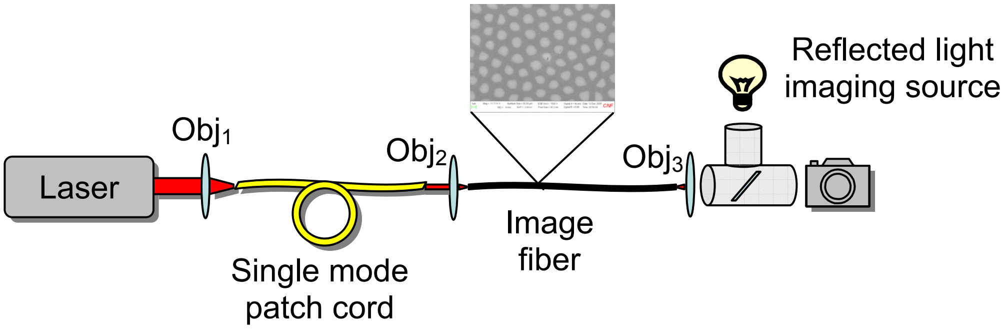

Figure 10-2. Experimental set-up: Obj$_1$ is an objective with NA = 0.10, Obj$_2$ serves as a collimator and an objective with NA = 0.30, Obj$_3$ is a 100x objective. The image inset is an SEM micrograph of a fiber bundle endface.

order to facilitate alignment of the set-up and to observe the fiber endface. Images were collected using a PixelSmart framegrabber and captured using an ImageJ program.

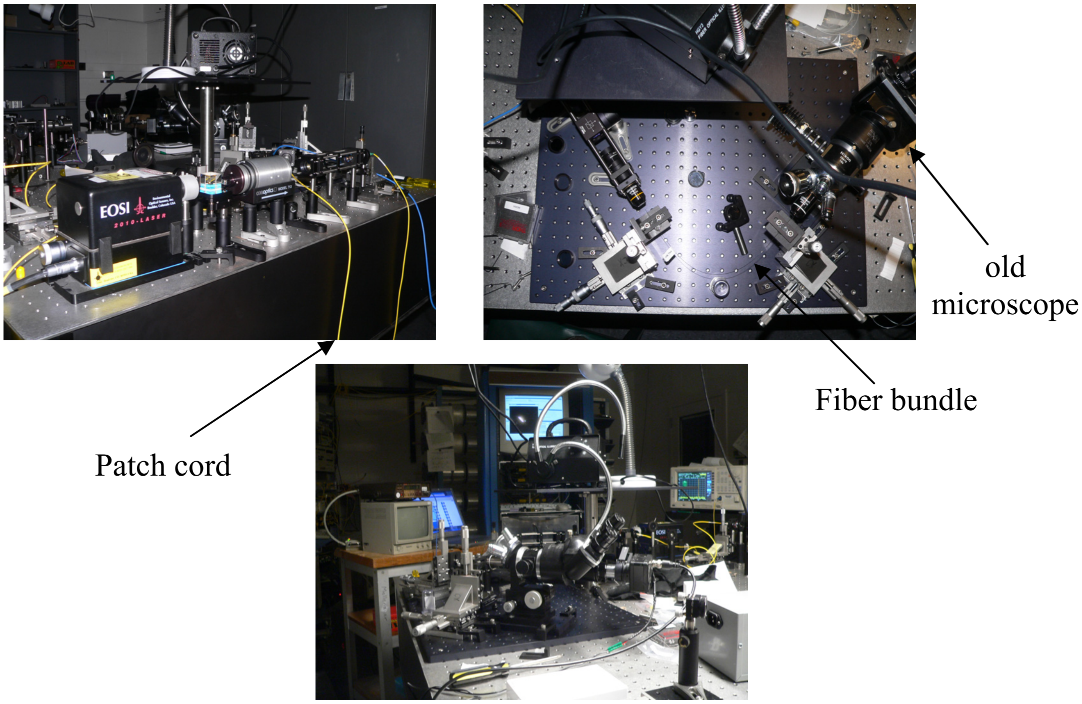

Figure 10-3. Photographs of the experimental set-up in the lab.

The input coupling conditions were then held constant as the image fiber output was analyzed over changes in laser wavelength and polarization. When a single core of the image fiber is illuminated, the fiber output shows a distribution of power among multiple cores, evidence that coupling is occurring. To examine the wavelength dependence of coupling, a new image was captured for each change in the input wavelength and images were taken over a range of wavelengths. Several image fibers where examined and results were typically collected from multiple areas on the fiber endface.

We observed strong core coupling in both the 350S and 500N Fujikura image fibers in addition to Sumitomo image fibers IGN-02-03 and IGN-035-06. The details of the Fujikura fibers have been stated previously in Chapter 9. Sumitomo fiber IGN-02-03 is similar to the 350S Fujikura fiber although with slightly smaller dimensions; the core separation is estimated to be approximately 3 μm and the core diameters between 1.5 μm and 2 μm. The length of the fiber sample used in the experiment was 0.9 m. The Sumitomo fiber IGN-035-06 is similar to the Fujikura 500N fiber with core separation of 4 μm and core size of approximately 2.5 μm; a length of 0.5 m was used. The Sumitomo fibers show a similar degree of variation in core size and shape to the Fujikura fibers, as observed from SEM images. An image taken of the IGN-02-03 fiber endface is shown in Figure 10-4. A Schott leached fiber bundle was also analyzed experimentally. The cores of this fiber are highly uniform and very large with diameters of 7 to 8 μm. Due to the tight mode confinement, coupling between neighboring cores is not expected and was not observed unless the power in the input core extremely saturated the camera. It is estimated that the percentage of power coupled between cores is reliably insignificant throughout the cross-section of these fibers. The exact indices of refraction of the Sumitomo and Schott fibers were not provided by the suppliers although the NA of the Sumitomo fibers is about the same as that of the Fujikura fibers.

An example of typical experimental results is shown in Figure 10-5 for the Fujikura 350S fiber. Three images taken at different wavelengths are shown in Figure 10-5(1-3). These images demonstrate that the power distribution in different cores changes with the wavelength. The fourth image is taken with a femtosecond

Ti:Sapphire laser (Spectra-Physics), with a spectral bandwidth covering the entire tuning range indicated in Figure 10-5(4). We found that, in general, the images taken with the pulsed source are comparable to the sum of individual images taken using the narrow band diode laser at each wavelength within the pulse spectral bandwidth.

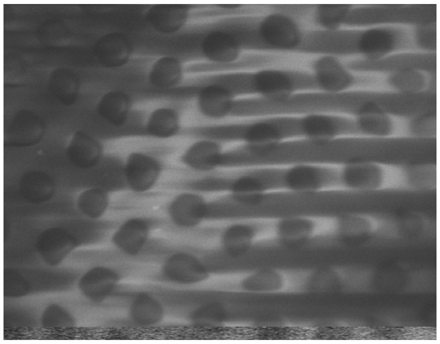

Figure 10-4. SEM micrograph of the Sumitomo IGN-02-03 fiber.

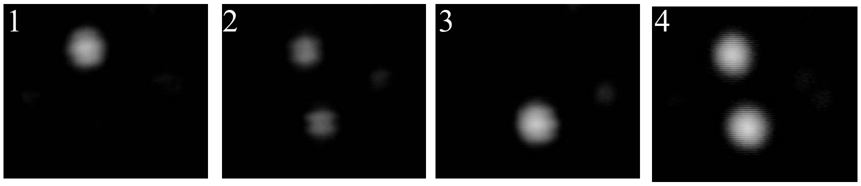

783.05 nm 783.25 nm 783.45 nm 777.5 to 786 nm

Figure 10-5. Images 1-4 are of the transmitted light through the image fiber 350S at different wavelengths; the images are approximately 7 μm square. The source for images 1-3 is CW while in image 4 the source is broad band and containing the wavelengths indicated.

Two examples of experimentally obtained plots of the power versus the wavelength are shown in Figure 10-6(b) and Figure 10-7(b) for each type of fiber. The power in a particular core was determined from each images by summing over the pixel values in a particular core area and dividing by the sum for the entire image. This processing was performed in Matlab. The wavelength dependence of the power in each core demonstrates the wavelength dependence of the coupling length. The period of power oscillations is indicative of the coupling length, which is shorter for the 350S fiber (see the direct comparison in Figure 10-8); thus, a smaller change in wavelength results in a more drastic change in the power distribution. Oscillations are observed because changing the wavelength has a similar effect to changing the length of the fiber for a single wavelength.

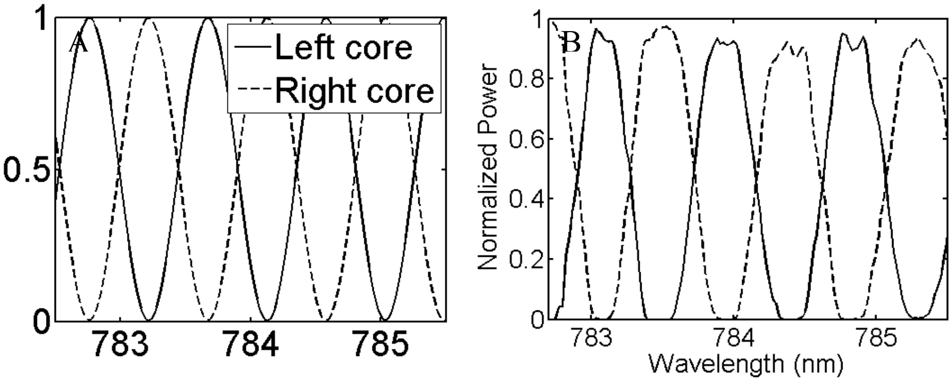

Figure 10-6. Numerical, a) and experimental, b) results for the power in two cores as a function of wavelength for fiber type 350S. The numerical results are calculated at a propagation distance of z = 0.3 m.

Because these power plots show the total power in each core oscillating, approximately, between zero and one, it is apparent that the coupling observed is occurring predominantly between two participating cores. In addition, because nearly one hundred percent power transfer is occurring between the cores, these plots suggest that the two cores shown are of nearly identical size while their neighboring cores have enough size mismatch to be decoupled from the two participating cores.

In order to demonstrate that the previously described theoretical analysis of multi-core fibers is applicable to actual image fibers, the experimental results in

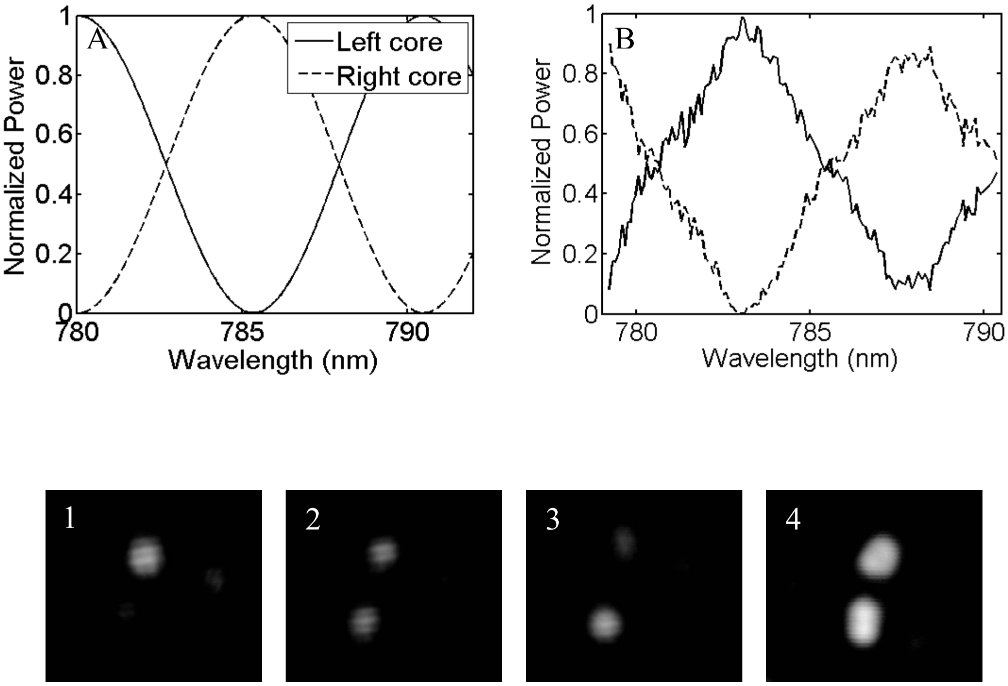

779 nm 781 nm 783 nm 778 to 789 nm

Figure 10-7. Numerical, a), and experimental, b), results for the power in two cores as a function of wavelength for fiber type 500N. The numerical results are calculated at a propagation distance of z = 0.3 m. The images are of the transmitted light through the image fiber 500N at different wavelengths. The source for images 1-3 is CW while in image 4 the source is broad band and containing the wavelengths indicated.

Figure 10-6(b) and Figure 10-7(b) were duplicated through simulations. The modes of two-core fibers with identical cores were calculated over a range of wavelengths and a normal mode expansion was used to calculate the power at a distance approximately equal to the sample length of the actual fibers, 0.3 m. The power in each core at this propagation distance was then plotted against the wavelength. The simulated plots approximately match the periodicity of the experimental data and are shown in Figure 10-6(a) and Figure 10-7(a). The core size and separation for these plots are 2.8 μm and 2.1 μm for Figure 10-6(a), and 4.2 μm and 2.84 μm for Figure 10-7(a). The fact that these parameters do not match the average values for each type of fiber is not surprising given the amount of variation present in the fiber cross-section.

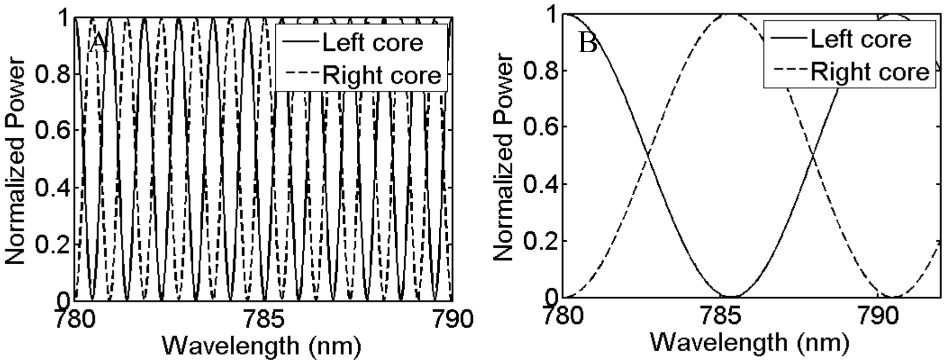

Figure 10-8. Comparison of the numerical simulations matching the experimental data in Figure 10-6 and Figure 10-7 over approximately the same wavelength range, demonstrating the different coupling behavior in these two fibers. The numerical results are calculated at a propagation distance of z = 0.3 m.

In Figure 10-7(1-4), the actual images from different wavelengths are presented for the Fujikura 500N fiber from the data in Figure 10-7(b). The shape of the transmitted light in image 4 indicates that a higher order mode has been excited in this fiber. This double-lobed shape is similar to a linear polarized (LP) mode of a standard single mode fiber. Coupling between higher order modes was observed in other experimental results shown later in the chapter and is not surprising considering the large core size of the 500N fiber.

In order to experimentally assess the polarization dependence of the coupling, the polarization of the input light is rotated by inserting a half-wave plate in the beam path. The patch cord was also securely taped to the table in order to reduce movement of the fiber which could alter the polarization of the output light. Figure 10-9(a) and Figure 10-9(b) show the simulation and experimental data, respectively for fiber type 350S. The experimental data is processed in the same manner as previously stated and the simulation plot is produced by calculating the power at the end of the fiber using a normal mode expansion while rotating the input polarization for a single wavelength. The oscillating power in each of the two cores indicates that the coupling depends on

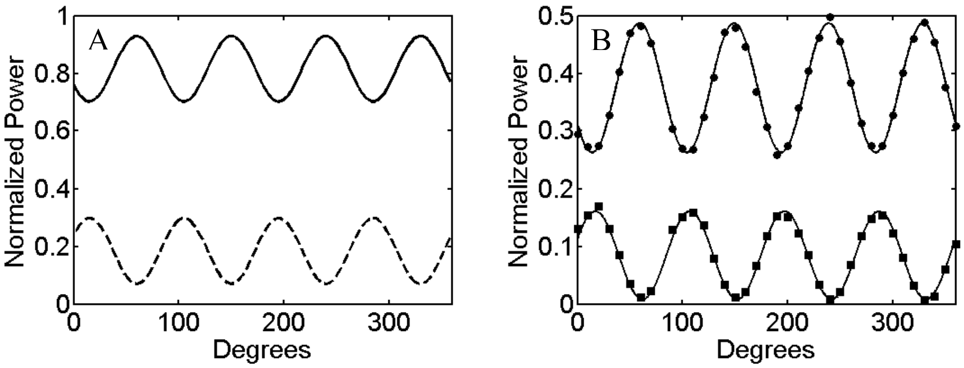

Figure 10-9. The numerical (a) and experimental (b) results for the power in two cores of fiber 350S when a half-wave plate is rotated 360 degrees.

the input polarization state. The experimental data in Figure 10-9 has been fit to a sine-squared function with a period of 90 degrees. The frequency of oscillations in the observed power matches the expected cycle necessary for a complete rotation of the polarization.

Additional experimental results, such as raw images and power plots, are presented in Figure 10-10 through Figure 10-16, including observations of coupling in the Sumitomo fibers. Although the coupling between cores of an image fiber is demonstrated very clearly in the data of Figure 10-6 and Figure 10-7, these additional plots and images lend further insight into the behavior of the coupling in fiber bundles and the proper way to observe it.

The data in Figure 10-10 and Figure 10-11 were taken with a low NA objective for coupling light into the fiber bundle, as previously alluded to in the description of

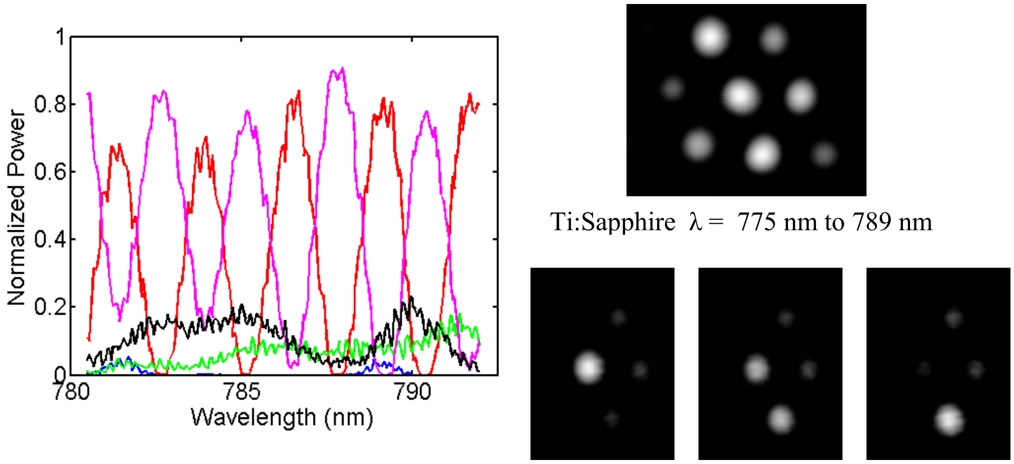

Ti:Sapphire λ = 775 nm to 789 nm

λ = 786.68 nm, λ = 787.12 nm, λ = 787.56 nm

Figure 10-10. A small NA objective (0.10) was used to couple light into the fiber bundle; therefore, more cores a participating in the coupling. The fiber is FIGH-10-350S. (Run3, 7-24)

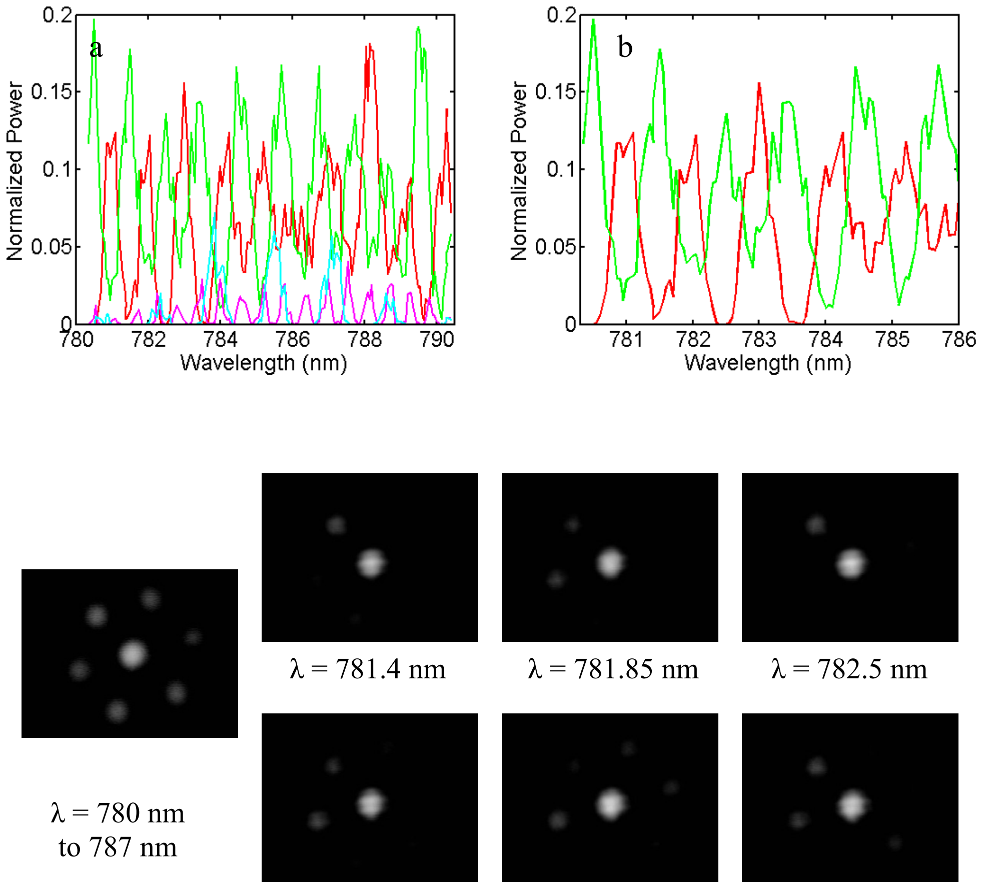

λ = 780 nm
to 787 nm

λ = 781.4 nm

λ = 781.85 nm

λ = 782.5 nm

λ = 782.95 nm

λ = 784.0 nm

λ = 784.35 nm

Figure 10-11. A 0.10 NA objective was used to couple light into the fiber. Notice the large number of cores participating in rather complicated coupling behavior, a), most likely due to the large spot size. Plot b) shows two of the cores in a) for a shorter range of wavelengths in order to better observe the symmetric behavior of these two cores. Notice that this coupling behavior is occurring between the two cores to the left of the central bright core which is providing a background illumination. The fiber is FIGH-10-350S. (Run 1, 7-26) the laser set-up. These observations typically show complicated coupling behavior between several cores due to the fact that multiple cores were illuminated by the input light and these cores coupled differently into various neighboring cores. In Figure 10-10, several cores participated in the coupling although two cores appear more strongly coupled to one another. Likewise, several cores are participating in the coupling in Figure 10-11. Although the power transfer appears complicated, two of the cores, in Figure 10-11(b), demonstrate complimentary behavior and these two

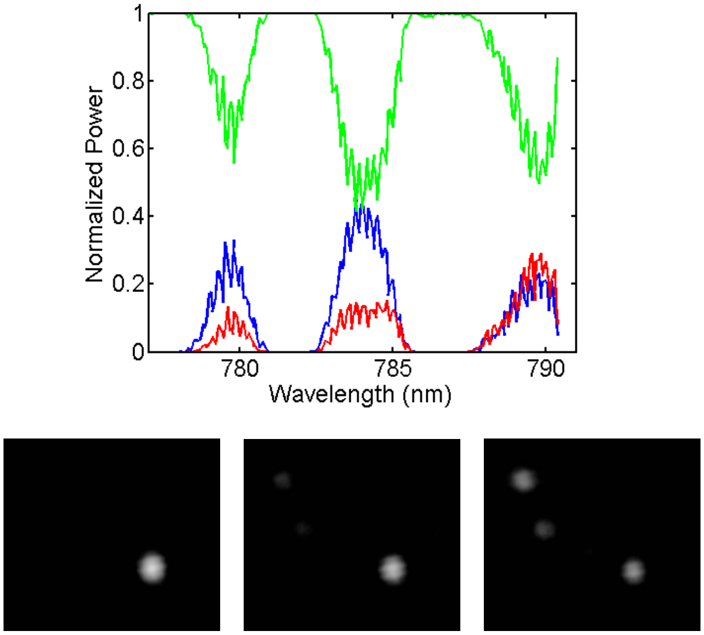

λ = 781nm λ = 782.9 nm λ = 784 nm

Figure 10-12. The fiber is FIGH-10-350S and the NA of the coupling objective is 0.30. (Run 3, 7-26).

are peripheral cores to the brightest central core, as shown in the images of Figure 10-11. The bright, central core provides a background illumination such that the total power on the plot is not equal to one. A finer step size might have reduced the complexity of the oscillations but the large number of interacting cores can be attributed to the large spot size, a result of using a smaller NA objective. It is also interesting to compare the images shown at individual wavelength steps to the Ti:Sapphire image including a range of wavelengths, which closely resembles the sum of the images.

Figure 10-12 and Figure 10-13 demonstrate incomplete coupling, when the coupling efficiency is less than one hundred percent. This occurs when two cores are non-identical but have only a slight mismatch to each other when compared to mismatch with neighboring cores. Figure 10-12 provides an example of significant power transfer occurring between next-nearest neighbor cores. Figure 10-13 shows very strong agreement between the Ti:Sapphire image and the single wavelength

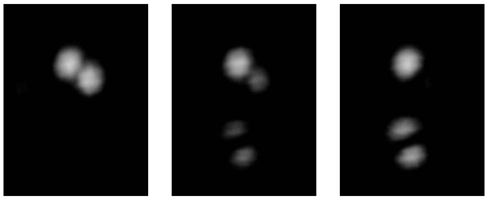

λ = 784.88 nm, 785.25 nm, 785.64 nm

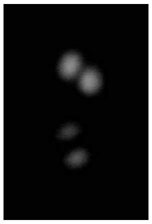

Ti:Sapphire
λ = 780 nm to
790 nm

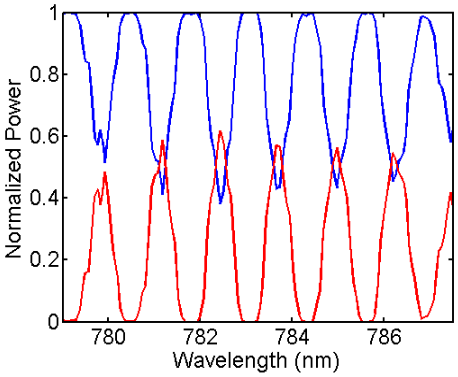

Figure 10-13. The fiber is FIGH-10-500N. (Run1, 7-31)

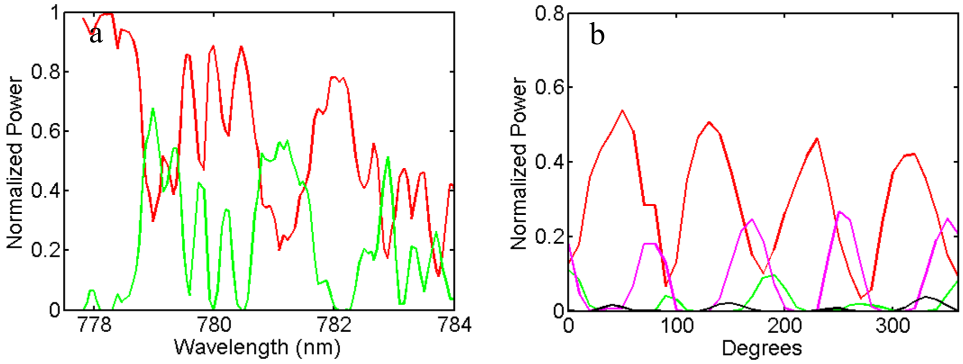

Figure 10-14. The polarization is rotated in b) and the wavelength varied in a). The input conditions are identical for both plots. The fiber is IGN-02-03 and the NA of the coupling objective is 0.30. (Run2 and Run3, 7-31)

images. In addition, the coupling is again between higher order modes in this 500N fiber.

In Figure 10-14 through Figure 10-16, the fibers used are manufactured by Sumitomo and the model number is indicated in the figure caption. In general, both of these fibers tended to exhibit complicated coupling behavior among several different cores and strong coupling between only a pair of cores was difficult to observe. In Figure 10-14 and Figure 10-15, the polarization dependence of the coupling is also shown. These plots clearly show the 90 degree period oscillations in several participating cores. Although the coupling behavior in Figure 10-13 and Figure 10-14 is complicated, two of the cores mirror each other. In Figure 10-16, coupling between next-near neighbors is again shown to be significant. These results show that the Sumitomo fibers also exhibit coupling that is a function of the wavelength and the

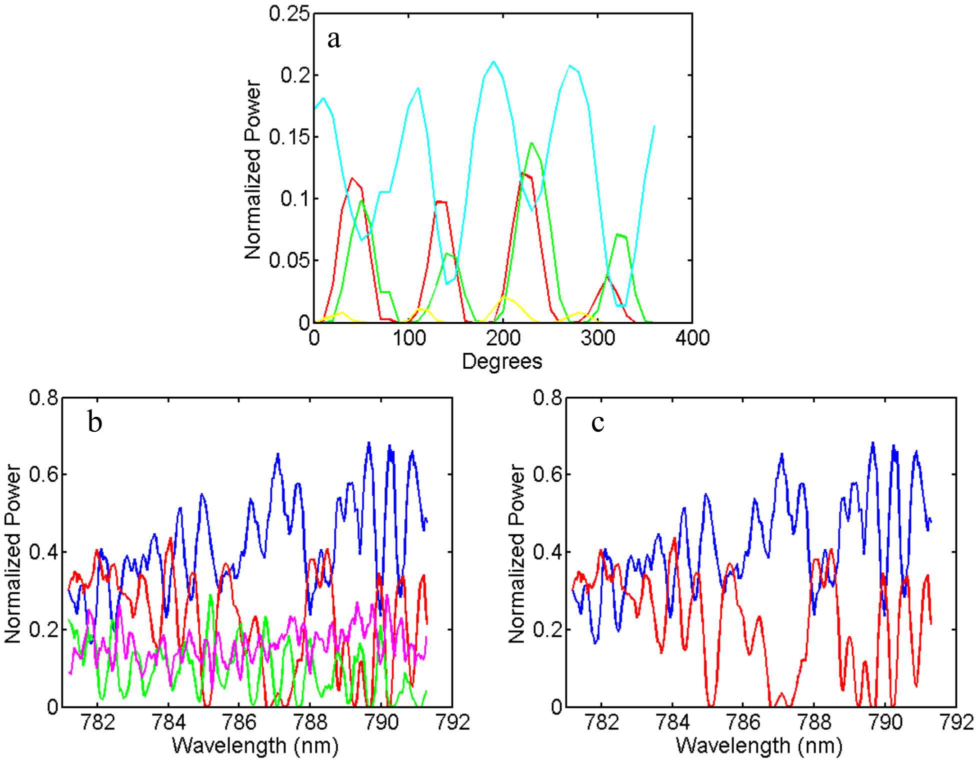

Figure 10-15. The polarization is rotated in a) and the wavelength varied in b) and c). The input conditions are identical for all plots. Plot c) shows only two of the cores in b) in order to better observe the symmetric behavior of these two cores. The fiber is IGN-02-03 and the coupling objective NA is 0.30. (Run4 and Run5, 7-31)

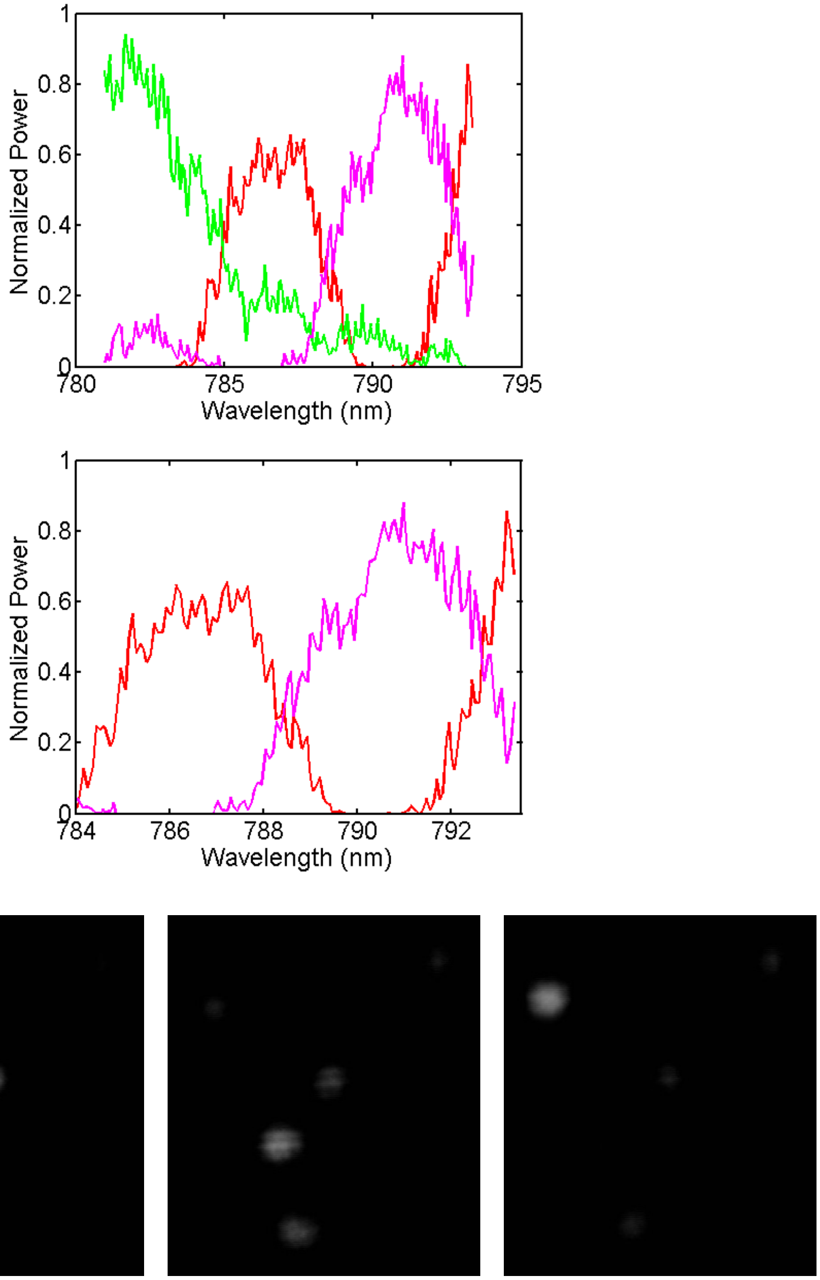

λ = 782.6 nm λ = 787.0 nm λ = 790.8 nm

Figure 10-16. Above are power plots showing the three cores participating the most in the coupling over different wavelength ranges. The fiber is IGN-035-36 and the coupling objective NA is 0.30. (Run2, 8-2) polarization and that this coupling tends to involve more cores than the coupling in the Fujikura fibers.

Conclusion

We have shown that core coupling that is a function of the wavelength and the polarization can be experimentally observed in Fujikura and Sumitomo image fibers. In general, the coupling behavior involved more cores in the Sumitomo fibers, whereas strong coupling between only a pair of cores was more easily observed in the Fujikura fibers. This may be evidence that the nonuniformity in the Fujikura fibers is more effectively reducing the coupling than in the Sumitomo fibers. From these observations, we would predict that Fujikura fibers will produce higher quality images than Sumitomo fibers of similar dimensions. In some plots of the power versus the wavelength, fairly complicated energy transfer was observed; the inclusion of more data points could possibly have improved this data. The coupling length in these examples appears to be very short, such that small wavelength steps would result in significant change. In this case, the behavior is not accurately represented by such coarse wavelength scanning.

Furthermore, our experimental results and numerical simulations of the wavelength and polarization dependence of crosstalk indicate that the coupling between cores in an image fiber can be predicted by modeling light propagation in coupled waveguides. In addition, this coupling or power transfer between cores will obviously compromise the quality of images produced by endoscopic imaging systems. For example, the resolution estimated from the fiber core size and separation is reduced by the non-negligible crosstalk observed here, resulting in blurred images. With the use of a stable wavelength source for confocal imaging, core coupling will introduce a constant percentage error in pixel values. The adaptation of these image fibers to two-photon microscopy is compromised by the wavelength dependence of the coupling as pulse spectrum and power splitting will occur. Also, because fiber bundles are flexible, the polarization of the input light typically cannot be maintained, resulting in dynamic coupling behavior along the fiber and a changing output pattern that will affect the images produced by these image fibers.

In conclusion, the mechanism that allows current high resolution image fibers to function in an endoscopic system is variation in pixel size and shape. Situations of strong core coupling were shown to exist for image fibers typically used in endoscopes despite the presence of nonuniformity. The wavelength and polarization dependence of this coupling was demonstrated experimentally and correctly predicted by numerical modeling based on light propagation in coupled waveguides. With an improved understanding of these fibers and how core mismatch is necessary for independent core propagation, image fibers can be more effectively utilized in current research and applications and their design improved to meet the demand for smaller, denser pixel arrays.

The work presented in this chapter has been submitted for publication in the Optics Letters Journal and the CLEO/QELS 2007 conference proceedings.

Chapter 11

CONCLUSION

Although basic modeling using coupled mode theory and the normal mode expansion method can predict the dimensions for multi-core photonic crystal fibers that would result in minimal core coupling, it has been shown that nonuniformities in the fiber cross-section influence the properties of the actual fabricated fibers. In Chapter 7 it was revealed that nonuniformities will cause the actual coupling length to be shorter than the coupling length estimated from simulations. This conclusion would seem to indicate that a multi-core PCF with weakly coupled cores would be impossible to fabricate; however, the numerical results in Chapter 8 demonstrate that the coupling efficiency is more important than the coupling length when considering the strength of core interactions. The effects of imperfections in the fiber cross-section, as well as the dependence of this response on the size of the air holes, were explained through a comparison with coupled mode theory. Our results show that structural nonuniformities in two-core PCFs that could be a consequence of normal fabrication processes have the potential to drastically reduce the efficiency of coupling allowing coupling to be practically ignored. The coupling efficiency of two-core PCFs is shown to be minimal when the air holes are large even when only small nonuniformities are present. Imperfections in the cladding cause the two cores to become decoupled and, as a result, light propagates essentially independently in each core. These results relax the restrictions for obtaining weak coupling between cores in a multi-core PCF. While PCFs with large air holes are still the preferred structure, a slightly non-uniform photonic crystal cladding is also necessary.

In addition, for large air hole fibers, lattice irregularities are shown to induce significant birefringence such that the fabricated fiber can be almost guaranteed to have a rather large birefringence due to the unavoidable fact that the fiber cross-section will be slightly nonuniform. Large birefringence will allow the polarization to be maintained along the length of the fiber. Nonuniformities cause a negligible change in the confinement loss for low loss fibers and dispersion is shown to be robust if the percentage of variation in the fiber parameters is less than 2% and the structure does not fall within a cutoff region.

Basic analysis of multi-core step-index fibers with the dimensions of typical image fibers reveals that the cores should be strongly coupled. We have shown that coupling in actual image fibers is reduced through random variations in the fiber cross-section. Nonuniformity in core size and shape increases the likelihood of modal mismatch between adjacent cores, which results in weakened coupling. In addition, we experimentally demonstrated that despite this reduction in core-to-core interactions, strong coupling can be observed in fiber bundles typically used for endoscopic imaging. This coupling depends on the wavelength as well as on the polarization of the input light. These results indicate that the performance of currently available image fibers, and therefore the quality of images transmitted by endoscopes, is still compromised by crosstalk.

Future directions

The performance of current image fibers can be further quantified by experimentally examining the reliability of each pixel. A narrow band source could be scanned across one fiber endface while the output at the opposite end is imaged. The percentage of power coupled into adjacent cores could then be assessed in order to provide an overall estimate of the performance of the fiber. In addition, an endoscope system could be replicated by placing optics at the distal end of the fiber. A sample would be imaged while the wavelength of the illumination source is changed and the quality of these images compared. This type of experiment would provide a more tangible demonstration of the effects of changing the wavelength on the quality of the images transmitted through an endoscope. Additional experiments could also be performed in longer wavelength regimes.

Endoscopes for multiphoton microscopy require the delivery of high peak power pulsed lasers. Mismatch between adjacent cores should result in pulse spectrum and power splitting, yet the effect of propagation in an image fiber on the pulse shape and spectrum has yet to be thoroughly studied. Pulsed laser delivery with fiber bundles could be characterized by experimentally measuring the spectrum output by each core and by observing the overall change in the output spectrum and shape. Pulsed light propagation in image fibers can also be simulated through use of the numerical methods presented in this dissertation. Because a pulse is mathematically a sum of frequencies, each frequency can be propagated down the fiber according to the numerical methods explained in Chapter 3, then all frequencies can be recombined at the end of the fiber to observe the modulated pulse shape.

In proposing a design for a new fiber endoscope, there are three major areas where current fibers can be improved. A multi-core fiber with any of the following qualities would expand the potential of current endoscopes: higher core density, reduced crosstalk, or single-moded propagation. The feasibility of a single-moded fiber for endoscopes, especially, should be given additional attention. A multi-core PCF may be able to provide one of these improvements.

Appendix A

DISCUSSION OF A PROPOSAL FOR A PCF ENDOSCOPE

A proposal for a multi-core photonic crystal fiber for possible use in a flexible endoscope will be presented based on the numerical calculations presented in Chapter 6 on two-core PCFs. An example illustration of a multi-core PCF is shown in Figure A-1 and is similar in cross-section to a honeycomb lattice PCF [116]. A multi-core PCF is advantageous over a multi-core step-index fiber because a PCF has higher index contrast between the core and the cladding and can be fabricated from a single material. Higher index contrast will result in more well-confined modes, weaker coupling between the cores, and a higher potential information or core density. These characterisitics will improve the image quality of current endoscopes and also reduce their size if independent core propagation can be achieved. When light propagates independently in each core, phase information is retained from one end of the fiber to the other and laser scanning can be performed at the distal end of the fiber by controlling the wavefront at the proximal end. A diagram of this type of fiber endoscope is shown in Figure A-2.

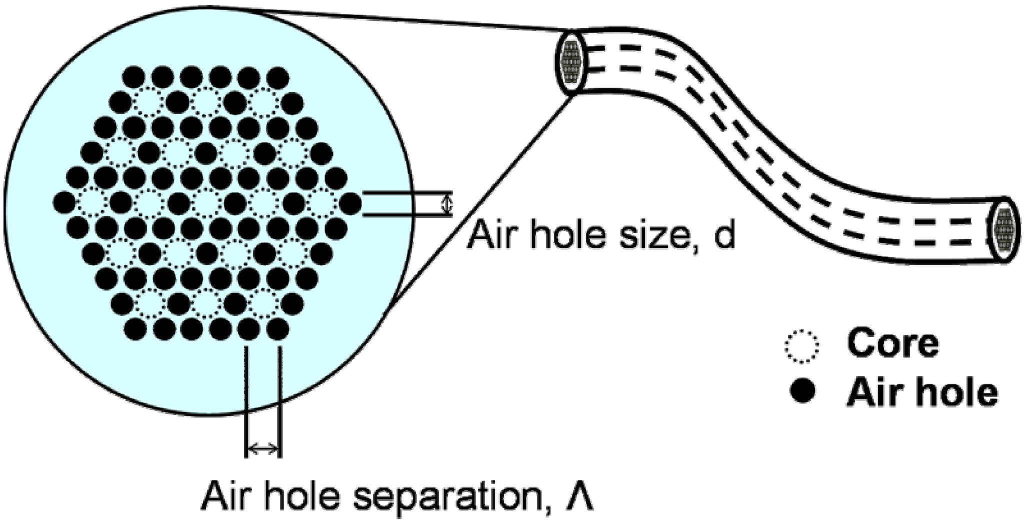

Figure A-1. Multi-core photonic crystal fiber for use in an endoscope.

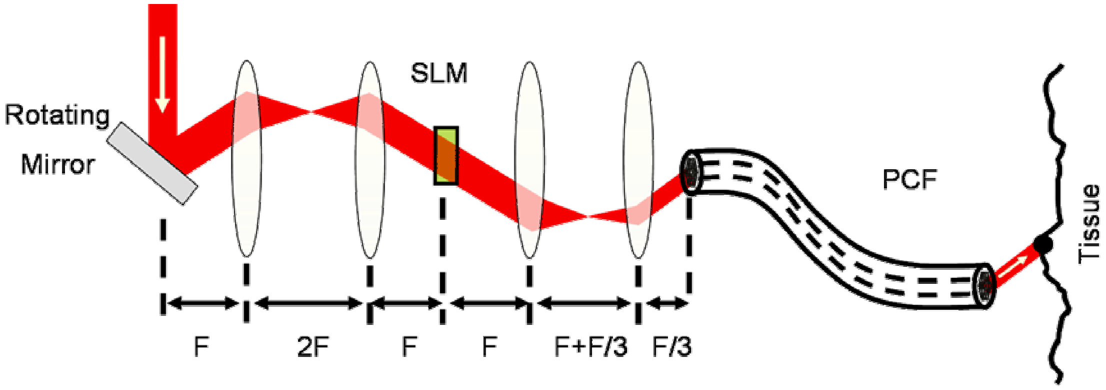

Figure A-2. Photonic crystal fiber endoscope.

The design of the multi-core PCF is guided by the need to reduce coupling between cores by increasing the coupling length. Based on the numerical modeling of two-core PCFs presented in Chapter 6, it is evident that a Type 2 fiber with large air holes and a large pitch will have a long coupling length. However, the modes of photonic crystal fibers also experience loss as they propagate due to their leaky nature; increasing the pitch will increase the imaginary part of the propagation constant resulting in increased loss. In addition, the multi-moded behavior of the cores becomes more apparent when the pitch is large. The plot in Figure A-3 illustrates the

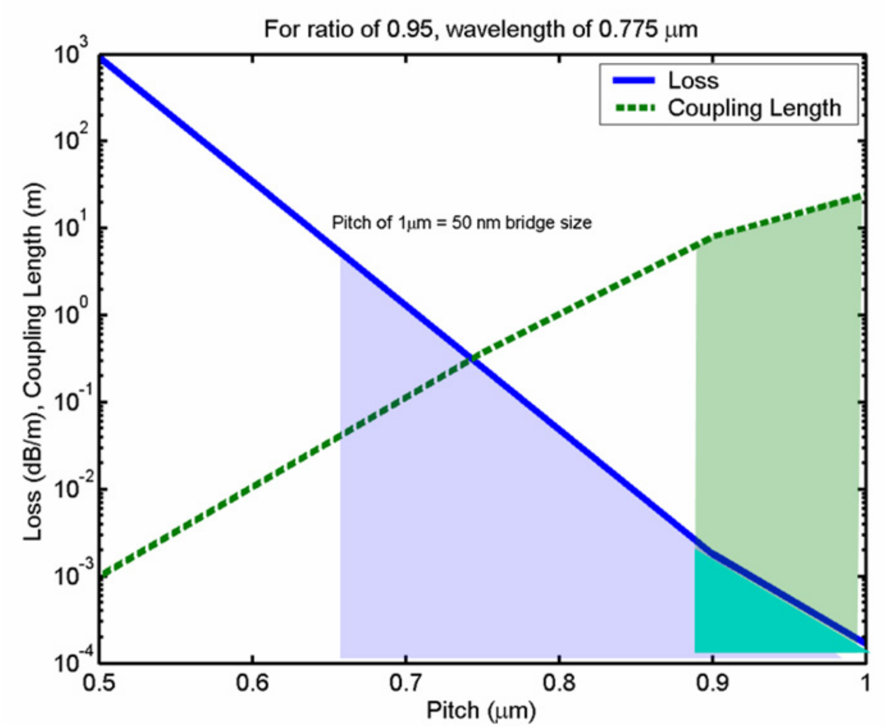

Figure A-3. The trade off between loss and coupling length is shown for a two-core PCF with d/Λ = 0.95 and a wavelength of 0.775 μm. The shaded regions indicate the acceptable limits for the two parameters.

trade-off between the loss and the coupling length for a fiber with large air holes, d/Λ = 0.95, λ = 775 nm, in an essentially single-moded regime. The shaded regions indicate the estimated limits for the loss, no larger than 10 dB/m, and for the coupling, a coupling length no shorter than 10 m. The PCF design is also limited by fabrication, in that the structures cannot be too small or they will collapse when drawn. By compromising the density of cores, the coupling length could be extended and the loss further reduced by adding another ring of air holes around the cores. Fiber designs that surround each core with two rings of air holes are included in Figure A-4. Thus, in addition to the coupling length, the mode loss, the number of modes, the core density, and the practicality of the design must be considered when designing a functional fiber.

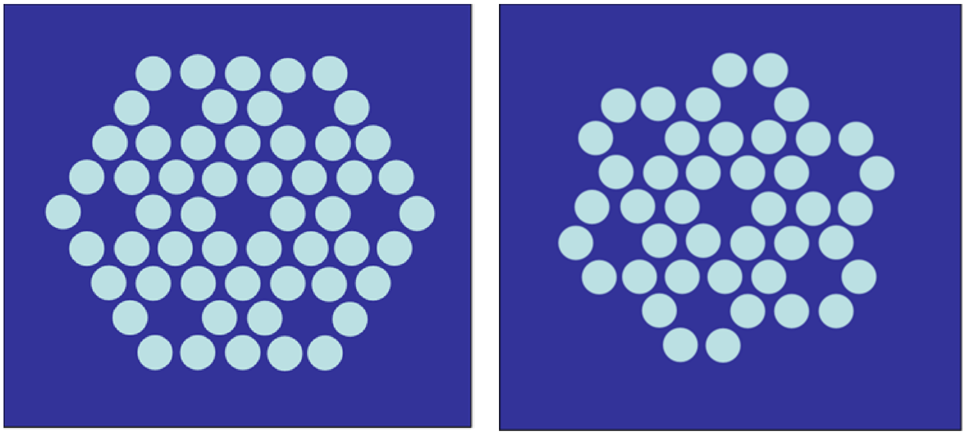

Figure A-4. The coupling between cores can be further weakened by adding a second ring of air holes around each core. Here are two examples of this type of multi-core PCF, each with a different packing fraction.

Two multi-core PCFs were obtained through collaborations with OFS Optics. Images of these fibers appear in Figure A-5. The two-core fiber in Figure A-5(a) has such a large core separation that no coupling was observed between the two cores and therefore the fiber had minimal value in our studies of inter-core coupling. Figure A-5(b) is an image of the preform for a requested design and Figure A-5(c) is the

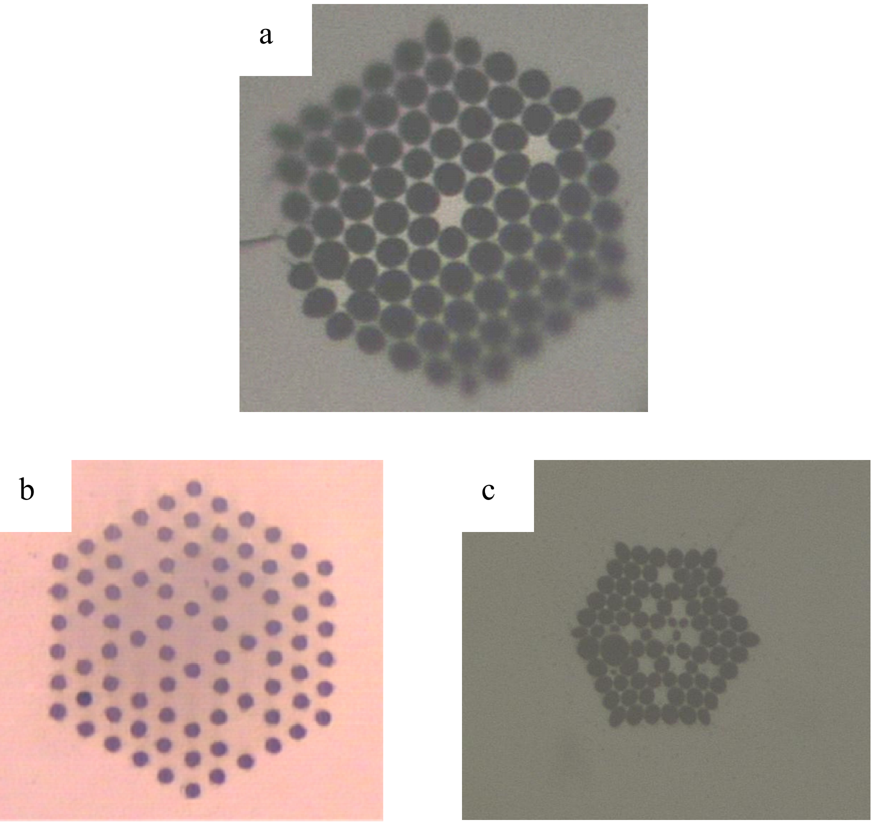

Figure A-5. Images of fibers obtained from OFS Optics. For the two-core PCF in a), the core diameters are approximately 2.4 µm and the core separation is 9.5 µm. In b) is an image of the preform for the fabricated fiber in c). This fiber was made using a new sol-gel process and the preform was etched before drawing. The fabricated fiber turned out extremely non-uniform, c).

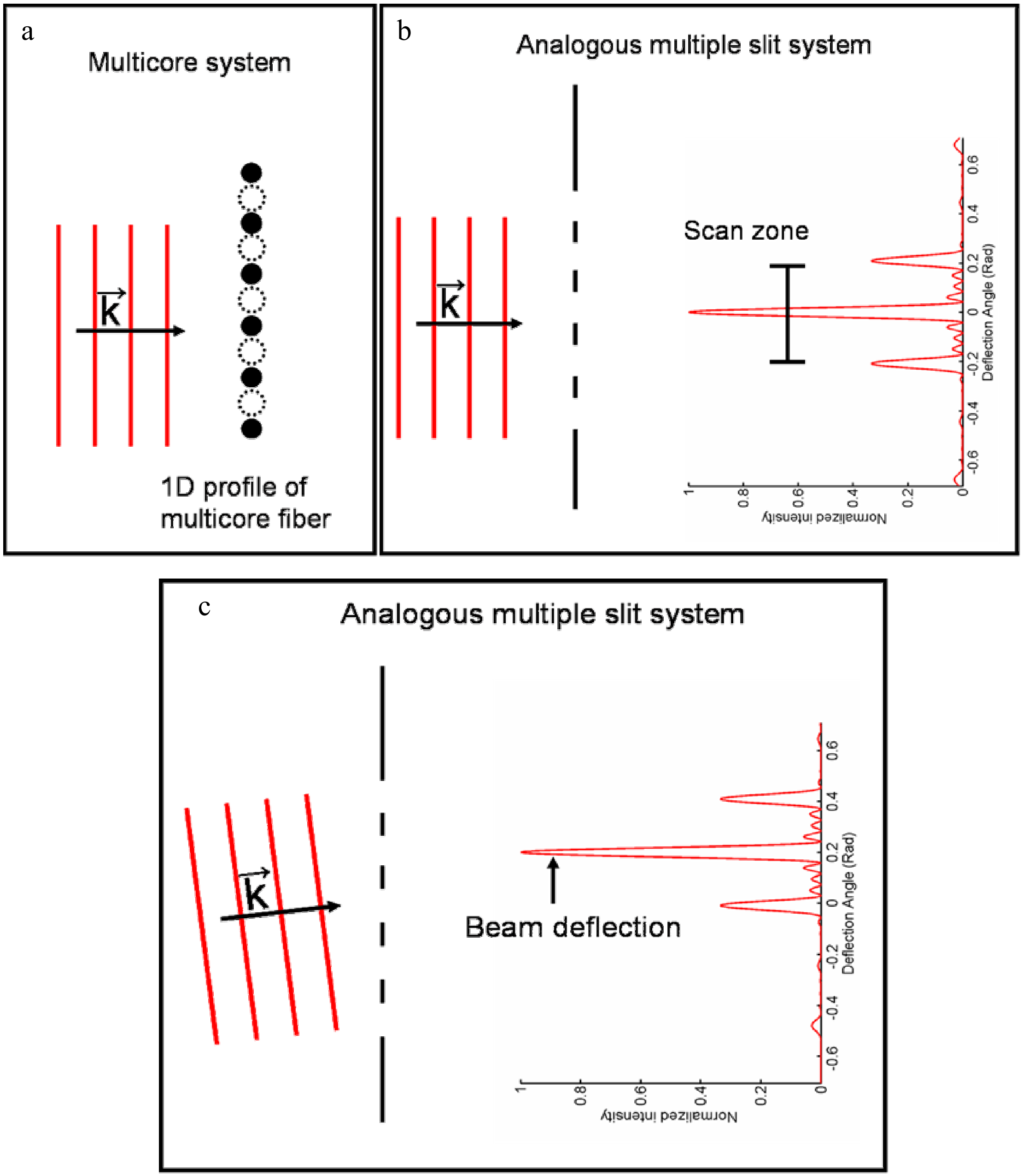

Figure A-6. The analogy between a multi-core PCF and a multiple slit systems is demonstrated (a-b). The scan zone indicated in b) is shifted in c) as a result of the angle of the incident beam.

fabricated fiber. The pitch of this PCF is approximately 2 μm and the core diameters are about 1.6 μm. Unfortunately, the fiber cross-section was extremely non-uniform in such a manner that coupling properties between the cores could not be accurately assessed. The coupling appeared to be strong between the cores in experimental testing, most likely due to the fact that the bridges between cores were not uniform and sometimes very large. Additionally, the cores were very small; therefore, strong coupling could also have been a result of the large effective area of the modes of these cores. OFS has agreed to continue to collaborate with our group and will provide additional multi-core PCFs for future research.

If independent core propagation can be guaranteed, remote laser scanning can then be performed at the distal end of the fiber. An appropriate wavefront is generated using lenses and scan mirrors at the proximal end of the multi-core PCF. The wavefront is coherently transported to the distal end of the fiber and then forms the desired intensity distribution at the tissue under test. The multi-core fiber can be compared to an optical phased array or analogously to a multiple slit system as shown in Figure A-6(a) and Figure A-6(b) in one dimension. The output of the fiber will resemble the far-field pattern of a diffraction grating or an N-slit interference pattern described by Eq. (A.1).

$$\begin{gathered} I(\theta) = \frac{I(0)}{N^2}\left(\frac{\sin\beta}{\beta}\right)^2\left(\frac{\sin N\alpha}{\sin\alpha}\right)^2 \\ \text{where: } \alpha = k\Lambda\sin\theta \text{ and } \beta = \alpha\left(1-\frac{1}{2}\frac{d}{\Lambda}\right) \end{gathered} \tag{A.1}$$

where the familiar α and β parameters, usually defined in terms of the slit size and separation, are defined here in terms of the pitch and the relative air hole size. This intensity pattern is plotted in Figure A-6(b). The zeroth order peak is used as the focused excitation spot at the sample plane; therefore, the distance between the first order peaks represents the scan zone. This zone can be shifted by changing the spatial frequency of the plane wave incident on the proximal end of the fiber, as shown in Figure A-6(c). In this manner, laser scanning can be performed at the distal end of the fiber using lenses and scan mirrors at the proximal end of the multi-core PCF.

The pitch, wavelength, air hole size, and the number of cores determine the quality of images that can be obtained from this type of scanning system. By decreasing the parameter $\lambda/(N\Lambda)$, the peaks of the interference pattern are sharpened and the spot size reduced. Thus, the resolution is improved at shorter wavelengths and for fibers with a larger number of cores and a larger core separation. The intensity of the central peak can be increased by decreasing the relative air hole size, d/Λ, which will improve the signal to background ratio. The scan zone can be extended by increasing the ratio of λ/Λ, thus enlarging the field of view of the endoscope. A trade-off exists between the obtainable resolution and the scan range due to the opposite influence of the wavelength on each of these qualities.

In conclusion, numerical modeling based on two-core PCFs provided the understanding necessary to submit a design to collaborators at OFS Optics. The fabricated fibers were, unfortunately, difficult to characterize and test. Future fibers will need to be tested for the ability to transport a wavefront coherently by experimentally examining the coupling between cores. In addition, the effects of external perturbations, such as temperature and bending, will need to be assessed as well as the efficiency of light collection from the distal end. Once the necessary characteristics of the fiber have been demonstrated, it will be implemented in a complete laser scanning imaging system. At that time, dynamic wavefront correction through use of a spatial light modulator will also be necessary.

Additional insight for designing a multi-core PCF endoscope was obtained in Chapter 7 and Chapter 8 through studying the effects of nonuniformities on the properties of PCFs. It was discovered in Chapter 7 that for large air hole fibers, the fabricated fiber can be almost guaranteed to have a rather large birefringence due to the unavoidable fact that the fiber cross-section will be slightly nonuniform. In Chapter 7 it was also revealed that nonuniformities will cause the actual coupling length to be shorter than the coupling length estimated from simulations; however, the numerical results in Chapter 8 demonstrate that the coupling efficiency is far more important when considering core interactions than the coupling length. Because nonuniformities in the photonic crystal cladding also reduce the coupling efficiency, essentially independent core propagation should be fairly common in fabricated multi-core fibers with large air holes.

These results relax the restrictions previously expressed in this Appendix in order to obtain weak coupling between cores in a multi-core PCF. While PCFs with large air holes are still the preferred structure, a slightly non-uniform photonic crystal cladding is also necessary. It should be noted that a trade-off does exist between nonuniformity and the number of propagating modes. Single-moded fibers tend to be more robust to variations and therefore exhibit stronger coupling; however, both single-moded propagation and uniformity are important for pulse propagation. Understanding the discrepancies between the properties of simulated and fabricated fibers is an important step in leveraging the unique properties of PCFs for use in endoscopes.

Appendix B

ADDITIONAL ANALYSIS OF COUPLING IN TWO-CORE PCFS WITH NONUNIFORMITIES

For some two-core PCFs, the introduction of irregularity in the air hole size and location resulted in complex effects on the modes and the power transfer between cores. Because such a large number of parameters are being varied (ie. the two-dimensional location and the size of each air hole in the PCF cladding), it is not surprising that some unpredictable characteristics developed.

Certain types of behavior were attributed to changes in the polarization of the modes. For example, the oscillation of power between the two cores occasionally exhibited additional beating behavior. The typical beating behavior described in Chapter 3 occurs between modes of the same polarization. However, when the cladding of a two-core PCF is varied in a random manner, the preferred axis for the modes is no longer necessarily the conventional x- and y-axes and beating occurs between modes of similar symmetry and of different polarizations. Figure B-1 shows a few examples of how the power in each core exhibited a beating behavior in addition to the typical power transfer. The frequency of the beats was often, though not

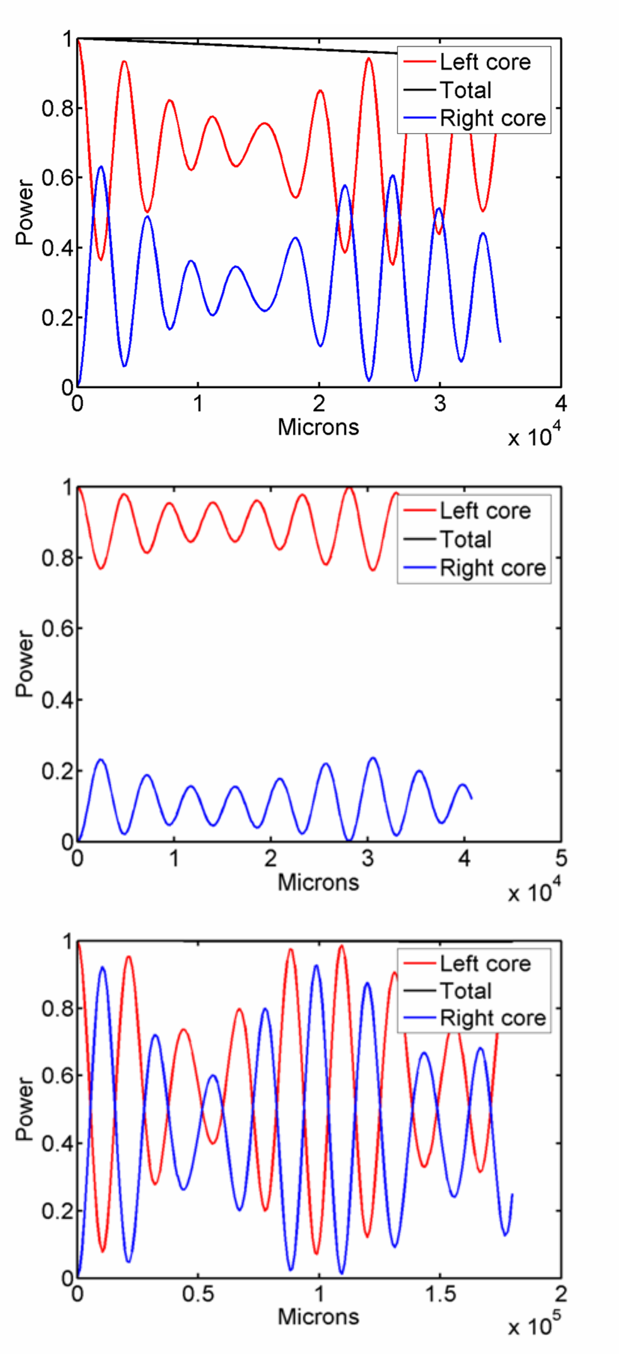

Figure B-1. Examples of the extra beat pattern appearing in the power oscillations of some two-core PCFs with nonuniformities.

conclusively, described by the beat frequency of the even or odd modes, thus demonstrating a mixing between the two polarizations.

A more intuitive understanding of this phenomenon can be gained by examining the modes of structures that exhibited beating and comparing them to structures that did not. In Figure B-2, four components of the modal field for one of the modes of two different two-core PCFs are shown. The images on the left are taken from a fiber that showed only the typical power transfer between the left and right cores while the images on the right are from a fiber that exhibited the beating in Figure B-1. It is evident by the orientation of the z-components of the field that the preferred axes are no longer the conventional x- and y- axes. The modes appear to be polarized along the x = y line rather than along x = 0 or y = 0. The change in polarization is also manifested by the fact that the electric field no longer distributes itself predominantly in the x- or y- component for a mode.

In addition, some structures developed coupling lengths much longer than the value for a perfect two-core PCF while for other structures it became difficult to define the coupling length because the beat patterns tended to be rather complex or bizarre. A few examples of these patterns are shown in Figure B-3. Sometimes, an extra long coupling length was the result of a large central air hole between the two cores. For other structures, the bizarre power oscillations appeared to be the result of a combination of beat patterns with similar frequencies. In general, PCFs with these characteristics were not able to be completely understood. When the coupling length taken from the power plots was longer than that of the perfect PCF, these structures were considered outliers and removed from the data analysis.

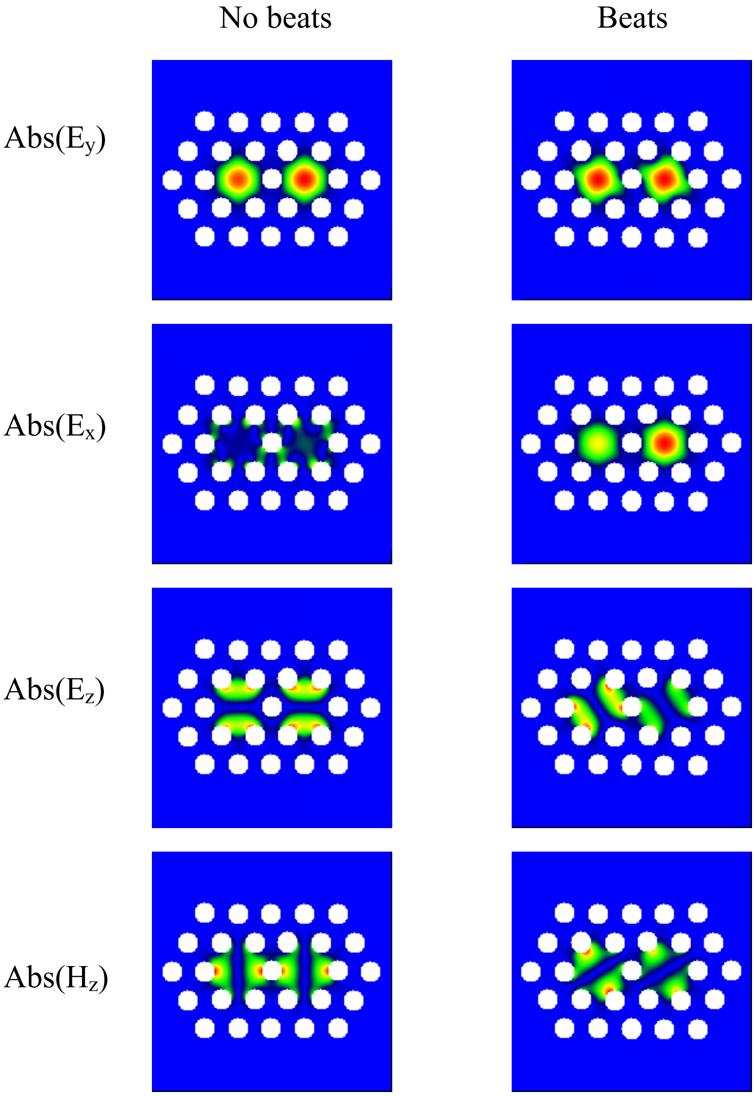

Figure B-2. Several components of the modal fields are shown for two different two-core PCFs with variations. The fiber on the left exhibited no extra beating in the power oscillations between the two cores while the power as a function of z for the fiber on the right appears in Figure B-1.

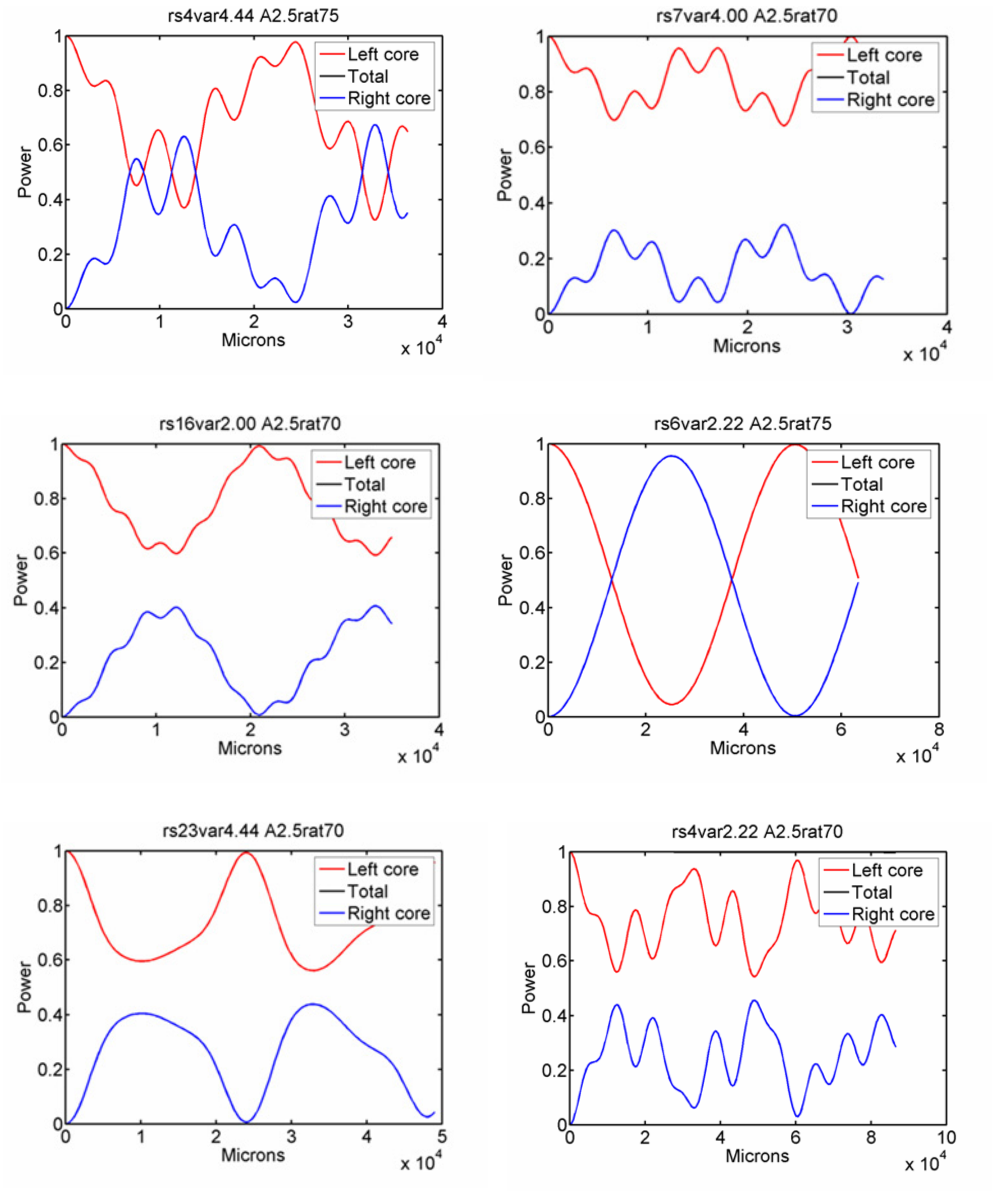

Figure B-3. Examples of the odd beating patterns in the power transfer that some two-core PCFs exhibited when nonuniformities were introduced into the cladding.

In order to further study trends in the degree of polarization of a mode, the ratio of the x-component of the field to the y-component was calculated over different degrees of variation. Specifically, the ratio in Eq. (B-1)

$$\frac{\iint \left| E_x^j \right|}{\iint \left| E_y^j \right|} \tag{B-1}$$

has a value greater than one for a preferentially x-polarized mode while a number less than one indicated a y-polarized mode. Although this ratio was not as large for the two-core PCFs studied as it generally is for two-core step-index fibers, the value nonetheless decreased as variation increased. However, because the orientation of the two modes does noticeably change with variations, this ratio is not necessarily a sign that the modes are becoming less linearly polarized, but instead, this trend suggests the modes become less loyal to the conventional x- and y-axes.

The even or oddness of the modes can be assessed in a similar manner by looking at the ratio of the field in one core to the field in the second core in Eq. (B-2).

$$\frac{\iint\limits_{leftcore} E_{x,y}^j}{\iint\limits_{rightcore} E_{x,y}^j} \tag{B-2}$$

If this value is positive, the mode is even, whereas if this value is negative the mode is odd. In general, the modes tended to retain the arrangement of the two highest index modes as the two modes with even symmetry. The left or rightness of a mode was also assessed using Eq. (B-3)

$$Leftness = \frac{\iint\limits_{leftcore} \left| S_z^j \right|}{\int \left| S_z^j \right|} \tag{B-3}$$

and can be used to determine the extinction ratio as presented in Chapter 8. The left or rightness of the modes of a two-core PCF increases with the degree of nonuniformity. Of course the modes of the perfectly uniform PCF have a left or rightness of 0.5, while in nonuniform PCFs, two modes are predominantly right and the other two modes are predominantly left.

When the input field used in the normal mode expansion to calculate the power as a function of the z-direction is changed from x-polarized to y-polarized, the resulting coupling lengths changed slightly. The average behavior and the relationship between the coupling length and the coupling efficiency as plotted in Chapter 8, however, remained the same. For two-core step-index fibers, changing the input polarization in the normal mode expansion resulted in the calculation of the y-polarized beat length from the plots of the power, which is slightly different from the beat length for the x-polarization.

Additional simulations are required in order to fully understand the impact of lattice nonuniformity on the polarization and the symmetry of the PCF modes. In general, simulations on two-core step-index fibers exhibited much less perturbation to the polarization of the modes even when variations where included. This result is not surprising considering the simulations performed on step-index fibers did not include variations in the core separation or orientation. The preferred axes, or the axes along which the cores were aligned, never changed; therefore, the modes remained x- and y-polarized as shown in Chapter 3.

REFERENCES

1. M. Minsky, "Memoir on inventing the confocal scanning microscope," Scanning **10**, 128-138 (1988).

2. W. Denk, J. Strickler, and W. Webb, "2-photon laser scanning fluorescence microscopy," Science **248**, 73-76 (1990).

3. "CUDOS MOF UTILITIES Software," (©Commonwealth of Australia, 2004) All rights reserved. www.physics.usyd.edu.au/cudos/software/.

4. C. Pollack, and M. Lipson, *Integrated Photonics* (Kluwer Academic Publishers, Boston, MA, 2003).

5. A. Snyder, and J. Love, *Optical Waveguide Theory* (Kluwer, London, 1983).

6. A. Yariv, *Optical Electronics in Modern Communications* (Oxford University Press, Inc., New York, 1997).

7. G. P. Agrawal, *Nonlinear Fiber Optics* (Academic Press, San Diego, CA, 2001).

8. W. P. Huang, C. L. Xu, S. T. Chu, and S. K. Chaudhuri, "A vector beam propagation method for guided-wave optics," Photonics Technology Letters, IEEE **3**, 910-913 (1991).

9. C. Vassallo, *Optical Waveguide Concepts* (Elsevier, Amsterdam, 1991).

10. A. Barybin, and V. Dmitriev, *Modern Electrodynamics and Coupled-Mode Theory: Application to Guided-Wave Optics* (Rinton Press, 2002).

11. S. L. Chuang, *Physics of Optoelectronics Devices* (Wiley-Interscience, 1995).

12. A. W. Snyder, "Coupled-Mode Theory for Optical Fibers," JOSA **62**, 1267 (1972).

13. S.-L. Chuang, "A coupled-mode theory for multiwaveguide systems satisfying the reciprocity theorem and power conservation," Lightwave Technology, Journal of **5**, 174-183 (1987).

14. A. W. Snyder, and A. Ankiewicz, "Optical fiber couplers-optimum solution for unequal cores," Lightwave Technology, Journal of **6**, 463-474 (1988).

15. H. A. Haus, W.-P. Huang, and A. W. Snyder, "Coupled-mode formulations," Optics Letters **14**, 1222 (1989).

16. W.-P. Huang, "Coupled-mode theory for couple optical wavedguides: an overview," JOSA A **11**, 963- (1994).

17. A. N. Kireev, and T. Graf, "Symmetric vector coupled-mode theory of dielectric waveguides," Optics Communications **244**, 25-35 (2005).

18. A. N. Kireev, and T. Graf, "Vector coupled-mode theory of dielectric waveguides," Quantum Electronics, IEEE Journal of **39**, 866-873 (2003).

19. J. C. Knight, T. A. Birks, P. S. J. Russell, and D. M. Atkin, "All-silica single-mode optical fiber with photonic crystal cladding," Opt Lett **21**, 1547 (1996).

20. T. A. Birks, P. J. Roberts, P. S. J. Russell, D. M. Atkin, and T. J. Shepherd, "Full 2-D photonic bandgaps in silica/air structures," Electronics Letters **31**, 1941-1943 (1995).

21. J. C. Knight, J. Broeng, T. A. Birks, and P. S. J. Russell, "Photonic Band Gap Guidance in Optical Fibers," Science **282**, 1476-1478 (1998).

22. S. John, "Strong Localization of Photons in Certain Disordered Dielectric Superlattices," Physical Review Letters **58**, 2486-2489 (1987).

23. E. Yablonovitch, "Inhibited Spontaneous Emission in Solid-State Physics and Electronics," Physical Review Letters **58**, 2059-2062 (1987).

24. J. D. Joannopoulos, R. D. Meade, and J. N. Winn, *Photonic Crystals: Molding the Flow of Light* (Princeton University Press, Singapore, 1995).

25. J. Joannopoulos, V. PR, and S. Fan, "Photonic crystals: Putting a new twist on light," Nature **386**, 143-149 (1997).

26. P. Russell, "Photonic Crystal Fibers," Science **299**, 358-362 (2003).

27. J. Broeng, D. Mogilevstev, S. E. Barkou, and A. Bjarklev, "Photonic Crystal Fibers: A New Class of Optical Waveguides," Optical Fiber Technology **5**, 305-330 (1999).

28. A. Bjarklev, J. Broeng, and A. S. Bjarklev, *Photonic Crystal Fibres* (Springer Science+Business Media, Inc., New York, 2003).

29. F. Zolla, G. Renversez, A. Nicolet, B. Kuhlmey, S. Guenneau, and D. Felbacq, *Foundations of Photonic Crystal Fibres* (Imperial College Press, London, 2005).

30. R. F. Cregan, B. J. Mangan, J. C. Knight, T. A. Birks, P. S. J. Russell, P. J. Roberts, and D. C. Allan, "Single-Mode Photonic Band Gap Guidance of Light in Air," Science **285**, 1537-1539 (1999).

31. J. Broeng, S. E. Barkou, T. Sndergaard, and A. Bjarklev, "Analysis of air-guiding photonic bandgap f ibers," Opt Lett **25**, 96-98 (2000).

32. J. Broeng, T. Sondergaard, S. E. Barkou Libori, P. M. Barbeito, and A. Bjarklev, "Waveguidance by the photonics bandgap effect in optical fibres," Journal of Optics A: Pure Applied Optics **1**, 477-482 (1999).

33. T. M. Monro, W. Belardi, K. Furusawa, J. C. Baggett, N. G. R. Broderick, and D. J. Richardson, "Sensing with microsctructured optical fibres," Measurement Science and Technology **12**, 854-858 (2001).

34. D. G. Ouzounov, F. R. Ahmad, D. Muller, N. Venkataraman, M. T. Gallagher, M. G. Thomas, J. Silcox, K. W. Koch, and A. L. Gaeta, "Generation of Megawatt Optical Solitons in Hollow-Core Photonic Band-Gap Fibers," Science **301**, 1702-1704 (2003).

35. D. G. Ouzounov, K. D. Moll, M. A. Foster, W. R. Zipfel, W. W. Webb, and A. L. Gaeta, "Delivery of nanojoule femtosecond pulses through large-core microstructured fibers," Opt Lett **27**, 1513-1515 (2002).

36. J. C. Knight, T. A. Birks, P. S. J. Russell, and J. P. d. Sandro, "Properties of photonic crystal fiber and the effective index model," Josa A **15**, 748-752 (1998).

37. T. A. Birks, D. Mogilevtsev, J. C. Knight, and P. St. J. Russell, "Dispersion compensation using single-material fibers," Photonics Technology Letters, IEEE **11**, 674-676 (1999).

38. J. K. W. Ranka, R.S.; Stentz, A.J., "Efficient visible continuum generation in air-silica microstructure optical fibers with anomalous dispersion at 800 nm," in *Lasers and Electro-Optics, 1999. CLEO '99. Summaries of Papers Presented at the Conference on* (1999), pp. CPD8/1-CPD8/2.

39. T. A. Birks, J. C. Knight, and P. S. J. Russell, "Endlessly single-mode photonic crystal fiber," Opt Lett **22**, 961-963 (1997).

40. M. Midrio, M. P. Singh, and C. G. Someda, "The space filling mode of holey fibers: An analytical vectorial solution," Journal of Lightwave Technology **18**, 1031-1037 (2000).

41. K. Saitoh, and M. Koshiba, "Empirical relations for simple design of photonic crystal fibers," Optics Express **13**, 267-274 (2005).

42. F. Brechet, J. Marcou, D. Pagnoux, and P. Roy, "Complete analysis of the characterstics of propagation into photonic crystal fibers, by the finite element method," Optical Fiber Technology **6**, 181-191 (2000).

43. M. Koshiba, and K. Saitoh, "Applicability of classical optical fiber theories to holey fibers," Opt Lett **29**, 1739-1741 (2004).

44. K. N. Park, and K. S. Lee, "Improved effective-index method for analysis of photonic crystal fibers," Opt Lett **30**, 958-960 (2005).

45. M. D. Nielsen, and N. A. Mortensen, "Photonic crystal fiber design based on the V-parameter," Optics Express **11**, 2762-2768 (2003).

46. M. D. Nielsen, N. A. Mortensen, J. R. Folkenberg, and A. Bjarklev, "Mode-field radius of photonic crystal fibers expressed by the V parameter," Opt Lett **28**, 2309-2311 (2003).

47. B. T. Kuhlmey, R. C. McPhedran, and C. M. d. Sterke, "Modal cutoff in microstructured optical fibers," Opt Lett **27**, 1684-1686 (2002).

48. N. A. Mortensen, "Effective area of photonic crystal fibers," Optics Express **10**, 341-348 (2002).

49. N. A. Mortensen, J. Folkenberg, M. D. Nielsen, and K. P. Hansen, "Modal cutoff and the V parameter in photonic crystal fibers," Opt Lett **28**, 1879-1881 (2003).

50. T. P. White, R. C. McPhedran, C. M. d. Sterke, L. C. Botten, and M. J. Steel, "Confinement losses in microstructured optical fibers," Optics Letters **26**, 1660-1662 (2001).

51. B. Kuhlmey, G. Renversez, and D. Maystre, "Chromatic Dispersion and Losses of Microstructured Optical Fibers," Applied Optics-OT **42**, 634-639 (2003).

52. V. Finazzi, T. M. Monro, and D. J. Richardson, "Small-core silica holey fibers: nonlinearity and confinement loss trade-offs," JOSA B **20**, 1427-1436 (2003).

53. M. Koshiba, and K. Saitoh, "Simple evaluation of confinement losses in holey fibers," Optics Communications **253**, 95-98 (2005).

54. A. L. Gaeta, "Nonlinear propagation and continuum generation in microstructured optical fibers," Opt Lett **27**, 924-926 (2002).

55. K. Saitoh, and M. Koshiba, "Numerical modeling of photonic crystal fibers," Lightwave Technology, Journal of **23**, 3580-3590 (2005).

56. F. Fogli, L. Saccomandi, P. Bassi, G. Bellanca, and S. Trillo, "Full vectorial BPM modeling of Index-Guiding Photonic Crystal Fibers and Couplers," Optics Express **10**, 54-59 (2002).

57. K. Saitoh, and M. Koshiba, "Full-vectorial imaginary-distance beam propagation method based on a finite element scheme: application to photonic crystal fibers," Quantum Electronics, IEEE Journal of **38**, 927-933 (2002).

58. M. Koshiba, and K. Saitoh, "Finite-Element Analysis of Birefringence and Dispersion Properties in Actual and Idealized Holey-Fiber Structures," Applied Optics **42**, 6267-6275 (2003).

59. T. P. White, B. T. Kuhlmey, R. C. McPhedran, D. Maystre, G. Renversez, C. M. d. Sterke, and L. C. Botten, "Multipole method for microstructured optical fibers. I. Formulation," JOSA B **19**, 2322-2330 (2002).

60. J. M. Fini, "Analysis of microstructure optical fibers by radial scattering decomposition," Optics Letters **28**, 992-994 (2003).

61. K. M. M. Lo, R.C.; Bassett, I.M.; Milton, G.W., "An electromagnetic theory of dielectric waveguides with multiple embedded cylinders," Lightwave Technology, Journal of **12**, 396-410 (1994).

62. S. Campbell, R. C. McPhedran, C. M. d. Sterke, and L. C. Botten, "Differential multipole method for microstructured optical fibers," JOSA B **21**, 1919-1928 (2004).

63. B. T. Kuhlmey, T. P. White, G. Renversez, D. Maystre, L. C. Botten, C. M. d. Sterke, and R. C. McPhedran, "Multipole method for microstructured optical fibers. II. Implementation and results," JOSA B **19**, 2331-2340 (2002).

64. M. J. Steel, T. P. White, C. M. d. Sterke, R. C. McPhedran, and L. C. Botten, "Symmetry and degeneracy in microstructured optical fibers," Optics Letters **26**, 488-490 (2001).

65. J. M. Fini, "Improved symmetry analysis of many-moded microstructure optical fibers," JOSA B **21**, 1431-1436 (2004).

66. P. McIsaac, "Symmetry-Induced Modal Characteristics of Uniform Waveguides --- I: Summary of Results," Microwave Theory and Techniques, IEEE Transactions on **23**, 421-429 (1975).

67. P. R. McIsaac, "Symmetry-Induced Modal Characteristics of Uniform Waveguides --- II: Theory," Microwave Theory and Techniques, IEEE Transactions on **23**, 429-433 (1975).

68. X. Yu, M. Liu, Y. Chung, M. Yan, and P. Shum, "Coupling coefficient of two-core microstructured optical fiber," Optics Communications **260**, 164-169 (2006).

69. K. Saitoh, Y. Sato, and M. Koshiba, "Coupling characteristics of dual-core photonic crystal fiber couplers," Optics Express **11**, 3188-3195 (2003).

70. J. M. Moison, A. M. Apetrei, J. A. Levenson, G. Melin, P. Pedeboseq, A. Fleureau, S. Lempereur, and L. Gasca, "Light transmission in multiple or single subwavelength trefoil channels of microstructured fibers," Optics Express **13**, 1193-1201 (2005).

71. T. M. Monro, P. J. Bennett, N. G. R. Broderick, and D. J. Richardson, "Holey f ibers with random cladding distributions," Opt Lett **25**, 206-208 (2000).

72. S. B. Libori, J. Broeng, E. Knudsen, A. Bjarklev, and H. R. Simonsen, "High-birefringent photonic crystal fiber," in *Optical Fiber Communication Conference and Exhibit, 2001. OFC 2001* (2001), pp. TuM2-1-TuM2-3 vol.2.

73. A. Cucinotta, S. Selleri, L. Vincetti, and M. Zoboli, "Perturbation analysis of dispersion properties in photonic crystal fibers through the finite element method," Lightwave Technology, Journal of **20**, 1433-1442 (2002).

74. J. M. Fini, "Perturbative numerical modeling of microstructure fibers," Optics Express **12**, 4535-4545 (2004).

75. I.-K. Hwang, Y.-J. Lee, and Y.-H. Lee, "Birefringence induced by irregular structure in photonic crystal fiber," Optics Express **11**, 2799-2806 (2003).

76. L. Zhang, and C. Yang, "Polarization splitter based on photonic crystal fibers," Optics Express **11**, 1015-1020 (2003).

77. B. T. Kuhlmey, R. C. McPhedran, C. M. d. Sterke, P. A. Robinson, G. Renversez, and D. Maystre, "Microstructured optical fibers: where's the edge?," Optics Express **10**, 1285-1290 (2002).

78. N. I. Nikolov, T. Srensen, O. Bang, and A. Bjarklev, "Improving efficiency of supercontinuum generation in photonic crystal fibers by direct degenerate four-wave mixing," Josa B **20**, 2329-2337 (2003).

79. W. E. P. Padden, M. A. v. Eijkelenborg, A. Argyros, and N. A. Issa, "Coupling in a twin-core microstructured polymer optical fiber," Appl Phys Lett **84**, 1689-1691 (2004).

80. K. L. Reichenbach, and C. Xu, "The effects of randomly occurring nonuniformities on propagation in photonic crystal fibers," Optics Express **13**, 2799-2807 (2005).

81. K. L. Reichenbach, and C. Xu, "Analysis of the effects of lattice irregularity in photonic crystal fibers," in *Conference on Lasers and Electro-Optics/Quantum Electronics and Laser Science and Photonic Applications Systems Technologies* (Optical Society of America, Baltimore, MD, 2005), p. CTuD1.

82. I. D. Chremmos, G. Kakarantzas, and N. K. Uzunoglu, "Modeling of a highly nonlinear chalcogenide dual-core photonic crystal fiber coupler," Optics Communications **251**, 339-345 (2005).

83. K. L. Reichenbach, and C. Xu, "Independent core propagation in two-core photonic crystal fibers resulting from structural nonuniformities," Optics Express **13**, 10336-10348 (2005).

84. K. L. Reichenbach, and C. Xu, "Independent core propagation in two-core photonic crystal fibers resulting from structural nonuniformities," in *Conference on*

Lasers and Electro-Optics/Quantum Electronics and Laser Science Conference and Photonic Applications Systems Technologies (Long Beach, CA, 2006), p. JTuD28.

85. A. F. Gmitro, and D. Aziz, "Confocal microscopy through a fiber-optic imaging bundle," Optics Letters **18**, 565 (1993).

86. A. F. Gmitro, A. R. Rouse, and A. Kano, "In vivo fluorescence confocal microendoscopy," in *Biomedical Imaging, 2002. Proceedings. 2002 IEEE International Symposium on* (2002), pp. 277-280.

87. Y. S. Sabharwal, A. R. Rouse, L. Donaldson, M. F. Hopkins, and A. F. Gmitro, "Slit-Scanning Confocal Microendoscope for High-Resolution In Vivo Imaging," Applied Optics **38**, 7133-7144 (1999).

88. J. Knittel, L. Schnieder, G. Buess, B. Messerschmidt, and T. Possner, "Endoscope-compatible confocal microscope using a gradient index-lens system," Optics Communications **188**, 267-273 (2001).

89. K.-B. Sung, C. Liang, M. Descour, T. Collier, M. Follen, and R. Richards-Kortum, "Fiber-optic confocal reflectance microscope with miniature objective for in vivo imaging of human tissues," Biomedical Engineering, IEEE Transactions on **49**, 1168-1172 (2002).

90. V. Dubaj, A. Mazzolini, A. Wood, and M. Harris, "Optic fibre bundle contact imaging probe employing a laser scanning confocal microscope," Journal of Microscopy **207**, 108-117 (2002).

91. W. Göbel, J. N. D. Kerr, A. Nimmerjahn, and F. Helmchen, "Miniaturized two-photon microscope based on a flexible coherent fiber bundle and a gradient-index lens objective," Optics Letters **29**, 2521-2523 (2004).

92. R. Juskaitis, T. Wilson, and T. F. Watson, "Real-Time White Light Reflection Confocal Microscopy Using a Fibre-Optic Bundle," Scanning **19**, 15-19 (1997).

93. G. L. Goualher, A. Perchant, M. Genet, C. Cavé, B. Viellerobe, F. Berier, B. Abrat, and N. Ayache, "Towards Optical Biopsies with an Integrated Fibered Confocal Fluorescence Microscope," Lecture Notes in Computer Science **3217**, 761-768 (2004).

94. E. Laemmel, G. M, L. G. G, P. A, L. G. J-F, and V. E, "Fibered Confocal Fluorescence Microscopy (Cell-viZio) Facilitates Extended Imaging in the Field of Microcirculation.," Journal of Vascular Research **41**, 400-411 (2004).

95. B. Flusberg, E. Cocker, W. Piyawattanametha, J. C. Jung, E. Cheung, and M. J. Schnitzer, "Fiber-optic Fluorenscence Imaging," Nature Methods **2**, 941 (2005).

96. K.-B. Sung, R. Richards-Kortum, M. Follen, A. Malpica, C. Liang, and Michael R. Descour, "Fiber optic confocal reflectance microscopy: a new real-time technique to view nuclear morphology in cervical squamous epithelium in vivo," Optics Express **11**, 3171-3181 (2003).

97. A. Rouse, A. Kano, J. Udovich, S. Kroto, and A. Gmitro, "Design and demonstration of a miniature catheter for a confocal microendoscope," Applied Optics **43**, 5763-5771 (2004).

98. A. Perchant, G. Le Goualher, M. Genet, B. Viellerobe, and K. Berier, "An integrated fibered confocal microscopy system for in vivo and in situ fluorescence imaging - applications to endoscopy in small animal imaging," in *Biomedical Imaging: Macro to Nano, 2004. IEEE International Symposium on*(2004), pp. 692-695 Vol. 691.

99. Y. Li, T. Wang, H. Kosaka, and S. K. Kasahara, "Fiber-image-guide-based bit-parallel optical interconnects," Applied Optics **35**, 6920-6933 (1996).

100. H. Kosaka, M. Kajita, Y. Li, and Y. Sugimoto, "A two-dimensional optical parallel transmission using a vertical-cavity surface-emitting laser array module and an image fiber," Photonics Technology Letters, IEEE **9**, 253-255 (1997).

101. R. K. Kostuk, and J. Carriere, "Interconnect Characteristics of Fiber Image Guides," Applied Optics **40**, 2428-2434 (2001).

102. C. Amatore, A. Chovin, P. Garrigue, L. Servant, N. Sojic, S. Szunerits, and L. Thouin, "Remote Fluorescence Imaging of Dynamic Concentration Profiles with Micrometer Resolution Using a Coherent Optical Fiber Bundle," Anal. Chem. **76**, 7202-7210 (2004).

103. T. Xie, D. Mukai, S. Guo, M. Brenner, and Z. Chen, "Fiber-optic-bundle-based optical coherence tomography," Optics Letters **30**, 1803-1805 (2005).

104. A. Komiyama, and M. Hashimoto, "A new class of crosstalk in image fibers," Optics Communications **107**, 49-53 (1994).

105. M. Nakamura, T. Otsubo, and K. Kitayama, "Skew characteristics of image fiber for high-speed 2-D parallel optical data link," Lightwave Technology, Journal of **18**, 1214-1219 (2000).

106. R. Conde, C. Depeursinge, B. Gisin, N. Gisin, and B. Groebli, "Refractive index profile and geometry measurements in multicore fibres," Pure Applied Optics **5**, 269-274 (1996).

107. K. Nishioka, K. Ono, and M. Shiraiwa, "Image Fiber," in *www.freepatentsonline.com* (Olympus Optical Co., Ltd., Tokyo, Japan, USA, 1995).

108. K. Ono, M. Shiraiwa, and K. Nishioka, "Image fiber and method of fabricating the same," in *www.freepatentsonline.com* (Olympus Optical Co., Ltd., Tokyo, Japan, USA, 2000).

109. S. Kumar, U. H. Manyam, and V. Srikant, "Optical fibers having cores with different propagation constants, and methods of manufacturing same," in *www.freepatentsonline.com* (Corning Incorporated, Corning, NY, USA, 2003).

110. E. Marcatili, "Improved coupled-mode equations for dielectric guides," Quantum Electronics, IEEE Journal of **22**, 988-993 (1986).

111. A. Komiyama, "Localization of mode waves in a disordered multi-waveguide system," Optics Communications **151**, 25-30 (1998).

112. A. Kumar, R. K. Varshney, and K. Thyagarajan, "Birefringence calculations in elliptical-core optical fibres," Electronics Letters **20**, 112-113 (1984).

113. R. Dyott, J. Cozens, and D. Morris, "Preservation of polarization in optical-fiber waveguides with elliptical cores," Electronics Letters **15**, 380-382 (1979).

114. K. Okamoto, T. Hosaka, and Y. Sasaki, "Linearly single polarization fibers with zero polarization mode dispersion," Quantum Electronics, IEEE Journal of **18**, 496-503 (1982).

115. K. L. Reichenbach, and C. Xu, "Coupling of Light in a Coherent Fiber Bundle," in *Biophysical Society 50th Annual Meeting* (Salt Lake City, UT, 2006), pp. 658-Pos/B524.

116. S. E. Barkou, J. Broeng, and A. Bjarklev, "Silica–air photonic crystal fiber design that permits waveguiding by a true photonic bandgap effect," Opt Lett **24**, 46 (1999).